INFORMATION TO USERS

The most advanced technology has been used to photograph and reproduce this manuscript from the microfilm master. UMI films the text directly from the original or copy submitted. Thus, some thesis and dissertation copies are in typewriter face, while others may be from any type of computer printer.

The quality of this reproduction is dependent upon the quality of the copy submitted. Broken or indistinct print, colored or poor quality illustrations and photographs, print bleedthrough, substandard margins, and improper alignment can adversely affect reproduction.

In the unlikely event that the author did not send UMI a complete manuscript and there are missing pages, these will be noted. Also, if unauthorized copyright material had to be removed, a note will indicate the deletion.

Oversize materials (e.g., maps, drawings, charts) are reproduced by sectioning the original, beginning at the upper left-hand corner and continuing from left to right in equal sections with small overlaps. Each original is also photographed in one exposure and is included in reduced form at the back of the book.

Photographs included in the original manuscript have been reproduced xerographically in this copy. Higher quality 6" x 9" black and white photographic prints are available for any photographs or illustrations appearing in this copy for an additional charge. Contact UMI directly to order.

U·M·I

University Microfilms International
A Bell & Howell Information Company
300 North Zeeb Road, Ann Arbor, MI 48106-1346 USA
313 761-4700 800 521-0600

Order Number 9017188

The quasi-parallel collisionless shock wave: A simulation study

Mandt, Mark Edward, Ph.D.
University of Alaska Fairbanks, 1988

U·M·I
300 N. Zeeb Rd.
Ann Arbor, MI 48106

THE QUASI-PARALLEL COLLISIONLESS SHOCK WAVE: A SIMULATION STUDY

A

THESIS

Presented to the Faculty of the University of Alaska

in Partial Fulfillment of the Requirements

for the Degree of

DOCTOR OF PHILOSOPHY

By

Mark E. Mandt, B.S., M.S.

Fairbanks, Alaska

September 1988

THE QUASI-PARALLEL COLLISIONLESS SHOCK WAVE:

A SIMULATION STUDY

by

Mark E. Mandt

RECOMMENDED:

D. Das

L. C. Lee

J. V. Olson

D. W. Swift

J. R. Kan, Chairman, Advisory Committee

J. L. Morack, Head, Physics Department

APPROVED:

K. Jayaweera, Dean, College of Natural Sciences

L. Proenza, Dean of the Graduate School

7/18/88

Date

Abstract

The structure of the quasi-parallel collisionless shock wave is studied via a numerical simulation model. The model is compared to observations and theoretical predictions and within its limitations appears to reproduce the true shock structure reasonably well. Three electron equations of state and their effects on the simulation are examined. It is found that only the isotropic-adiabatic electron equation of state yields acceptable results in the simulation at high Mach numbers. The scale lengths of the shock are measured, normalized by the natural scale lengths of the plasma, and plotted as a function of the Alfvén Mach number. It is found that the wavelength of the upstream waves follows that predicted for a phase standing whistler quite well and the scalelength of the jump in the magnitude of the magnetic field is generally greater than, but approximately equal to this wavelength. For Alfvén Mach numbers $M_A \gtrsim 2.5$, waves are generated in the downstream region. Their wavelength and the scale length of the plasma transition are larger than the natural scale lengths of the plasma. The ion heating is seen to occur in two stages. In the first stage which occurs upstream of the principal shock ramp, the heating can be characterized by a polytropic power law equation of state with an exponent much greater than the isentropic-adiabatic rate of $\gamma = 5/3$. The second stage of heating which occurs from the principal shock ramp to the downstream region is characterized by an exponent on the order of the isentropic-adiabatic rate. The results show that the ion heating occurs mainly around the principle density jump near the center of the shock transition region, while the increase in entropy takes place mainly in the upstream side of the shock transition region. It is suggested that the ion heating is a consequence of the non-adiabatic scattering of the ions through the magnetic field of the shock and its upstream precursor wave.

Table of Contents

List of Figures

List of Tables

Acknowledgments

This thesis is the culmination of four years of research and study. It is an extension of the work that I began six years ago when I first joined the Space Physics and Atmospheric Sciences program here at the Geophysical Institute. It would be nearly impossible to give proper credit to all those who in some fashion helped me to produce this thesis. However, I would like to attempt to mention those who had the most impact on this work and my stay in Alaska in general.

First I would like to acknowledge my advisory committee. While I have a strong tendency to work on my own and in my own way, they provided me with invaluable knowledge on subjects ranging from basic physics to specific analysis techniques. My only regret is that I did not take greater advantage of their considerable experience and expertise. Joe Kan, my principal advisor, provided the impetus for this work and along with Dan Swift laid the groundwork upon which it would be built. Though many battles were fought over concepts, the methodology, and even the material in the thesis, the result is a much better piece of work than I could have accomplished by myself. Joe gave me plenty of freedom to pursue my own ideas while still peeking over my shoulder from time to time to ensure that I was not too far out in left field. He also provided me with support for the duration, paid my not inconsiderable computer bills, and gave me considerable exposure to the scientific community by sending me to seven conferences during this time (of course I had to make presentations at six of them). At these meetings I have had the opportunity to have some interesting discussions with Dr.'s K. B. Quest, C. F. Kennel, J. Chao, C. S. Wu (who is soon to be my new employer), and others.

The rest of the committee has also given me much help along the way. Dan Swift is the originator of the simulation code upon which most of this thesis is based. He has also taught me much of the basic physics and general simulation techniques that I have learned here. I have had many very stimulating conversations with Lou Lee on the physics of

shocks. It can be a lot of fun to kick around ideas with a mind as sharp as his. John Olson has been of great assistance in helping me understand and interpret the material dealing with satellite observations. He has also ensured that the remainder of the thesis turned out to be fairly understandable to someone who has not studied shock waves. I would also like to thank Tom Roberts for sitting in as the outside committee member and Deben Das who replaced Tom when he retired. And of course, many of the other faculty members here at the Institute have discussed ideas with me and offered their own comments as well as teaching me about some of the other fields of study here.

Many of the staff members also deserve credit for the help they have given me. Dick Million, Celia Rohwer, and Rick Guritz have taught me much about VMS and the VAX computer system. They also put up with my plentiful, but often naive, questions about the system. The ladies of the director's office and the business office were always cheerfully prompt in helping to deal with the unavoidable paperwork. They also shared with me my joys (primarily K. C.) and sympathized with my sorrows.

My fellow students and friends were an important part of my life here. A few of them are (listed alphabetically as they are all equally my very good friends) Bob Sica, Dirk Lummerzheim, Gerald Walker, Jim Conner, Nettie La Belle-Hamer, and Rodney Viereck as well as their families. Without them to enjoy the good times with me and give me moral support for the hard times my stay here would have been an experience to be endured rather than to be gratefully remembered. We have also managed to work out a fair amount of physics and analysis techniques at our tea time discussions. My many chinese friends have provided for me an invaluable intercultural experience.

My parents are of course responsible for my existence. They have always told me that I could do whatever I wanted to do with my life and then encouraged me on with the decisions that I made. And lastly, but most important (to me) is Jill my wife and K. C. my son. Their faith in me and simply their being there has been an inspiration to

my existence. Finally I would like to finish with a quotation which I used in my Master's thesis but seems to be even more appropriate for this one.

> Two roads diverged in the forest and I-
> I took the one less traveled by,
> And that has made all the difference.
>
> Robert Frost

P.S. I would also like to acknowledge support for this work from the director's office for computer resources, NSF grant ATM-85-21194 and NASA grant NAGW-906 for other financial support. The computation work was done on the Geophysical Institute's VAX 11/780 and 11/785, the Space Physics group's VAX 11/730 and MicroVax II, and the University of Alaska VAX 8800. This manuscript was typeset with TEX.

Chapter 1. Introduction

The study of collisionless shock waves has been underway for over 25 years. These shock waves have provided a variety of nonlinear phenomena for study within the discipline of space plasma physics. They are an integral part of planetary magnetospheres, comets, solar flares, high speed streamers, and coronal mass ejections. They produce a variety of interactions within the medium through which they propagate and at the obstacles which they encounter. This introduction begins with some background information about the nature and discovery of collisionless shock waves. Some of the properties of perpendicular and quasi-perpendicular shocks will be presented and contrasted with the quasi-parallel shock, which is the topic of this study. Finally, a description of the content of the remainder of this thesis will be given.

1.1 Background

Of the three principal Magnetohydrodynamic (MHD) wave modes, the fast (or magnetosonic, or whistler), intermediate (or Alfvén), and slow modes (see Chapter 2.2 for a discussion of the MHD wave modes), both the fast and slow modes can be shown to undergo nonlinear steepening (Kantrowitz and Petschek, 1966). This nonlinear steepening can lead to shock formation as will be discussed in the next chapter on shock wave fundamentals. Fast mode shocks are the most commonly observed type of MHD shock. This is because the solar wind flow is faster than the fast mode speed so the planetary bow shocks must be fast mode shocks. The slow mode shock is thought to play an important role in the reconnection process (Petschek, 1964). The existence of the slow mode shock has not been clearly established either observationally or theoretically. The slow mode shock will

not be further discussed here, however the interested reader may refer to Swift (1983b), Feldman *et al.* (1984a,b), Hada and Kennel (1985), Winske *et al.* (1985), Edmiston and Kennel (1986), and Wolfson (1987) for recent studies.

The existence of collisionless shock waves had been hypothesized some time before their actual discovery. It had been speculated that a standing bow wave should exist ahead of the magnetopause (Zhigulev, 1959; Axford, 1962; Kellog, 1962) and that shock waves should appear in the interplanetary medium (Parker, 1961). The study of collisionless plasma shocks had its major impetus with the first satellite observations in the early 1960's when the Earth's bow shock was discovered (Freeman, 1964; Ness *et al.*, 1964). Since laboratory experiments could not produce a collision-free plasma of sufficient dimensions in which to generate a shock wave these satellite observations motivated the study of collisionless shocks in a magnetized plasma. The only work done on them prior to this time consisted of theoretical conjecture, no experimental proof existed.

Sonnett and Abrams (1963) observed what they believed to be shock like features in magnetic field measurements from Explorer 1. Freeman (1964) reported heating of the electron distribution at the bow shock as observed by Explorer 12. Ness *et al.* (1964) identified the bow shock as a collisionless magnetohydrodynamic shock from IMP-1 magnetic field measurements. As observations continued there was much work done on classification of the large variety of shock structures. The International Sun Earth Explorer (ISEE) satellite program which began in 1978 has yielded high resolution, multi-spacecraft data about both the Earth's bow shock and interplanetary shocks. Other spacecraft missions have also probed interplanetary shocks as well as the bow shocks of the other planets.

1.2 Classification of Shock Structures

The various collisionless shock waves can be classified by three principal parameters. They are: the Alfvén Mach number (M_A), the ratio of kinetic to magnetic pressures (β, also known as the plasma beta), and the angle between the magnetic field and the shock normal (θ_{Bn}). These parameters determine the gross, macroscopic characteristics of a shock. Other parameters, such as the ion to electron pressure ratio, pressure anisotropies, relative abundance of ion species, etc., may also be of importance in determining the microstructure and dissipation processes of a shock.

The solar wind plasma which constitutes the interplanetary medium is principally an electron-proton plasma with usually less than 5% helium nuclei and trace amounts of heavier elements. The electron and ion populations can have a multi-component character (i.e. counterstreaming beams). The Alfvén Mach number and plasma beta in the Solar Wind can vary over a wide range, $0.01 < \beta < 100$ and $1.2 < M_A < 20$ (Formisano, 1977). Typical values are $0.1 < \beta < 5$ and $2 < M_A < 10$. Low β, low M_A shocks tend to be laminar. As either β or M_A increases, the structure tends to be more turbulent. However, these changes are not entirely independent of θ_{Bn}.

The shock normal angle θ_{Bn} can vary from 0° to 90°. It does not range beyond 90° because the shock structure is symmetric with respect to reversal of the magnetic field direction. Depending on θ_{Bn}, shock waves have been divided into two categories with very different characteristics. These categories are usually referred to as quasi-parallel shocks ($\theta_{Bn} \lesssim 45°$) and quasi-perpendicular shocks ($\theta_{Bn} \gtrsim 45°$). The quasi-perpendicular shock exhibits a very clean, well defined structure on the ion inertial and/or gyro-radius scales. The physical mechanisms involved are fairly well understood (Kennel *et al.*, 1985; Scudder *et al.*, 1986a,b,c) and will be described briefly.

The structure of the quasi-perpendicular shock changes depending on whether the shock is sub-critical or super-critical. This critical Mach number is the one at which resistivity can no longer provide the required dissipation needed to satisfy the Rankine-Hugoniot conditions (Kantrowitz and Petschek, 1966). Sub-critical shocks can be further divided into dispersive, resistive, or perhaps a combination of the two. For nearly perpendicular shocks the field gradients are steep and large currents excite electrostatic instabilities to provide an anomalous resistivity on a distance scale of the electron inertial length (c/ω_{pe}). At more oblique angles, plasma dispersion produces a shock structure characteristic of a large amplitude damped whistler wave (Greenstadt and Fredericks, 1979; Greenstadt *et al.*, 1984).

Above the critical Mach number ion reflection begins to produce additional features in the shock structure. These reflected ions produce a "foot" in the magnetic field that extends about twice the ion streaming gyro-radius ($\rho_s = V_s/\Omega_i$ where V_s is the streaming velocity and Ω_i is the ion gyro-frequency) ahead of the main ramp. Once transmitted they produce an oscillating structure in the density and magnetic field that scales with the downstream gyro-radius. The thickness of the main ramp, as based upon the magnetic field, density, and velocity profiles, is proportional to the ion inertial length (c/ω_{pi}).

On the other hand, the quasi-parallel shock has a very broad structure that extends well beyond the scale lengths of the quasi-perpendicular shock. Changes in the flow properties of the quasi-parallel shock usually occur over length scales an order of magnitude greater than the above mentioned ion scales. This is accompanied by an upstream wave train and perhaps turbulence upstream and downstream that can extend to distances of two or three orders of magnitude greater than the ion scale lengths. Part of the reason for this characteristic of quasi-parallel shocks is that the geometry allows greater access of the shocked particles to the upstream region. In the limit of the perpendicular shock a particle can only reach to the streaming gyro-diameter upstream of the shock. Back-streaming

particles from the quasi-parallel shock can generate waves which add to the chaos of the shock structure. The complicated structure of the quasi-parallel shock has made it difficult to determine the physical processes which underlie it. Recent reviews of the quasi-parallel collisionless shock may be found in Greenstadt (1985), Kennel (1985), and Quest (1985).

1.3 This Work

This work is a study of some of the unsolved problems of the quasi-parallel collisionless shock wave. The main tool used for this study is a numerical simulation model. In brief, the simulation model is a one and two halves dimensional, Darwinian hybrid code which uses a particle in cell algorithm. That is, it includes one spatial and all three velocity components. The displacement current is neglected in Maxwell's equations. The ions are treated as discrete particles while the electrons are treated as a massless fluid of finite pressure. Thus, the model assumes a planar geometry, high frequency radiation ($\omega \gtrsim \omega_{pe}$ where ω_{pe} is the electron plasma frequency) is neglected, and the ion dynamics are retained while the electrons are assumed to be inertialess ($m_e = 0$). A more complete description of the algorithm is given in Appendix A.

First, the fundamental concepts concerning shock waves are introduced in Chapter 2. This chapter begins with definitions pertaining to shock waves and the conservation (or Rankine-Hugoniot) equations for hydrodynamic discontinuities. Then nonlinear steepening of ordinary sound waves and the effects of dispersion and dissipation are discussed. The second section of Chapter 2 introduces the three basic MHD wave modes and discusses the modifications of the shock wave in a magnetized conducting fluid. Some of the characteristics of the MHD modes and their corresponding shocks are also described.

In Chapter 3 some shock observations made by satellites are incorporated into the simulation study. In the first section, an attempt is made to model three specific cases

of satellite observations and compare the simulation results with those observations. In the second section some of the difficulties in interpreting the observations are discussed. In particular, the Doppler shift and how it relates to differences between the observed and simulated results is addressed. A systematic discrepancy in the wavelength of the upstream precursor waves measured by the satellites, predicted by linear cold plasma dispersion theory, and seen in the simulation is noted. It is shown that this discrepancy may be explained by a simple geometric effect in the assumptions of the observed shocks, the theoretical prediction, and the simulation model.

Chapter 4 discusses the effects of three different electron equations of state and the resulting electrostatic fields within the simulation. Solutions of the Rankine-Hugoniot equations are used to calculate the expected potential jump as a function of Mach number and shock normal angle θ_{Bn}. The effects of using these equations of state in the simulation model are also discussed.

Chapter 5 contains the results of a study of the scalelengths of the quasi-parallel collisionless shock wave as a function of the Alfvén Mach number. To be examined are the wavelengths of the upstream and downstream waves, the width of the magnetic field jump, the width of the density jump, and the width of the jump in the normal velocity component. These scale lengths are examined for a number of $\theta_{Bn} = 10°, \beta = 0.5$ shocks. They are also compared to the fundamental scale lengths of the plasma, the ion inertial length and the various gyro-radii.

In Chapter 6 the characteristics of the ion heating as seen in the simulation are presented. First, existing ion heating theories are summarized. Then a general description of the shock features is given followed by a more detailed examination of three representative cases. It will be demonstrated that most of the ion heating can be accounted for by discrete larmor radius effects as the incoming ions encounter the upstream precursor wave fields and the jump in the magnetic field magnitude. It is seen that microinstabilities are

not required for dissipation at the shock. However, the conditions of the shock tend to be unstable to streaming instabilities which may account for other wave structures associated with the shock.

Chapter 7 summarizes the principal results of this thesis. Appendix A contains a description of the algorithm upon which the simulation is based. Appendix B has a discussion of entropy relevant to the material of Chapters 4 and 5. In Appendix C a discussion of the interaction of particles with various magnetic field configurations is considered. The magnetic field configurations range from an exact discontinuity to idealized models of the true shock wave structure (as seen in the simulation).

Chapter 2. Fundamentals of Shock Waves

In this chapter I shall present a development of the basic concepts relating to shock waves. The first section will discuss shock waves from the perspective of simple hydrodynamics. The second section will introduce the variations of the simple gasdynamic shock due to the presence of a magnetic field within a conducting medium.

2.1 Gasdynamic Shocks

A hydrodynamic (gasdynamic) discontinuity, of which shocks are a special case, is a surface in a flow field across which various properties of the fluid change discontinuously (from a macroscopic viewpoint). Shocks are characterized by flow through the surface which is accompanied by changes in the fluid velocity, density, temperature, pressure, and entropy. The velocity decreases across the shock in the direction of the flow while the other quantities such as density, pressure, and entropy increase. Of course, the surface is not a true discontinuity. However, for the shocks to be considered in this chapter, the thickness of the surface is small compared to some appropriate macroscopic dimensions of the system in which it occurs. So the shock can be considered a true discontinuity for the purpose of obtaining the physical relationships between quantities on both sides of the shock.

Shocks are physical phenomena which must obey the conservation laws of mass, momentum and energy. These laws and an equation of state provide the relationships between fluid properties on both sides of the shock. The equations form a fourth degree polynomial with four possibly distinct roots. However, there are other constraints that must be satisfied for a physical shock to exist. The entropy must increase across the shock. Also, the fluid velocity in front of the shock is 'supersonic,' while behind it is 'subsonic.' Here

'supersonic' and 'subsonic' refer to faster and slower than the propagation speed of the appropriate wave mode in the medium.

The conservation equations as applied to a steady state discontinuity, often referred to as the Rankine-Hugoniot equations, are given in many standard texts (*e. g.* Boyd and Sanderson, p. 117, 1969): conservation of mass (or the continuity equation);

$$[\rho\vec{v}\cdot\hat{n}] = 0 \tag{2.1}$$

conservation of momentum (or the momentum equation);

$$[\rho\vec{v}(\vec{v}\cdot\hat{n}) + \hat{n}P] = 0 \tag{2.2}$$

and conservation of energy (or the energy equation);

$$\left[\vec{v}\cdot\hat{n}\left(\frac{1}{2}\rho v^2 + \frac{\gamma}{\gamma-1}P\right)\right] = 0 \tag{2.3}.$$

In the above equations ρ is the density, $\vec{v}$ is the fluid velocity, P is the pressure, γ is the ratio of specific heats, and $\hat{n}$ is the unit vector in the shock normal direction. The square brackets [ ] represent the change in the enclosed quantity between the upstream and downstream states. Solving this system of equations relates the downstream quantities to those upstream. These relationships are independent of the dissipation processes occurring within the shock transition layer.

The steepening of an ordinary sound wave to form a shock may be seen by examining a pressure pulse and the equation for the sound speed. The sound speed in a gas is given by

$$C_s = \sqrt{\frac{\gamma P}{\rho}} \tag{2.4}.$$

As long as discontinuities do not yet exist the compression is adiabatic (Landau and Lifshitz, p. 366, 1958). So we may write the sound speed using the adiabatic power law ($P/\rho^{\gamma} = const.$) for an equation of state as

$$C_s \propto \rho^{\gamma-1/2} \tag{2.5}$$

One can see from this that the local sound speed at any point on the pulse varies with the density. If we resolve the pulse as a succession of small steps then each step propagates at the local sound speed. Thus as the pulse evolves, the compressional part of the pulse (leading edge) will tend to steepen and the rarefactional part (trailing edge) will spread because the sound speed is higher in the higher density region. This nonlinear steepening is demonstrated in Figure 2.1 which shows the evolution of a right traveling pulse in a frame moving at the sound speed of the background gas.

At an early time in the nonlinear steepening process, when gradients in the moments of the gas (such as the density and velocity) are small, there is nothing to inhibit the steepening. When the gradients become large enough, some form of dissipation or dispersion begins to occur. Eventually a balance is reached between the nonlinear steepening process and the dissipation and/or dispersion. A dissipation process is usually considered to be any process whereby organized energy (such as bulk flow energy) is transformed into thermal energy with a resulting increase in entropy. Dispersion can reduce flow energy in two ways. It can propagate energy away from a discontinuity as wave energy. Dispersion can also determine the scale size and other properties of the discontinuity which will refract the flow as the flow passes through the discontinuity.

Consider a general dispersion relation expanded in the wave number k (long wavelength limit)

$$\omega = v_{ph}k + \mu k^2 + \alpha k^3 + \cdots \tag{2.6}$$

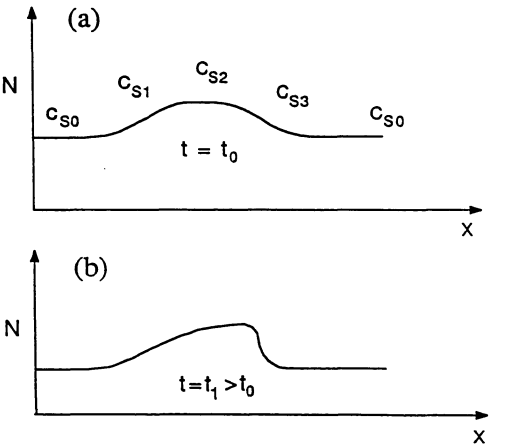

Figure 2.1 Demonstration of the non-linear steepening process for a sound pulse. Each portion of the pulse propagates at the local sound speed as shown in a) where $C_{S0} < C_{S1} < C_{S2} > C_{S3} > C_{S0}$. The sound speed varies along the pulse which leads to steepening of the leading edge as shown in b). The pulse propagates to the right.

If we interpret ω as resulting from a time derivative $(-i\partial_t)$ and k as resulting from a space derivative $(i\partial_x)$ then for a plane wave solution we get (Nicholson, p. 171, 1983)

$$\frac{\partial v}{\partial t} = -v_{ph}\frac{\partial v}{\partial x} + i\mu\frac{\partial^2 v}{\partial x^2} + \alpha\frac{\partial^3 v}{\partial x^3} + \cdots \tag{2.7}$$

The imaginary term $i\mu\partial_x^2 v$ represents a viscous dissipation and $\alpha\partial_x^3 v$ is the dispersive term. In a collisional gas the dissipation of the ordered flow energy is through ordinary Coulomb collisions which limit steepening to scales on the order of the mean free path.

If we calculate the group velocity from the dispersion relation above we get (neglecting viscosity)

$$v_g = \frac{\partial \omega}{\partial k} = v_{ph} + 3\alpha k^2 \tag{2.8}$$

As long as the wave is not experiencing strong absorption the speed at which the wave energy propagates is equal to the group velocity (Brillouin, 1960). Equation (2.8) shows that the speed of energy propagation for the disturbance is dependent on k and greater than or less than the phase velocity depending on the sign of α. Dispersion relations for the three possible cases are shown in Figure 2.2a. For a steep pulse a Fourier decomposition shows that the larger k components have greater amplitudes. When sufficiently high k modes are exited they may either propagate upstream of the pulse or be convected downstream, carrying energy away from the pulse in either case. If α is positive then standing waves may form ahead of the shock because the group velocity increases with k. If α is negative then a trailing wave train may form. When $\alpha = 0$ no wave trains are expected. Figure 2.2b shows the relationships between the dispersion relations and shock structures.

If we use the convective time derivative in the above equation then neglecting viscosity we get the Kortweg-deVries equation (*e. g.* Nicholson p. 171, 1983)

$$\frac{\partial v}{\partial t} + v\frac{\partial v}{\partial x} - \alpha\frac{\partial^3 v}{\partial x^3} = 0 \tag{2.9}$$

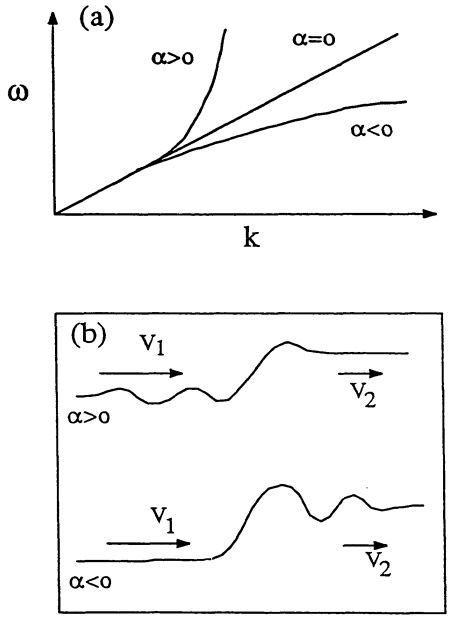

Figure 2.2 a) The three classes of dispersion and b) the shock structures characteristic of the two truly 'dispersive' cases ($\alpha \neq 0$). A leading or trailing wavetrain results from having positive ($\alpha > 0$) or negative ($\alpha < 0$) dispersion respectively.

This gives us soliton solutions (Tidman and Krall, p. 20, 1971). A soliton is a solitary wave structure that retains its shape as it propagates. It is formed through a balancing of the nonlinear steepening with dispersion. Shock solutions are obtained with the inclusion of viscosity in the equation (Tidman and Krall, p. 29, 1971).

A shock is formed when dissipation becomes adequate to convert the upstream flow energy to internal energy in the downstream fluid (with or without dispersion which can transport energy away from the shock). That is, the fluid is decelerated at the shock and its upstream coherent streaming energy is partially converted to random thermal motions downstream. If many dissipation processes are possible then whichever has the longest scale length will be the dominant one. The scale lengths for the viscous and dispersive effects can be determined by including viscosity in the Kortweg-deVries equation and assuming a steady state solution ($\partial_t = 0$ in the wave frame) leading to

$$v\frac{\partial v}{\partial x} = -\mu\frac{\partial^2 v}{\partial x^2} + \alpha\frac{\partial^3 v}{\partial x^3} \qquad (2.10).$$

One can estimate the scale lengths from this equation if we approximate the derivatives by $\partial_x = 1/L$, $\partial_x^2 = 1/L^2$, etc. Considering each term on the right side separately, we see that the viscous scale length is $L_\mu = \mu/v$ and the dispersive scale length is $L_\alpha = \sqrt{\alpha/v}$. If the two are comparable then both may affect the shock structure.

2.2 Magnetohydrodynamic Shocks

A fluid with non-zero electrical conductivity and imbedded electric and magnetic fields is much more complicated than the ordinary gas discussed in the last section. The electromagnetic momentum and energy fluxes must also be considered in the conservation laws. Maxwell's equations governing the electric and magnetic fields contribute to the

dynamics of the system. In addition, due to the presence of currents, resistivity becomes another possible dissipation process.

Let us first examine the properties of small amplitude disturbances in a uniform plasma. In the ideal MHD limit (i.e. infinite conductivity) and assuming zero viscosity and thermal conductivity, the equations for conservation of mass and momentum are (*e. g.* Landau and Lifshitz, p. 218, 1960)

$$\frac{\partial \rho}{\partial t} + \nabla \cdot (\rho \vec{v}) = 0 \tag{2.11}$$

and

$$\rho \frac{\partial \vec{v}}{\partial t} + \rho(\vec{v} \cdot \nabla)\vec{v} = -\nabla P + \frac{1}{4\pi}(\nabla \times \vec{B}) \times \vec{B} \tag{2.12}.$$

For small disturbances the entropy is constant and an equation of state may be used in place of the energy equation (Kantrowitz and Petschek, p. 153, 1966). The adiabatic power law equation of state is

$$\frac{P}{\rho^{\gamma}} = const.$$

From Maxwell's equations we have

$$\nabla \cdot \vec{B} = 0 \qquad \text{and} \qquad \nabla \times (\vec{v} \times \vec{B}) = 0 \tag{2.13}$$

which express the divergence free nature of the magnetic field and the continuity of the tangential electric field. Here we have made use of the ideal MHD assumption that the electromagnetic force on the fluid vanishes ($\vec{E} + \frac{1}{c}\vec{v} \times \vec{B} = 0$).

If these equations are linearized for perturbations in $\vec{B}$, P, ρ, and $\vec{v}$, then assuming plane wave solutions ($e^{i(\vec{k}\cdot\vec{x}-\omega t)}$) we obtain from these equations the dispersion relation with four possible solutions. Of these solutions the three corresponding to propagating modes are called the fast, intermediate, and slow modes because of their relative propagation

speeds. In terms of the phase velocities (C_F, C_I, and C_{SL} respectively) they are (*e. g.* Kennel, 1985)

$$C_I^2 = C_A^2 \cos^2\theta \tag{2.14a}$$

$$\left.\begin{matrix} C_F^2 \\ C_{SL}^2 \end{matrix}\right\} = \frac{1}{2}\left\{(C_A^2 + C_S^2) \pm \left[(C_A^2 + C_S^2)^2 - 4C_A^2 C_S^2 \cos^2\theta\right]^{\frac{1}{2}}\right\} \tag{2.14b,c}$$

where $C_A = B/\sqrt{4\pi\rho}$ is the Alfvén speed, $C_S = \sqrt{\frac{\gamma P}{\rho}}$ is the ordinary sound speed, and θ is the angle between the propagation vector $\vec{k}$ and the ambient magnetic field. It may be seen from the above equations that $C_{SL} \leq C_I \leq C_F$ and for $\theta = 90°$, $C_{SL} = C_I = 0$ (see Figure 2.3).

If we examine the perturbed quantities in the linearized equations for these dispersion relations it can be shown that fast and slow compressional waves can steepen to form shocks. Intermediate waves, as well as fast and slow rarefactions, do not steepen to form shocks (Kantrowitz and Petschek, 1966). This is most easily explained in terms of the effect of the wave on the local propagation speed as was done in the section on gasdynamic shocks. For a compression the fast and slow speeds increase while for a rarefaction they decrease. The intermediate wave does not affect the local propagation velocity. The propagation characteristics of the three MHD modes are readily seen in a Friedrichs diagram. Figure 2.3 has Friedrichs diagrams plotted for different values of β (or equivalently C_S^2/C_A^2), which show the propagation speed as a function of θ_{kB} for all three modes.

The intermediate wave is characterized by a rotation of the tangential magnetic field and velocity. Pressure and density are unchanged in this mode. For the fast and slow waves the magnetic field and velocity changes lie in the plane defined by the magnetic field ahead of the wave and the wave normal. This is referred to as the coplanarity property. The magnetic field magnitude and density perturbations are in phase for the fast mode and out of phase for the slow mode. In the slow wave the sum of magnetic and plasma pressures ($B^2/4\pi + P$) remains constant.

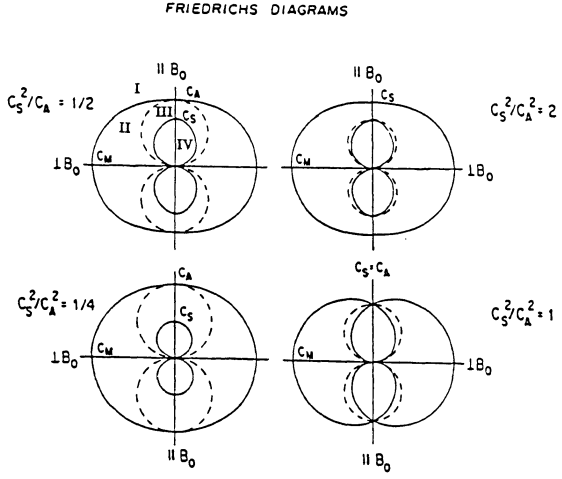

Figure 2.3 MHD Friedrichs diagrams. The Friedrichs diagram displays the dependence of the 3 MHD plane wave speeds (radial coordinate) on their angle of propagation to the magnetic field (angular coordinate) in a polar plot whose vertical axis is parallel to the magnetic field. Four cases are shown, with $C_S^2/C_A^2 = \frac{1}{4}$ and $\frac{1}{2}$ in the left-hand column and $C_S^2/C_A^2 = 1$ and 2 in the right. The fast and slow waves are indicated by solid lines and the intermediate wave by a dashed line. The magnetosonic wave propagates perpendicular the the magnetic field with the speed $C_M = \sqrt{C_S^2 + C_A^2}$. For parallel propagation, the fast and intermediate speeds equal the Alfvén speed when $C_S^2/C_A^2 < 1$, while the slow and intermediate speeds equal the Alfvén speed when $C_S^2/C_A^2 > 1$. When $C_S^2/C_A^2 = 1$, all three speeds are equal. This figure is taken from Kennel (1985).

When a fast or slow wave steepens to form a shock the entropy is no longer constant across the shock and the adiabatic equation of state is invalid. The shock jump conditions are obtained from the conservation equations for mass, momentum, and energy along with Maxwell's equations. Again in the ideal MHD limit, they are respectively (Boyd and Sanderson, p. 117, 1969):

$$\left[\rho\vec{v}\cdot\vec{n}\right] = 0 \tag{2.15}$$

$$\left[\rho\vec{v}(\vec{v}\cdot\vec{n}) + \vec{n}\left(P + \frac{B^2}{8\pi}\right) + \vec{B}\cdot\vec{n}\frac{\vec{B}}{4\pi}\right] = 0 \tag{2.16}$$

$$\left[\vec{v}\cdot\vec{n}\left(\frac{1}{2}\rho v^2 + \frac{\gamma}{\gamma-1}P + \frac{B^2}{8\pi}\right) - \frac{(\vec{B}\cdot\vec{n})(\vec{B}\cdot\vec{v})}{4\pi}\right] = 0 \tag{2.17}$$

In this format the relevant Maxwell's equations are

$$\left[\vec{B}\cdot\vec{n}\right] = 0 \qquad \text{and} \qquad \left[\vec{n}\times(\vec{v}\times\vec{B})\right] = 0 \tag{2.18}.$$

Note that for $\vec{B} = 0$ these reduce to the ordinary hydrodynamic (or Rankine-Hugoniot) jump conditions given earlier. The fast and slow mode shocks exhibit the same characteristics as their respective linear waves. That is, at least qualitatively, the relationships between changes in density, pressure, velocity, and magnetic field for the linear waves also hold for shocks (Kantrowitz and Petschek, p. 175, 1966).

The jump conditions provide some additional properties of an MHD shock. In the limit of high Mach number, the density and transverse (to the shock normal) magnetic field compression ratios (ρ_2/ρ_1 and B_{t2}/B_{t1}) approach 4. In Figures 2.4 and 2.5 the density and magnetic field jumps are plotted as surfaces in the (M_A, θ_{Bn}) parameter space as calculated from the Rankine-Hugoniot equations for an upstream beta value of $\beta = 0.5$. The change in the normal velocity component across the shock is the inverse of the density jump. The ratio of downstream internal energy to upstream flow energy approaches 15/16. The ratio of the normal velocity components is the inverse of the density compression ratio.

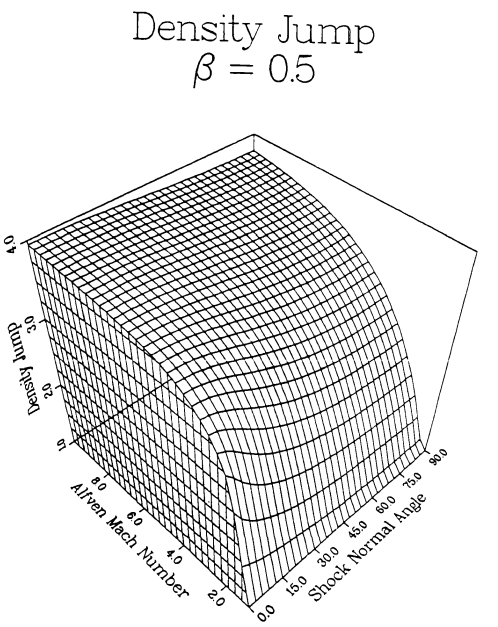

Figure 2.4 Density jump (ρ_2/ρ_1) as a function of M_A and θ_{Bn} for $\beta = 0.5$. Values are obtained from solutions to the Rankine-Hugoniot equations.

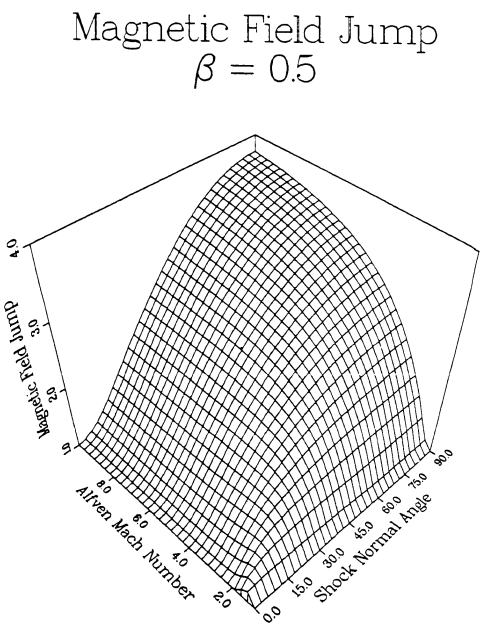

Figure 2.5 Magnetic field jump (B_2/B_1) as a function of M_A and θ_{Bn} for $\beta = 0.5$. Values are obtained from solutions to the Rankine-Hugoniot equations.

From the linear wave dispersion relations it is found that the steepening of slow waves is inhibited for high β and only fast shocks can propagate perpendicular to the magnetic field.

The regions of possible velocity transitions across the shocks are labeled on the upper left hand Friedrichs diagram shown in Figure 2.3. For the fast shock the upstream speed must lie in region I and the downstream speed must be in region II. For the slow shock the transition must be between regions III (upstream) and IV (downstream). Solutions of the conservation equations yielding other velocity transitions do exist. Coroniti (1970) performed a perturbation analysis of the shock solutions and found that all but the above mentioned transitions were unstable. He examined the hydromagnetic equations with dissipation including resistivity and Maxwell's equations (*e. g.* Landau and Lifshitz, 1960) for stability. A stable shock solution requires that the upstream (downstream) plasma be unstable (stable) to an arbitrary small perturbation. The unstable transitions are termed non-evolutionary (Anderson, 1963).

The structure of the shock transition region will be determined by the dissipative and dispersive processes that are occurring within it. For a viscous shock in a collisional gas, ordinary collisions produce the momentum transfer that decelerates the flow. However, most space plasmas are virtually collisionless since the mean free path is very long in comparison to all other scale lengths. Instead, an anomalous 'viscous' dissipation process is produced by wave particle interactions. This anomalous dissipation process is required for the shock to form.

Since a jump in the magnetic field occurs within the shock, Ampere's law implies that there must be a current layer associated with it. Thus Joule heating and other current instabilities can provide some of the dissipation. Resistive heating is important for low Mach number ($M_A \lesssim 3$) shocks. For higher Mach numbers resistivity alone cannot account for the required dissipation, so some form of anomalous viscosity is needed (Kennel,

1985). Coroniti (1970) demonstrated this by considering resistivity as the only dissipation process. He found that when the normal component of the downstream flow speed is less than the sound speed the downstream state is unstable. If the downstream state is unstable then it will continue to evolve to some other state and the conditions of the Rankine-Hugoniot equations will not be met. This implies that resistivity alone cannot prevent further steeping and a viscous subshock is necessary.

One may view a shock as two interacting streams, so stream instabilities and turbulence are often present. Particles may also be reflected from the shock producing even more complicated streaming interactions. Although dispersion is not a dissipation process, it can produce the same result by transporting energy away from the shock.

Whatever the process(es) at work to provide the shock transition is highly dependent on the parameters defining the particular shock case. For example, in the high β limit the parallel propagating fast mode wave is primarily electrostatic so it may be expected that the shock will be electrostatic. For the moderate β values to be considered in this thesis the fast mode wave is primarily electromagnetic and it will be shown that its dispersive nature dominates the physics of the shock. The most important of the parameters (listed in descending order of importance and all referring to upstream quantities) are the Mach number, the angle between the shock normal and the magnetic field (θ_{Bn}), the plasma beta (β), and the electron-ion pressure ratio (P_e/P_i). The relative importance of the parameters is also dependant upon their value which can alter the ordering from that given above.

Chapter 3. Comparison of Simulation Results with Satellite Observations

The purpose of conducting computer experiments of plasma phenomena is to learn more about the physical processes that govern these phenomena. Many of the phenomena that are manifested in the interplanetary medium cannot be reproduced in a laboratory and thus can only be observed *in situ*. The principal reason for this is that a collision free plasma of sufficient size to eliminate boundary effects from the container cannot be produced in a laboratory. Thus we have to rely primarily on theoretical modeling along with satellite observations and experiments to gain an understanding of the phenomena occurring in the interplanetary medium.

Satellite observations have shown us the existence of many phenomena and have told us much about their nature. However, observations have limitations and computer simulations can help to fill in the gaps and perhaps point towards the need for other observations that should be made. On the other hand, results obtained from a simulation must be consistent with the observations. In the first part of this chapter a comparison is made between observations of the magnetic field structures of three interplanetary shocks and the results of a computer simulation of the observed events. Also presented are the ratios of the downstream to upstream plasma density, magnetic field strength, and ion temperature (where available). In the second part some of the difficulties encountered when interpreting measurements obtained by satellites will be discussed. In particular, the Doppler shift and how it relates to the comparisons that are made will be examined.

3.1 Comparison of Simulation Results with Observations

ISEE observations of 3 interplanetary shocks, as provided by C.T. Russell, have been chosen for this analysis. The ISEE magnetometer data is sufficiently well resolved in time ($\approx$ .25 sec sampling interval) for the purposes of this study. The temporal resolution of the magnetometers exceeds that of plasma measurements which usually require on the order of 1 to 5 minutes for sampling the complete distribution function (Bame *et al.*, 1978a,b; Frank *et al.*, 1978; Anderson *et al.*, 1978; Russell *et al.*, 1983c). The high sampling rates are needed for the comparison since the shocks are convecting past the spacecraft at approximately the solar wind speed. The total system length for the simulation represents time intervals ranging from 68 to 75 seconds for the three ISEE observations. Thus the details of the magnetic field structures can be compared directly while the details of the plasma (i.e. density, pressure, velocity, etc.) cannot. However, the change in the average density and temperatures from the upstream to the downstream region can and shall be compared for those cases where results have been published.

The shock normal directions have been derived using multi-spacecraft observations as described by Russell *et al.* (1983a,b). The solar wind parameters have been determined using measurements obtained by the solar wind instrument (Bame *et al.*, 1978b) and the ISEE 1 and 2 magnetometers (Russell, 1978). The values of the parameters θ_{Bn}, M_A, β, and P_e/P_i as provided by Russell, which specify each of the three shock cases simulated, are shown in Table 3.1. The values in parenthesis represent the range of values that may be found in the published literature for these shock cases. These publications are: Kennel *et al.* (1982), Scholer *et al.* (1983), Tsurutani *et al.* (1983), Russell *et al.* (1983a,b,c), Russell and Alexander (1984), Kennel *et al.* (1984a,b), and Bavassano-Cattaneo *et al.* (1986). Also included in Table 3.1 are the average upstream number density, magnetic field magnitude,

and the shock velocity. These are needed to convert the observed and simulated results to a common scale.

Table 3.1 Parameters for the Interplanetary Shock Cases

Case	9/11/78	11/20/79	11/12/78
θ_{Bn}	32° (32° – 36°)	39° (39° – 66°)	42° (22°-50°)
M_A	1.4 (1.3-1.6)	1.7	2.9 (2.6-5.6)
β	0.23 (0.23-0.4)	0.83	0.55 (0.5-1.1)
P_e/P_i^*	2.0	1.7	3.25
$n_1(\mathrm{cm}^{-3})$	3	4	2.3
$B_1(\mathrm{nT})$	9.7	7.8	7.9
$V_{\mathrm{shock}}(\mathrm{km/s})$	436	282	606

* electron to ion pressure ratio

The variation in the values obtained for these parameters (and the changes of the plasma properties across the shock, to be shown later) come from a number of sources. Some of the observations were made from different satellites (ISEE-1, 2, or 3) and different instruments. This variation of the parameters from one satellite to another indicates that the shocks may well be evolving as they propagate through the variable solar wind. Often different techniques were used to compute shock normal angles and the Mach number (see Russell *et al.*, 1983a). Different investigators are also likely to choose different averaging intervals for estimating the upstream and downstream asymptotic values of the density, pressure, velocity, and magnetic field.

Because our simulation is one-dimensional and thus assumes a planar geometry, it is more applicable to interplanetary shocks than to the planetary bow shocks. This is because the radius of curvature of interplanetary shocks is estimated to be 2 to 3 orders of magnitude greater than the planetary bow shocks (Kennel *et al.*, 1982). For the planetary bow shocks the extent of the foreshock region and the shock associated turbulence up and downstream can be as large as the radius of curvature. The one-dimensional model excludes what may be important two-dimensional wave propagation effects. Precursor

waves generated in low Mach number shocks generally propagate at small angles to the magnetic field, $\theta_{Bk} \lesssim 20°$ (Russell *et al.*, 1983b). So the angle of the wave normal to the shock normal can sometimes be quite large. Table 3 of Russell *et al.* (1983b) shows that the majority of the wave normal angles θ_{kn} lie in the range $25° - 55°$. However, our one-dimensional simulation allows propagation only along the shock normal, so that $\theta_{kn} = 0°$. The simulation model is more fully described in Appendix A.

In order to compare the wavelength of the upstream waves for the simulation results to the observations we must convert the time series of the satellite observations to a distance scale and relate the dimensionless units of the simulation to the same distance scale. The shock velocity in the satellite frame is determined from the data using the plasma velocity vectors and best fit shock normals from multi-spacecraft observations. The method is described and the results are presented in Russell *et al.* (1983b). It is assumed that the upstream waves are phase standing with respect to the shock front in order to convert time to distance with this velocity. The scaling of the simulation results is described in the end of Appendix A.1. At the bottom of each of the figures displaying the satellite observations is the time scale in which the measurement was taken and at the top is the derived distance scale in units of the Earth's radii. At the bottom of each of the simulation figures is a scale in ion inertial lengths and at the top is the distance scale corresponding to the ion inertial length calculated from the upstream density of the observed shocks. The upstream density and average magnetic field, which determine the distance and time scales for the simulation (see Appendix A.1), for the observed shocks are listed in Table 3.1.

Figure 3.1 shows the magnetic field profiles of the September 11, 1978 shock observed by ISEE 2. Figure 3.2 shows the results of the simulation of this shock event. In both of these figures (and those to follow) the z coordinate points in the shock normal direction, the x coordinate lies in the coplanarity plane and the y coordinate is perpendicular to the shock normal and the coplanarity plane. One can see from Figures 3.1 and 3.2 that the

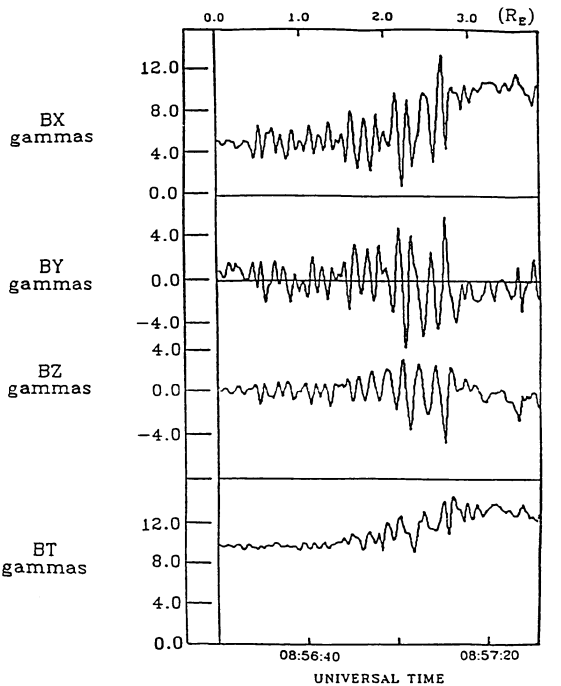

Figure 3.1 Magnetic field profiles of the interplanetary shock observed by ISEE-2 on 9/11/78 (from Mandt *et al.*, 1986).

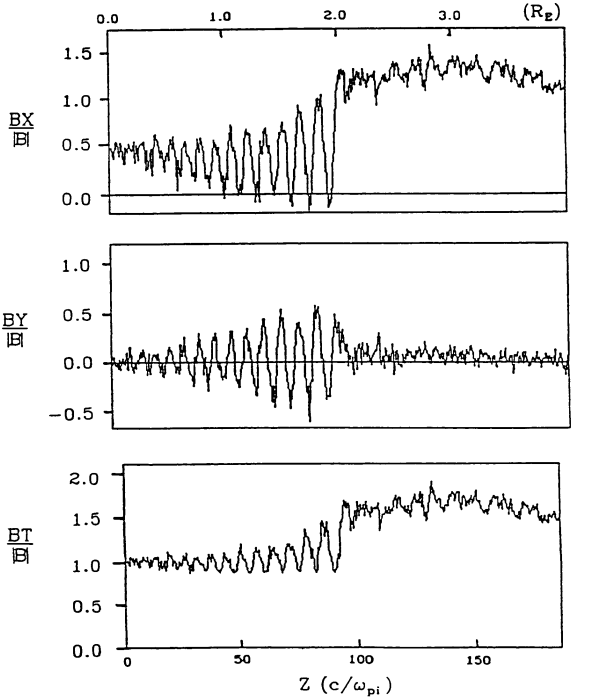

Figure 3.2 Magnetic field profiles (normalized to the total upstream field) for the simulation of the 9/11/78 shock (from Mandt *et al.*, 1986).

overall structures are very similar, with a laminar wave train preceding the magnetic ramp. One obvious difference is that B_z is constrained to be constant in the simulation while the observations show that it is not. The structure of the observations is less regular than in the simulation. This is reasonable as the conditions in the simulation are well controlled but the observed shock is propagating through a variable solar wind. It is also possible that there are wave forms in the observations that are not generated in the simulation model.

The frequency (in the solar wind rest frame), the wavelength, and the amplitude of the upstream waves compare fairly well between observation and simulation as shown in Table 3.2. The variation of the values in Table 3.2 is less than 30% for this case. The measurements were taken directly from the plots averaging over as many wavelengths as are clearly part of the wavetrain. The values of the frequency and wavelength from the satellite observations are obtained by assuming that they are phase standing in the shock frame. In the simulation these waves are phase stationary.

Figure 3.3 shows the magnetic field profiles of the November 20, 1979 shock observed by ISEE 3. Figure 3.4 shows the results of the simulation of this event. We see from these two figures that the basic structure is similar with an upstream wavetrain preceeding a rather abrupt magnetic ram. However, the quantitative comparison is much worse than in the first case. The wavelength in the simulation is just under half of that observed and the other quantities compared are off as much as 40% of the observed values. It should also be noted that in this case a much less regular structure is seen from both the observations and simulation results. The frequency, the wavelength and the amplitude of the waves are presented in Table 3.2.

Figure 3.5 shows the magnetic fields of the November 12, 1978 shock observed by ISEE 1. Figure 3.6 shows the results of the simulation of this event. As is evident in these two figures, while there are waves upstream of both the observed and simulated shocks,

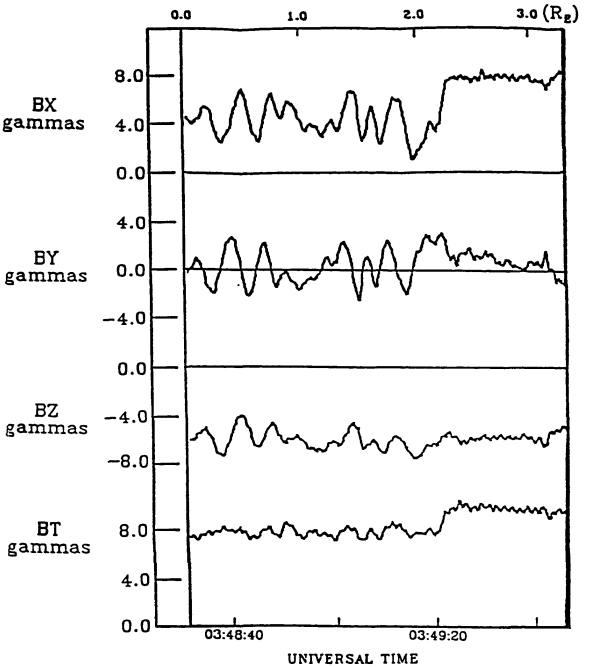

Figure 3.3 Magnetic field profiles of the interplanetary shock observed by ISEE-3 on 11/20/79 (from Mandt *et al.*, 1986).

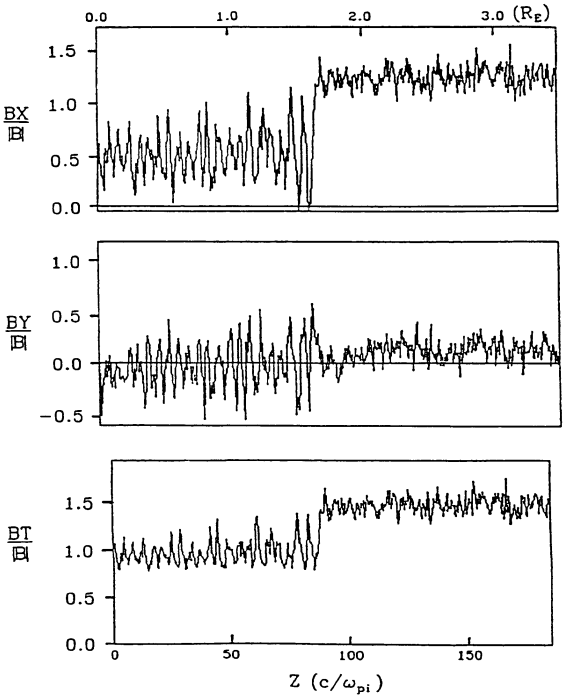

Figure 3.4 Same as Figure 3.2 but for the 11/20/79 shock (from Mandt *et al.*, 1986).

they are quite different in appearance. The only common features are the scale length of the magnetic field ramp and the large amplitude wave structure coincident with the ramp. This latter feature is seen most clearly in the plot of BY (the magnetic field component out of the coplanarity plane) in Figure 3.5 and 3.6.

In front of the observed shock there is an irregular wave train of the type generally associated with backstreaming particles. These waves have been discussed in detail by Kennel *et al.* (1984a,b). They are not part of the precursor wave structure. In fact, this shock was classified as having no observable precursor waves by Russell *et al.* (1983b). The simulation has a very definite upstream precursor type wave extending from within the shock to well upstream of the shock. However, assuming that it is phase stationary, this wave could not have been detected by the ISEE fluxgate magnetometers because the frequency of the wave is above that which could be transmitted without aliasing by the data system, and thus would have been attenuated by the antialiasing filters (Russell, 1978). The presence of this wave in the simulation supports the inference (Russell *et al.*, 1983b) that the disappearance of precursor waves above about a magnetosonic Mach number (M_{MS}) of 1.8 was due to the precursor wave frequency increasing above the magnetometer passband. We also note that Kennel *et al.* (1984a) found a high frequency (1 Hz) modulation in the upstream region. Table 3.2 lists the properties of the simulated waves.

In these three interplanetary shock events a reasonably good qualitative agreement is seen between the observed and simulated magnetic field profiles. Variations between the individual cases that occur in both the simulation and observations are also noticed. In the first case we have a very well defined, laminar wave train and extended ramp. In the second case the ramp is sharper and the wave train is less well defined. In the third case there appears to be no laminar wave train, but a large amplitude wave of a few wavelengths appears to stand in the magnetic ramp. These variations between the three cases are seen in the simulations (apart from the wavetrain of case 3 as discussed earlier) as

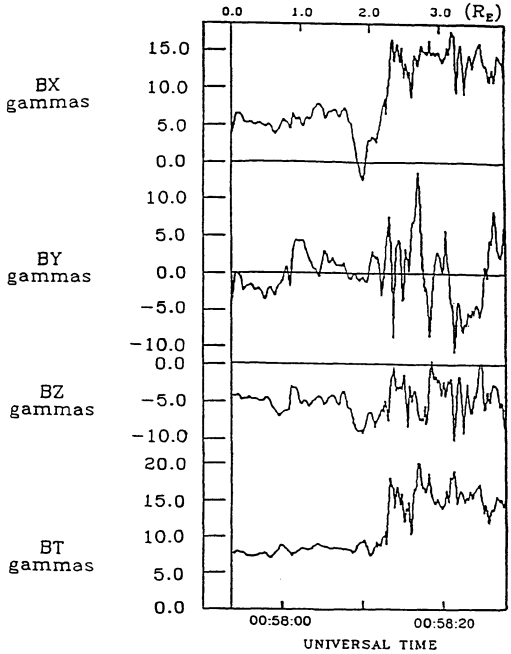

Figure 3.5 Magnetic field profiles of the interplanetary shock observed by ISEE-1 on 11/12/78 (from Mandt *et al.*, 1986).

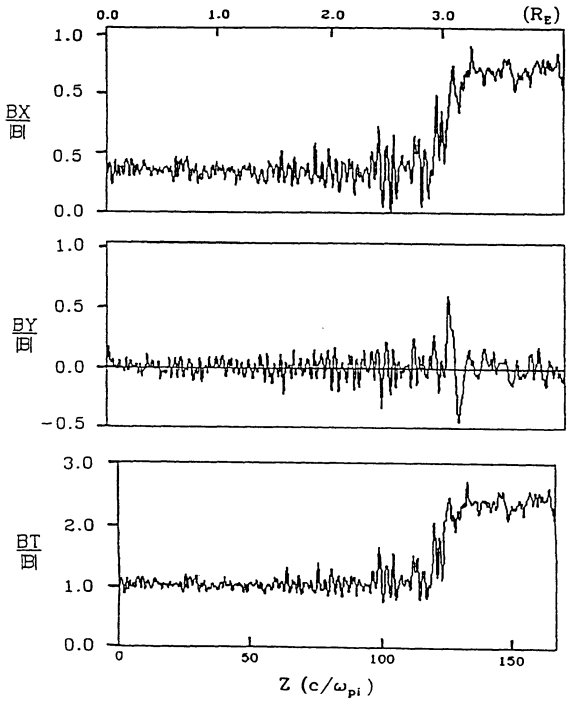

Figure 3.6 Same as Figure 3.2 but for the 11/12/78 shock (from Mandt *et al.*, 1986).

Table 3.2 Comparison of Results

	ISEE Data	Simulation
	Interplanetary Shock of September 11, 1978	
λ, km	1300	910
ω_{SW}, Hz	0.26	0.19
A_{max}, γ	12.0	12.0
$\Delta B/B$	0.4	0.4
n_2/n_1	1.3-1.4	1.5
B_2/B_1	1.2-1.4	1.5
T_{i2}/T_{i1}	1.1-1.3	1.5
	Interplanetary Shock of November 20, 1979	
λ, km	1200	530
ω_{SW}, Hz	0.13	0.22
A_{max}, γ	6.0	8.5
$\Delta B/B$	0.4	0.5
n_2/n_1	—	1.5
B_2/B_1	1.4	1.4
T_{i2}/T_{i1}	—	1.7
	Interplanetary Shock of November 12, 1978	
λ, km	—	380
ω_{SW}, Hz	—	0.9
A_{max}, γ	—	10.0
$\Delta B/B$	1.0	1.3
n_2/n_1	2.2-3.0	2.4
B_2/B_1	2.2-2.3	2.4
T_{i2}/T_{i1}	5.0	5.3

Here λ is the wavelength, ω_{SW} is the solar wind rest frame frequency, $A_{\max}$ is the maximum of the wave amplitude, $\Delta B/B$ is the ratio of the change in the magnitude of the magnetic field to the average upstream value, n_2/n_1 is the downstream to upstream density ratio, B_2/B_1 is the magnetic field ratio, and T_{i2}/T_{i1} is the ion temperature ratio. λ, ω_{SW}, A_{max}, and $\Delta B/B$ are obtained from the figures. n_2/n_1, B_2/B_1, and T_{i2}/T_{i1} are taken from published literature (see text for references). Where two numbers are given they represent the range of values found.

well as the observations. For the quantitative comparison, the wavelength and frequency of the simulated waves were consistently off by as much as a factor of 2. The peak wave amplitude and magnetic field jump compared quite well. From Table 3.1 one can see that all three cases lie within a fairly narrow range of the parameter space spanned by M_A, θ_{Bn}, β, and P_e/P_i. Besides the Mach number we found the shock structure to be most sensitive to β. Cases 1 and 2 are very similar, but case 2 has a higher beta value and a less laminar magnetic field profile. This variation in the structure with beta is expected. For very low beta the plasma is strongly directed by the magnetic field. As beta increases the plasma exerts a greater influence on the magnetic field. Since the particles act as sources for the magnetic field, random thermal motions of the particles add more noise to the magnetic fields. We have also run the second case with $\beta = 1$ and actually had better agreement with the observations than in the run presented here. For that run the values obtained are $\lambda = 740$ km, $\omega_{SW} = 0.16$ Hz, and $A = 6.2\gamma$.

Also listed in Table 3.2 are the ratios of the downstream to upstream average values of the density, magnetic field, and ion temperature. The observational values were taken from the same set of publications from which the shock parameters were obtained. One can see that while some of the values from the simulation lie in the observed ranges, most of them are greater than those observed. The larger downstream to upstream ratios and shorter precursor waves indicate that the simulated shocks may be stronger (have a greater Mach number) than those observed. All of the values mentioned above for the simulated results lie within 15% of the observed values.

We note that there are several sources of uncertainty in the observed plasma parameters. For example, in the derivation of the shock normals, Russell and Alexander (1984) estimate that while 66% of the 16 interplanetary shock normals they studied were determined to better than 4° , 20% were in error greater than 8°. The individual magnetic field values are accurate to 0.1γ, but the accuracy of the averaged magnetic field values depends

on the fluctuation level. The plasma density is uncertain by about 10%. Finally, we have not included the effects of alpha particles on the density or pressure. Thus the improved agreement for case 2 with $\beta = 1$ is understandable. The range of values listed in Table 3.1 can give an indication of their uncertainty. The value of the density and magnetic field magnitude determine the temporal and spatial scaling for the simulation (see Appendix A.1).

In all three cases the wavelengths of the upstream waves are shorter in the simulation, with the second case being the worst. The simulation also overestimates the jump in the magnetic field in all cases. These values are also listed in Table 3.2. One would expect that variations due to uncertainties in the plasma parameters (density, temperature, field magnitude and direction) used to define the particular case and to scale the simulation would be less systematic. However, the nature of these uncertainties is not simple. Another likely source for the discrepancies is due to the assumptions upon which the simulation model is based. The electrons are treated as a massless fluid, thus any effects due to the electron dynamics are lost. Also, the ions in the simulation are treated as 'macro particles'. That is, each 'particle' in the simulation actually represents a large number of actual ions. This may well affect the scaling of the phenomenon being simulated.

It is noted that not only are the observed wavelengths longer than the simulated cases, but both of these are longer than what is predicted for a phase standing whistler wave. Part of the reason for this may be due to nonlinear effects as will be discussed in Chapter 5. Another cause may be due to the assumed geometry of the shock and the upstream wave propagation. Figure 3.7 shows the two most likely geometries for the shock-precursor structure. Figure 3.7a shows the usual configuration where the phase fronts parallel the shock surface. The expected wavelength for a phase standing whistler from the cold plasma

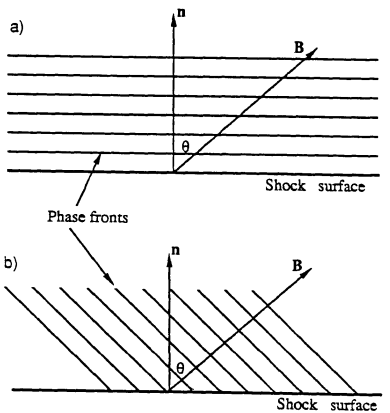

Figure 3.7 Two realizations of the possible geometries for a phase standing precursor wave ahead of a shock. The two cases sketched show a) the wave normal parallel to the shock normal, and b) the wave normal parallel to the upstream magnetic field. The shock normal vector, **n**, points towards the upstream region.

dispersion relation with this geometry is

$$\lambda_0 = 2\pi c/\omega_{pi} \frac{\cos\theta_{Bk}}{\sqrt{M_A^2 - 1}} \tag{3.1}.$$

Figure 3.7b shows a situation where the phase fronts have normals parallel to the magnetic field. Under this assumption the relation for the predicted wavelength of a phase standing whistler wave is given by

$$\lambda_0' = 2\pi c/\omega_{pi} \frac{\cos\theta_{Bk}}{\sqrt{M_A^2 \cos^2\theta_{kn} - 1}} \tag{3.2}.$$

Table 3.3 lists the wavelengths measured from the satellite and the simulations as well as the wavelengths predicted for a phase standing whistler wave based on the geometries of Figure 3.7a and b where $\theta_{Bk} = \theta_{Bn}$ for case a) and $\theta_{Bk} = 0$ and $\theta_{kn} = \theta_{Bn}$ for case b). The one dimensional assumption of the simulation enforces the structure of Figure 3.7a upon it. The possibility that a physical shock may follow the structure of Figure 3.7b is also supported by the observation by Russell *et al.* (1983b) who find that the precursor wave propagation is highly field aligned.

Table 3.3 Comparison of Upstream Wavelengths*

Case	λ_{obs}	λ_{sim}	λ_0	λ_0'
9/11/78	1300	910	850	1300
11/20/79	1200	530	410	830
11/12/78	—	380	260	500

* all in kilometers

3.2 Interpretation of Satellite Observations

The interpretation of data obtained from observations by satellites poses a very difficult problem. One must determine whether one is observing temporal variations, spatial

variations, or some combination of both. To unambiguously resolve the characteristics of a single convecting and propagating signal may be impossible. To further complicate the issue, what is usually observed is a multitude of waveforms (including turbulence) that are not necessarily linearly superimposed. Extracting information from this sort of data is very difficult. In this section some of the most fundamental problems for the interpretation of satellite data will be listed. The problem most relevant to this study, namely the Doppler shift, will be discussed in more detail. Then I shall consider how it relates to the observations of the previous section.

The first and simplest obstacle in determining the nature of an observed signal is the Doppler shift. In general the signal source, the medium through which it propagates, and the observer will all be in motion relative to one another and this affects the relationship between the signal that is generated and what is observed. Another major difficulty in a magnetized plasma is that the index of refraction is anisotropic. The propagation characteristics of waves depend on the orientation of the wave relative to the magnetic field. In addition, pace plasmas tend to be inhomogeneous. Variations in the plasma density, temperature, and composition as well as the magnetic field also alter the propagation characteristics of a signal. Also, as was mentioned at the beginning of this section, what is generally observed is a superposition of many different waveforms.

The problem of the Doppler shift will now be discussed. To simplify things somewhat, one can work in a reference frame where the medium is assumed to be at rest and consider just the motion of a source and an observer through it. If the source is at rest or we are only interested in the properties of the signal as it propagates through the medium, then the rest frame frequency (ω_r) is obtained from the observed frequency (ω_{obs}) by the simple relation

$$\omega_r = \omega_{obs} + \vec{k} \cdot \vec{v}_{obs} \tag{3.3}$$

where $\vec{v}_{obs}$ is the velocity of the observer (spacecraft). Thus one must know the wavelength and propagation direction (or the phase velocity) of the signal as well. This can only be inferred from simultaneous, multi-point observations or by assuming knowledge of the dispersion relation. Multi-spacecraft observations of interplanetary shocks are discussed by Russell and Alexander (1984) and references therein.

If one is interested in the characteristics of a moving source then the situation is much more complicated. The frequency in the medium is given by the same Doppler shift relation if the medium and observer are at rest. The general expression (in one-dimension) is

$$\omega_r = \omega_{obs}\left[\frac{V_{ph} + V_m - V_s}{V_{ph} + V_m - V_{obs}}\right] \tag{3.4}$$

where V_{ph} is the phase velocity of the wave, V_m is the velocity of the medium and V_s is the source velocity, all relative to some inertial frame of reference. In general the wavelength will also be altered by relative motion between the source and medium. What is often of interest is not a single isolated signal but rather a spectrum of signals. This is usually represented as the power spectral density. To Doppler shift the power spectrum one must integrate the observed spectrum over a frequency interval. In general this requires knowledge of the dispersion relation. For the simple case of a power law spectrum the shape is unchanged but the amplitude is altered (Olson, 1970).

Interplanetary shocks were chosen for this comparative study because the velocities of the medium, the wave, and the observer are fairly well known. Knowing the velocity of the waves of course depends on the assumption that the waves are phase standing in the shock frame. The fact that the shocks are convecting quickly past the shock makes the determination of the upstream wavelength more reliable. In the case of the Earth's bow shock, the shock oscillates back and forth with a velocity comparable to that of the satellite. Under these conditions a single spacecraft cannot determine the shock velocity.

The Doppler shift could also be important due to two and three dimensional propagation effects. The discrepancies between the observed, simulated, and predicted upstream wavelengths indicate that the geometry usually assumed for a phase standing precursor (with the shock and precursor normals aligned) may be incorrect. Assuming that $\theta_{Bk} = 0$, the predicted wavelength is closer to the observed value. Also, given the one dimensional limitation of the simulation model, the shorter wavelengths seen there are expected.

3.3 Summary

In this chapter a comparison was made between three interplanetary shock events and computer simulations of these events. Qualitatively, the comparison between each case was reasonable. Quantitatively, the ratios of the upstream to downstream density, ion temperature, magnetic field field intensity, and the precursor wave amplitude were within 30% of the observations. However, the frequency and wavelength of the precursor were off by as much as 50% in one case. This may be explained by Doppler effects due to the geometry of the observed shock versus that of the simulation model. The usual assumption is that the wave normal vector of a phase standing precursor wave will be parallel to the shock normal. Observations show that the precursor waves tend to propagate along the magnetic field. The one dimensional simulation model restricts wave propagation to be along the shock normal direction. The expected wavelength of a phase standing whistler with its wave normal parallel to the magnetic field is much closer to the observed value than that from the simulation and may explain the discrepancy between the simulation and observations.

Chapter 4. The Electrostatic Potential and Electron Equation of State

The inclusion of a finite electron pressure in the hybrid code provides a means of studying equations of state for the electrons and the corresponding electrostatic potentials. In this chapter we shall examine the role of this electric field and the cross shock potential jump expected for three electron equations of state. In the first section the equation for the electric field and the estimated potential jump are presented. The equations of state to be considered and the predicted pressure changes and potential jumps due to them are presented next. Finally, the simulation results, the results of this chapter, and how both relate to a physical shock will be discussed.

4.1 The Electrostatic Field

In the one-dimensional hybrid model, self-consistent electrostatic electric fields can only exist in the direction of the simulation axis (electrostatic fields transverse to the axis can be externally imposed). If the electron pressure is $P \neq 0$, then the resulting electrostatic electric field is given by

$$E_z = -(\vec{v}_e \times \vec{B})_z - -\frac{1}{\rho}\frac{\partial P_\parallel}{\partial z} + \frac{1}{\rho}\frac{\partial}{\partial z}\left(\frac{P_\parallel - P_\perp}{2B^2}B_t^2\right) \tag{4.1}$$

where the subscript e for the electron pressures has been dropped and $\vec{B}_t = (B_x, B_y, 0)$ is the magnetic field transverse to the simulation axis. Equation (4.1) is derived from the results of Appendix A and is seen to be composed of the z-component of the motional electric field and gradients of the electron pressure terms.

Since we are examining the expected potential jumps due to the electron pressures as predicted by the Rankine-Hugoniot equations (with $\vec{v} \parallel \vec{B}$) we will ignore the $\vec{v}_e \times \vec{B}$ term.

Also, this motional electric field is perpendicular to $\vec{v}$, and should do no work on the plasma (assuming a steady state). From the definition $\vec{E} = -\vec{\nabla}\phi$ we can use a finite difference approximation in one-dimension to obtain for the potential jump across the shock

$$\Delta\phi = -E_z \Delta z = \frac{1}{\rho}\Delta P_{\parallel} - \frac{1}{\rho}\Delta\left(\frac{P_{\parallel} - P_{\perp}}{2B_t^2}B^2\right) \qquad (4.2).$$

The above expression assumes that the electric field is uniform over Δz and would correspond to a monotonic shock profile. Equation 4.2 also assumes that the density is constant, which it is not. However, we use the upstream value of the density for this calculation which should give an upper limit for the potential jump.

4.2 The Electron Equations of State

Three equations of state for the electrons are examined: an isotropic power law, the Chew-Goldberger-Low or CGL equation of state (Chew *et al.*, 1956), and the corrected CGL (CCGL) equation of state (Hada *et al.*, 1986). The CGL and CCGL equations allow for anisotropic electron pressures which may strongly influence the ion dynamics through the second term on the right of equation (4.2).

An isotropic power law equation of state is the most simple, nontrivial formulation to consider and is given by $P/\rho^{\gamma} = constant$. A value of $\gamma = 5/3$ represents adiabatic compression while $\gamma = 1$ represents isothermal compression (or expansion, but we are interested in shocks which are compressive). Values of $\gamma > 5/3$ indicate an increase in entropy while values of $\gamma < 5/3$ indicate a local loss of entropy (see Appendix B). The CGL equation of state represents the conservation of two adiabatic invariants for the electrons, the magnetic moment and the entropy. It is given by

$$\frac{P_{\perp}}{\rho B} = \mu_0 \qquad \text{and} \qquad \frac{P_{\perp}^2 P_{\parallel}}{\rho^5} = S_0 \qquad (4.3).$$

The CCGL equations conserve magnetic moment but assume that the electrons behave isothermally along magnetic field lines. Therefore, the equation defining the parallel pressure in the CGL equations is replaced by an isotropic power law with $\gamma = 1$. The reason for this modification of the CGL equations is the high mobility of the electrons along field lines which allows for rapid thermalization parallel to $\vec{B}$. This may be especially important for quasi-parallel shocks.

We will examine the electron pressure and electrostatic potential change across the shock for each equation of state by considering how the magnetic field and density (which define the electron pressures) behave. To do this we will first consider the potential jump due to the changes predicted by the Rankine-Hugoniot equations. Then we shall consider the effects of the detailed structure of the shock. The changes in the density and magnetic field across the shock as predicted by the Rankine-Hugoniot equations is shown in Figures 2.4 and 2.5 as a function of the Alfvén Mach number and the shock normal angle (θ_{Bn}).

For the isotropic power law the change in pressure is given by

$$P_2 = R_\rho^\gamma P_1 \tag{4.4}$$

where $R_\rho \equiv \rho_2/\rho_1$ is the ratio of the down to upstream densities. Under the assumption of quasi-neutrality the electron density is nearly identical to the ion density in the simulation. This yields for a potential jump

$$\Delta\phi_{RSO} = (R_\rho^\gamma - 1)kT_1 \tag{4.5}$$

where kT_1 is the upstream electron thermal energy. The value of the numerical factor $(R_\rho^\gamma - 1)$ ranges from 3 to 9.1 for $\gamma = 1$ to 5/3 and assuming $R_\rho = 4$ (the high Mach number limit).

For the CGL equation of state the perpendicular and parallel pressure changes are given by

$$P_{\perp 2} = R_\rho R_B P_1 \qquad \text{and} \qquad P_{\parallel 2} = \frac{R_\rho^3}{R_B^2} P_1 \tag{4.6}$$

The upstream pressure is assumed isotropic and $R_B \equiv B_2/B_1$ is the ratio of the downstream to upstream magnetic field strengths. The electrostatic potential jump is then

$$\Delta\phi_{CGL} = (\frac{R_\rho^3}{R_B^2} - 1)kT_1 - (R_\rho^2 - R_B^3)(R_B^2 - 1)\frac{R_\rho}{R_B^2}kT_1 \tag{4.7}$$

For the CCGL equation we replace the parallel pressure term with a term appropriate to an isothermal power law. The change in the parallel pressure is then the same as for the isotropic power law with $\gamma = 1$. The potential jump is

$$\Delta\phi_{CCGL} = (R_\rho - 1)kT_1 - (1 - R_B)(R_B^2 - 1)\frac{R_\rho}{R_B^2}kT_1 \tag{4.8}$$

The potential jumps calculated from these equations are plotted in units of the upstream electron thermal energy (kT_1) as surfaces in the Alfvén Mach number and shock normal angle parameter space (Figs. 4.1–4.3). The isotropic case, shown in Figure 4.1, follows the density profile as expected with a maximum potential jump of $9.1kT_1$. The CGL case, shown in Figure 4.2, predicts a large potential jump for large shock normal angles and its value peaks at about $150kT_1$. The potential jump at smaller angles is also large with a peak at about $60kT_1$. However, the potential jump has a trough at about $\theta_{Bn} = 20°$ where it goes negative. The potential predicted by the CCGL equation, shown in Figure 4.3, has a monotonic structure and magnitude comparable to the isotropic equation. The values of the potential jump increase with increasing Mach number and θ_{Bn} peaking at about $12.5kT_1$.

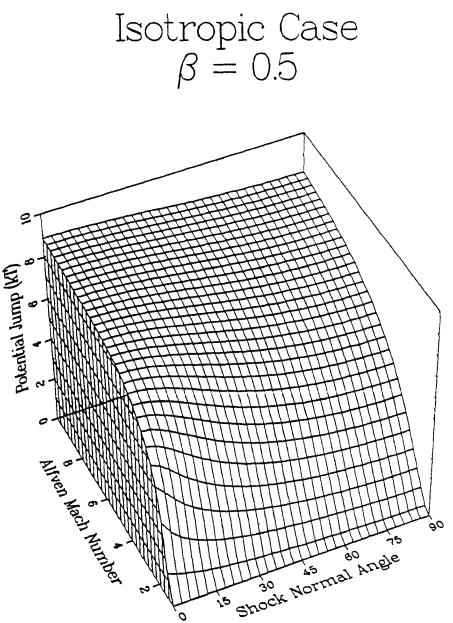

Figure 4.1 The electrostatic potential jump (in units of the upstream electron thermal energy) predicted by the Rankine-Hugoniot equations for the isotropic equation of state. The potential jump is plotted as a surface in the (M_A, θ_{Bn}) parameter space.

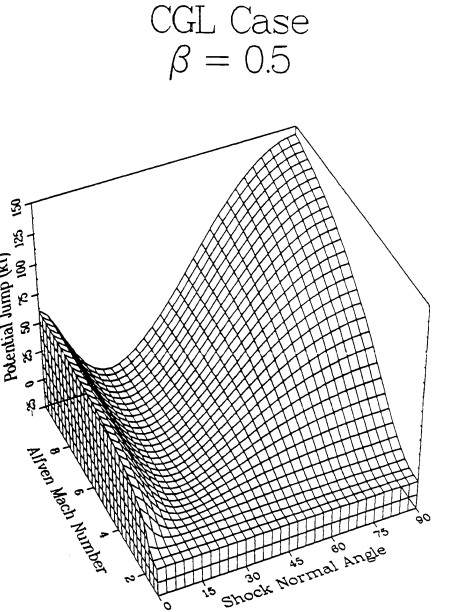

Figure 4.2 Same as Figure 4.1 but for the CGL equation of state.

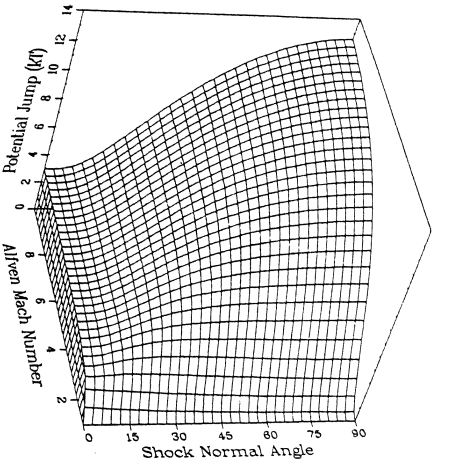

Figure 4.3 Same as Figure 4.1 but for the CCGL equation of state.

4.3 Discussion and Conclusions

The simulation results using these three equations of state show very little difference at low Mach numbers ($M_A < 3$). However, above $M_A \approx 3$ the shock structure becomes increasingly erratic with increasing Mach number for the CGL and CCGL equations of state. The potential jump across the shock transition is sometimes positive and sometimes negative. Large fluctuations in the potential occur throughout the simulation. The shock structure at high Mach numbers behaves reasonably only for the isotropic equation of state. For the CGL equation of state, the reason is evident from examining the expected pressure changes and resulting potential jump across the shock. The results show that the CGL equation of state produces a large anisotropy leading to electric fields that destroy the shock structure at high Mach numbers. The predicted behavior of the CCGL equation of state seems reasonable; the reason for its breakdown is due to the microstructure of the shock itself. The actual shock structure also affects the results of the CGL equation.

The fact that the CGL equation of state predicts potential jumps that would accelerate the ions through the shock indicates that they are inappropriate for a shock model. A negative potential jump is unphysical, as it would accelerate rather than decelerate the ions through the shock. Also, the magnitude of the predicted potential jump is excessive in the CGL case. When one considers the actual structure of the quasi-parallel shock the situation becomes even worse. While the Rankine-Hugoniot equations predict that $R_B \approx 0$ for small shock normal angles, both simulations and observations show that a value of $R_B \gtrsim 2$ would be appropriate due to the waves associated with the shock. Also, the small scale fluctuations in ρ and $\vec{B}$ can be in phase and out of phase in different regions of space. This results in a very erratic potential structure which is totally unrealistic.

The isotropic equation of state depends only on the density and the resulting potential jump behaves reasonably throughout the parameter space. At high Mach numbers one

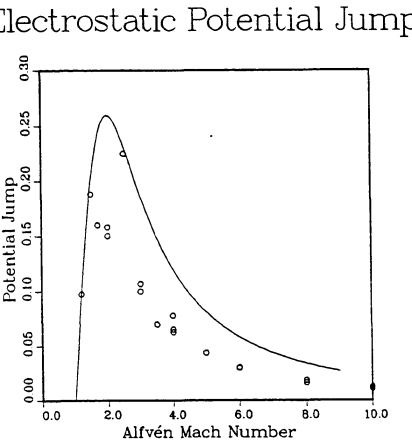

Figure 4.4 Electrostatic potential jump normalized to the upstream flow energy $\frac{1}{2}Mv_n^2$ as a function of the Alfvén Mach number for $\beta_e = 0.25$ and $\theta_{Bn} = 10°$. The curve is the Rankine-Hugoniot prediction. The circles are results from the simulation.

would expect an isotropic pressure due to the turbulent structures within the transition region. The potential jump follows the electron pressure. The potential jump, normalized by the upstream flow energy $Mv_n^2/2$, is plotted in Figure 4.4 as a function of the Alfvén Mach number for $\beta_e = 0.25$ and $\theta_{Bn} = 10°$. Also plotted on the figure are the results from simulation runs with these same parameters. The potential jump is normalized to the flow energy in this figure because that is the convention often used to present observational and theoretical results. One can see from the figure that the simulation results are consistently less than that predicted by the Rankine-Hugoniot equations but exhibit the same trend. That the simulation results are lower than the theoretical values is reasonable since the assumptions of equation (4.2) imply that it represents an upper limit. The magnitude of the potential jump in the simulation peaks at about 25% of the incoming ion energy near $M_A = 2$ and decreases with increasing Mach number. This is expected as the magnitude of the potential jump is limited by the change in the electron thermal energy across the shock (which is limited by the density jump) while the ion energy is essentially unbounded as the Mach number increases.

In summary, three different electron equations of state have been examined, the adiabatic power law, the Chew-Goldberger-Low equation, and the corrected CGL. The resulting electrostatic potentials were studied using the predictions of the Rankine-Hugoniot equations and testing the electron equations of state in the simulation. The predicted potential jump for the CGL equation of state was negative for certain ranges of parameter space and therefor unphysical. The predicted potential jump for the isotropic power law and the CCGL equation are reasonable. At low Mach numbers ($M_A < 3$) all three equations produce the same results. At higher Mach numbers the anisotropy terms in the CGL and CCGL equations result in large electric fields which disrupt the simulation. The simulation results using the adiabatic power law equation of state follow follow the predicted potential jump quite well.

Chapter 5. Scale Lengths of Quasi-Parallel Shocks

In this chapter the results of a survey of the quasi-parallel collisionless shock as a function of the Alfvén Mach number are examined. Simulations were performed with a shock normal angle of 10° and upstream plasma beta of $\beta = 0.5$. The wavelengths of the upstream and downstream waves were measured and estimates made of the scale lengths of the magnetic field, density and velocity jumps. These were normalized to the natural scale lengths of the plasma: the ion inertial length (c/ω_{pi}), the ion thermal gyro-radius ($\rho_{1,2}$ upstream and downstream respectively), and the ion streaming gyro-radius ($\rho_s = V_s/\Omega_i$), and plotted as functions of the Alfvén Mach number. The intent of this study is to see how the characteristic lengths of the shock relate to the natural scale lengths of the upstream and downstream plasmas.

The wavelengths of the upstream and downstream waves were measured by averaging over as many wavelengths as were clearly a part of the wavetrain. The values for the scalelengths were hand-fitted estimates of the length over which the principal change in the quantity occurs (or approximately where the largest gradients exist). In the process of conducting this study it was noted that there appeared to be a large variability in the scale lengths with time. In order to account for this as much as possible, the data set used in this study was constructed from as many time samples as were available for each case. Typically, a simulation is run until $T = 50\text{–}150\Omega_{in}^{-1}$ with diagnostic plots output every $10\text{–}20\Omega_{in}^{-1}$. In Figure 5.1, showing the upstream wavelength, the average value for each Mach number is plotted. In the remaining figures, the average as well as the minimum and maximum values for each case are plotted. A total of 25 cases are represented in this study.

5.1 Upstream and Downstream Wavelengths

Figure 5.1a shows the wavelengths of the upstream waves as a function of the Alfvén Mach number. One can see the expected decrease of the wavelength with increasing Mach number. This is because the propagation velocity of the waves increases with decreasing wavelength and the longer waves cannot stand in the flow at higher Mach numbers. The expected wavelength of a phase standing whistler as a function of Mach number is (Tidman and Krall, 1971)

$$\lambda_0 = \frac{2\pi}{k_0} = \frac{2\pi c}{\omega_{pi}} \frac{\cos\theta_{Bn}}{\sqrt{M_A^2 - 1}} \qquad (5.1).$$

In Figure 5.1 the upstream wavelength as a function of this expected wavelength is plotted. The solid line on the figure is the least squares fit of the data to a straight line given by $\lambda = 1.2\lambda_0 + 0.4$. The correlation coefficient is 0.992 and the rms error is 0.3, which is less than the deviation from the expected fit. The average deviation of the simulation data to the expected fit is 1.5. The dashed line has a slope of unity and represents the theoretical prediction of (5.1). One can see that the simulation results produced upstream waves with consistently longer wavelengths than predicted by the cold plasma linear dispersion relation by up to a factor of about 2 for higher Mach numbers. It was noticed from the simulation runs that at very early times in a simulation run the wavelength was shorter and much closer to the predicted value.

The discrepancy between the simulation results and that predicted by theory may be due to one or both of two effects. In the region upstream of the principal ramp the flow is somewhat reduced. Since the wave phase velocity must equal the flow velocity and the phase velocity decreases with increasing wavelength, this would allow a longer wavelength wave to phase stand ahead of the shock. The other cause may be the nonlinear nature of the waves. Since the magnetic field is substantially increased due to the wave fields in

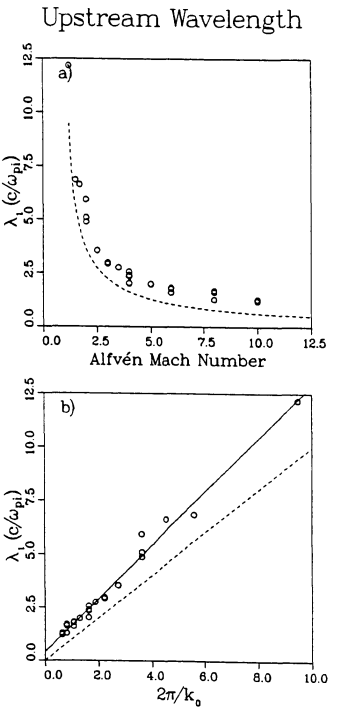

Figure 5.1 Wavelengths of the upstream waves as a function of a) the Alfvén Mach number and b) the wavelength of the expected phase standing whistler. The circles are the results of simulation runs, the solid line is a least squares fit to the data, and the dashed line is the predicted value.

the upstream region while the density increases only slightly the local Alfvén speed will be greater than the background value. Since the wave speed is proportional to the Alfvén speed and the wave number, if the phase velocity is to be constant the wavelength must increase as the Alfvén speed increases. This would also allow a longer wavelength wave to phase stand in the upstream flow.

Figure 5.2 shows the downstream wavelengths as a function of Mach number normalized by a) the upstream ion inertial length (c/ω_{pi}), b) the upstream thermal gyro-radius (ρ_1), c) the downstream gyro-radius (ρ_2), and d) the streaming gyro-radius (ρ_*). These figures show that the downstream wavelengths are longer than any of the natural scale lengths of the shocks. In Figure 5.2a, in which the normalization (c/ω_{pi}) is independent of M_A or β_i, there appears to be a trend towards a longer wavelength at higher Mach numbers. It is not expected that the downstream waves would scale with the upstream gyro-radius but we include Figure 5.2b here to be consistent with Figures 5.3, 5.4, and 5.5. Figure 5.2c shows that the downstream wavelength begins around $10\rho_2$ at low Mach numbers and appears to asymptote to $\sim 5\rho_2$ at higher Mach numbers. Figure 5.2d shows the same behavior for the streaming gyro-radius normalization as in Figure 5.2c with the magnitude reduced by a factor of 2.

However, the different normalizations do not appear to better organize the data. The reduction in scatter at high Mach numbers in 5.2c and 5.2d is due to the increase in the normalization length (ρ_2 and ρ_*) with Mach number. If the wavelength truly scaled with the thermal or streaming gyro-radius then there should also be a reduction in scatter of the data points at lower Mach numbers but this is not observed. It might be noted that any dependency on the upstream ion beta could show up as a variation in the figure in Figure 5.2b (as well as in Figures 5.3b, 5.4b, and 5.5b). This is because the thermal gyro-radius is a function of β for a given Mach number. However, no variation of significance is seen other than an increase in the scatter of the points.

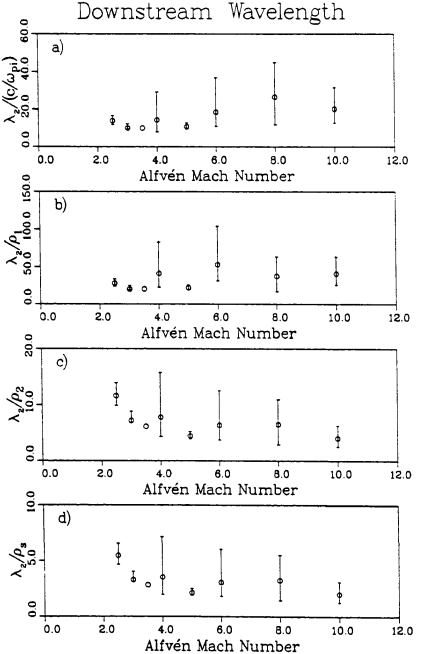

Figure 5.2 The downstream wavelengths as a function of the Alfvén Mach number normalized to a) the upstream ion inertial length (c/ω_{pi}), b) the upstream thermal gyro-radius (ρ_1), c) the downstream gyro-radius (ρ_2), and d) the streaming gyro-radius (ρ_s). The circles are the average values obtained at different times in simulation runs and the error bars show the range of values measured.

5.2 Scale lengths of Magnetic Field, Density, and Velocity Jumps

Figure 5.3 shows the scale length of the jump in the magnetic field magnitude as a function of Mach number with the same normalizations as in Figure 5.2. These figures show that the magnetic field jump does not scale to any of the natural scales of the plasma. In general, the minimum length for the magnetic field jump is approximately the wavelength of the upstream waves. The magnitude of the magnetic field as computed from the unsmoothed magnetic fields is used to estimate the length of the magnetic field jump. The presence of the upstream waves tends to obscure the magnetic field transition in many cases yielding much larger scale lengths. Thus, the lower bounds of the data points plotted in Figure 5.3 may be the best estimate of the actual magnetic field jump but this will be fairly sensitive to how the data is filtered. For the analysis performed for this study the length of the magnetic field jump is bounded below by the upstream wavelength and is much less than the downstream wavelength.

Figure 5.4 and 5.5 show the density and velocity jump scale lengths, respectively, as a function of the Alfvén Mach number with the same normalizations as in Figure 5.2. It can be seen that the plots in both figures are very similar. This is to be expected since the normal flow velocity must follow the inverse of the density in order to satisfy the continuity equation. The scale length of the plasma (density and velocity) jump is larger than the natural scale lengths of the shocks but does not appear to be better organized by any of them. Figure 5.4a shows that the jump can be, but is not always, much broader in the vicinity of the transition Mach number ($2 \lesssim M_A \lesssim 4$). Figure 5.4d shows that the shock width is on the order of ten times the streaming gyro-radius for very low Mach numbers and is slightly larger than the streaming gyro-radius for higher Mach numbers. This is in agreement with the observations of Scudder *et al.* (1984).

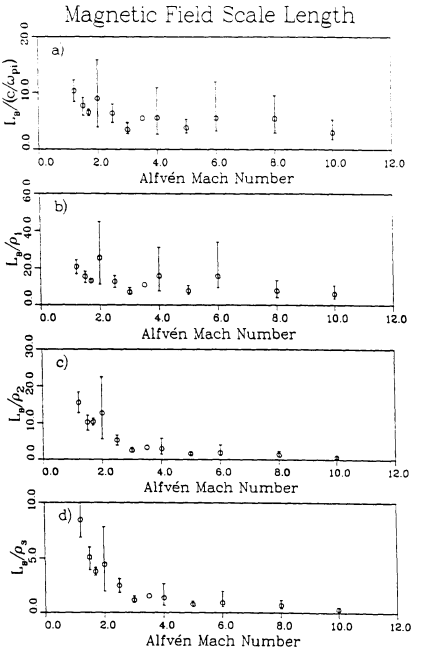

Figure 5.3 Magnetic field jump scale length versus the Alfvén Mach number. The same normalization used in Figure 5.2 is also used here.

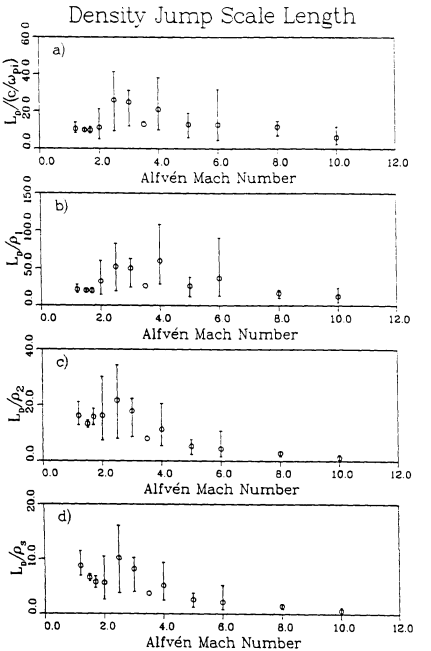

Figure 5.4 Density jump scale length versus the Alfvén Mach number. The same normalization used in Figure 5.2 is also used here.

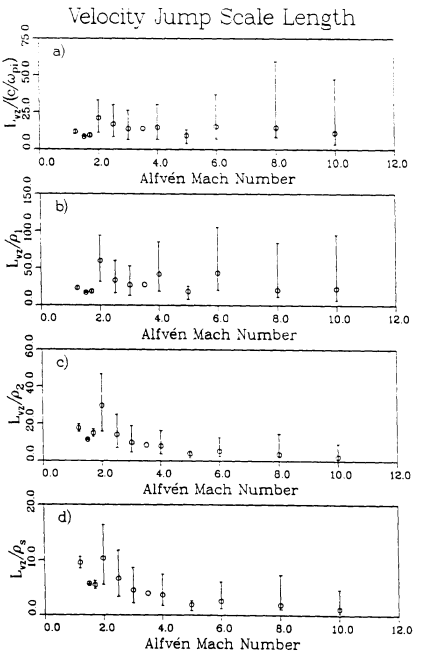

Figure 5.5 Normal velocity jump scale length versus the Alfvén Mach number. The same normalization used in Figure 5.2 is also used here.

5.3 Summary and Discussion

The wavelength of the upstream wavetrain exhibits the same trend as is expected for a phase standing whistler from the cold plasma dispersion relation. However, the wavelength of the simulated waves is consistently larger by up to a factor of 2 for the highest Mach numbers considered. This may be due to one or both of two physical effects. One is the slight slowing of the plasma in the upstream region. This effectively reduces the Mach number in the region where the waves exist. Figure 5.1 shows that the phase standing wavelength is longer for lower Mach numbers. The other is a nonlinear effect due to the wave fields themselves. The presence of the wave increases the magnitude of the magnetic field and hence the magnitude of the wave phase speed. Since the phase velocity is proportional to the wave number this too allows a longer wave to phase stand. The problem of the geometry and relating these results to actual shocks as discussed in Chapter 3 should not arise here. This is because $\cos\theta_{Bn} \approx \cos\theta_{kn} \approx 1$ so equations 3.1 and 3.2 are nearly identical.

The downstream wavelength is greater than any of the natural plasma scale lengths. What determines the wavelength is not known but the study by Kan and Swift (1983) suggests that their generation is due to the firehose instability. The work by Quest (1988) also indicates that these waves are generated by either the firehose instability, if one is considering the plasma to be a fluid, or two stream instabilities, if one is examining the kinetic behavior of the plasma. The two are merely different approaches to the same problem. That these waves could significantly scatter or heat the ions is unlikely since their wavelengths are too long (see Chapter 6 and Appendix C). However, they may well contribute to the isotropization of the ion temperature.

The scale length of the magnetic field jump is on the order of the wavelength of the upstream wavetrain and much smaller than the downstream wavelength. The jump

length is around 5 times the streaming gyro-radius at low Mach numbers and less than the streaming gyro-radius at higher Mach numbers ($M_A \gtrsim 3$). Based on the results presented in Appendix C this means that the ions see the change in the magnetic field as a fairly abrupt discontinuity at higher Mach numbers. This adds weight to the ion heating arguments that will be presented in Chapter 6.

The plasma jump is seen to be larger than the natural scale lengths of the shock and can be quite variable, particularly near the transition Mach number ($2 \lesssim M_A \lesssim 4$). Part of the reason for this is that above the transition Mach number the shock begins to exhibit a time dependent behavior in the plasma jump. The plasma transition may steepen to approximately the same scale length as the magnetic field jump and then may spread out many times wider before steepening once again. The nature of this time dependent behavior is not clearly established and will require a much more detailed analysis of the simulation results than has been attempted here.

In summary, wavelength of the upstream precursor wave follows that expected for a phase standing whistler. The principal jump in the magnetic field is also controlled by the dispersive properties of the fast mode wave. Above a transition Mach number of $M_A \approx 3$ long wavelength waves appear in the downstream region which may be due to streaming instabilities. The scale length of the jump in the plasma density and normal velocity component is large ($L \approx 10\text{–}20c/\omega_{pi}$) and variable, particularly near the transition Mach number ($2 \lesssim M_A \lesssim 4$).

Chapter 6. Ion Heating

Ions play the dominant role in the heating at the quasi-parallel wave due to their large inertia (as compared to the electrons). The electrons heat resistively and are important only at low Mach numbers ($M_A < 2$). At higher Mach numbers resistivity is insufficient to provide the required dissipation in the shock layer. It is the ion, rather than the electron, dynamics that interact with the dispersive waves generated by the shock because the wavelength of these waves is much greater than the electron gyro-radius and the frequency is well below the electron gyro-frequency. These waves are an integral part of the shock structure and play an important role in the dissipation process.

In this chapter the ion heating in the quasi-parallel collisionless shock is examined. In the first section a summary of the existing theories is presented. This is followed by the simulation results from which a power law equation of state is empirically derived. The simulation results are first described in general and then two representative cases, one subcritical and one supercritical, are examined in more detail. This critical Mach number is the one at which the firehose instability criterion is first met and occurs around $M_A \approx 2.5$. It is found that the ion heating may be described by a power law equation of state with different exponents for the upstream and downstream parts of the transition region. Then it is proposed that, based on test particle calculations, most of the ion heating can be accounted for by finite larmor radius effects when the ions encounter the precursor wave fields and the magnetic ramp. This model for the ion heating is seen to be consistent with the results of the simulation. The main results will then be recapitulated and how they relate to other theories and observations will be discussed.

6.1 Existing Theoretical Work

Several mechanisms have been proposed for the ion heating in the quasi-parallel shock. However, how much of the heating is produced by what mechanism and under what conditions is as yet unresolved. The earliest theories relied on the firehose instability in high beta plasmas to generate MHD turbulence and thereby produce the needed dissipation. Parker (1961) described the shock as being two counterstreaming ion beams which are firehose unstable (under appropriate conditions). Moiseev and Sagdeev (1963) considered a high beta ($\beta \gg 1$) shock where the fast mode degenerates into an ion sound wave. They argued that an ion sound wave would nonlinearly steepen to Debye length scales where ion reflection would produce an irreversible ion sound wave train. In the absence of collisions the heating would only be parallel to the magnetic field so this would again lead to a firehose instability.

Many authors have worked on theories of high beta parallel firehose shocks at low Mach numbers (Kennel and Sagdeev, 1967; Kennel and Petschek, 1968; Berezin and Sagdeev, 1969; Galeev and Sagdeev, 1970 and Sagdeev, 1979). Numerical calculations support the general features of these theories (Auer and Volk, 1973). They also indicate that an ion sound subshock would be required at higher Mach numbers (Jackson, 1983). Simulations have shown the generation of Alfvénic turbulence with the onset of the firehose instability at about $M_A = 3$ (Kan and Swift, 1983). However, this earlier version of the simulation code assumed a zero temperature, zero mass electron fluid so an ion sound subshock could not exist.

These firehose shock theories did not include the upstream wave structures or the energetic backstreaming particles. Both observations and simulations show that these are likely to play an important role in the quasi-parallel shock heating process (Bavassano-Cattaneo *et al.*, 1986; Kan and Swift, 1983; Quest *et al.*, 1983). Lee (1983) proposed a

self-consistent model whereby backstreaming ions generate the hydromagnetic wave fluctuations which in turn scatter and/or accelerate the backstreaming ions as well as heat the bulk plasma. It has also been proposed (Kan and Swift, 1983; Quest *et al.*, 1983) that significant ion heating is produced by the non-resonant and non-adiabatic scattering of the ions as they move through the low frequency whistler waves in the upstream portion of the transition region.

Other authors have performed simulations and proposed theories for strong quasi-parallel shocks. Biskamp and Welter (1972) proposed an electrostatic two-ion-beam instability as responsible for dissipation. This instability is excited nonlinearly by the whistler wave potential. Forslund and Freidberg (1971), Forslund *et al.* (1972), and Forslund *et al.* (1980) proposed a parametric decay of the large amplitude whistler waves into an ion acoustic wave and another whistler wave as the basic dissipation mechanism.

More recently Quest (1988) has examined in some detail the mechanism of the ions being heated by electromagnetic waves which are generated by streaming instabilities. He considers the shock interface itself as well as reflected or leaked backstreaming ions as candidates for the free energy source for the streaming instabilities. The wave characteristics predicted by his theory match the results of simulations that he performed quite well. The cases he considered were $\theta_{Bn} = 0°$, $\beta = 1.5$ and $1.5 \leq M_A \leq 10.02$. In this study the same waves that Quest observed were also seen. However, here a different role is attributed to them in the ion heating process. The short wavelength waves in the upstream region that are discussed here are not mentioned by Quest.

6.2 Macroscopic Characteristics and Equation of State

In this chapter the results of a set of numerical simulations are used to examine the macroscopic characteristics of the ion heating in quasi-parallel shocks. The simulation

model is described in Appendix A. The electron fluid is assumed to be isotropic and follow the isentropic-adiabatic equation of state. The first part of this section describes the analysis performed. This will be followed by the simulation results.

The macroscopic characteristics of the ion heating process are examined by plotting the logarithm of the ion pressure versus the logarithm of the density in a hodogram format. This type of presentation will show any power law dependence in the ion heating (i.e. $P = C\rho^{\gamma}$). For an isothermal process $\gamma = 1$ and for an isentropic-adiabatic process $\gamma = 5/3$ (assuming three degrees of freedom). From these plots of the simulation results straight line fits to the data are approximated to provide estimates of the exponent γ in the power law. It should be pointed out that if one is interested in how the temperature varies, this too can be obtained from the pressure-density plots. From the definition $P = nkT$ the above equation becomes $T = C'\rho^{\gamma-1}$. Thus the plots of the logarithm of the temperature versus the logarithm of the density would be identical to the pressure-density plots with the slope, γ, replaced by $\gamma - 1$.

In the analysis performed and the results to be presented, the ion distribution function is handled two ways for each case considered. In the first method, all ions are included in the moment calculations. In the second method all ions in the upstream region with $|\vec{v} - \langle\vec{v}\rangle| > 2v_{th}$ are removed from the moment calculations. The calculations are performed using the total distribution function because this is what would be measured by a satellite and would also provide the results that are pertinent to single fluid theories. The reason for using a truncated distribution function is to examine what is happening to the bulk of the incoming distribution separate from reflected or leaked backstreaming particles. Counterstreaming particles contribute large values to calculations of the second moment (pressure). It is also unclear whether these backstreaming particles were scattered locally or leaked from the downstream region. Using the reduced distribution function enables a better determination of the local heating. The location of the 'upstream' region is

determined by the point where the average density exceeds the upstream density by a factor of 1.3 to 2.0 (depending on the particular case). This is where the principal density jump occurs.

Simulations were performed for a number of quasi-parallel ($\theta_{Bn} = 10°$), moderate beta ($\beta = 0.5$) shock cases. The general characteristics of all cases will be described first. Then two cases, a sub-critical ($M_A = 2$) and a super-critical ($M_A = 4$), will be discussed in some detail. These cases are chosen to be representative of the different structures in the shock transition region as functions of the Mach number. Other aspects of the $M_A = 2$ and $M_A = 4$ shock cases have been discussed previously (Kan and Swift, 1983; Mandt and Kan, 1985). These authors suggest that the ion heating mechanism in the quasi-parallel shock can be attributed to non-adiabatic scattering of the ions by the large-amplitude wave fields generated in the shock transition region. This scattering mechanism leads to heating of the ions whose gyro-radius and gyro-frequency are comparable to the wavelength and frequency of the large-amplitude, right-handed whistlers in the transition region.

At very low Mach numbers ($M_A \lesssim 1.5$) the upstream wave train has a long wavelength (λ_u) and small amplitude. The heating is coincident with the density jump and occurs over a distance of the order of λ_u. The parallel pressure jump is greater than the perpendicular pressure jump and gradually isotropizes downstream. As the Mach number increases ($M_A \approx 2$) the wavelength decreases (to be expected since the whistler wave exhibits positive dispersion, see Figure 2.2), the amplitude of the waves increases (as does the magnetic field jump), and heating begins to occur upstream of the density ramp as ions are scattered by the waves.

Above a critical Mach number of $M_A \approx 2.5$ another change occurs in the shock structure. Kan and Swift (1983) showed that near this Mach number the shock becomes firehose unstable. The heating becomes more isotropic and a downstream wavetrain begins to appear with a wavelength much longer than that in the upstream region. This downstream

wave train generally has a fairly constant amplitude and a right handed polarization. The constant amplitude of the waves in the downstream region indicates that there is no strong interaction between them and the plasma. At times both upstream and downstream waveforms appear to mix within the transition region. The upstream waves are phase standing in the shock frame while the downstream waves get convected downstream with the flow. These characteristics continue to be present at larger Mach numbers.

Above this transition Mach number, the heating in the upstream region continues but becomes a less important part of the total heating as the Mach number increases. However, it still provides a major contribution to the overall heating process. The principal heating occurs at the beginning of the density transition and is usually complete before the density peak is reached. Changes in the pressures occur on scales of the order of the upstream wavelength. Changes in the magnitude of the magnetic field also occur on this scale (note that these 'changes' in the pressure, magnetic field, density, etc. do not, in general, represent the total shock transition, as sometimes the total transition is completed in multiple steps). The density transition is occasionally as short as the magnetic field and pressure changes, but usually it is many times longer. The character of the 'heating' in the downstream region for all Mach numbers is a gradual isotropization of the plasma.

We shall now consider the two cases in detail. Figure 6.1 shows profiles of the magnetic field magnitude, the density, and the parallel and perpendicular (relative to the local magnetic field) pressures for the $M_A = 2.0$ case. The flow is from left to right and the shock layer remains quasi-stationary in the simulation frame. The simulation coordinate is expressed in units of the upstream ion inertial length (c/ω_{pi}) and all values plotted are normalized to the upstream value. In this figure all ions are included in the moment calculations. One can see from the figure that well upstream of the principal shock jump there is a large pressure increase near $z = 40c/\omega_{pi}$ which is accompanied by very little change in the density. At this point the wave amplitude also experiences a sudden increase.

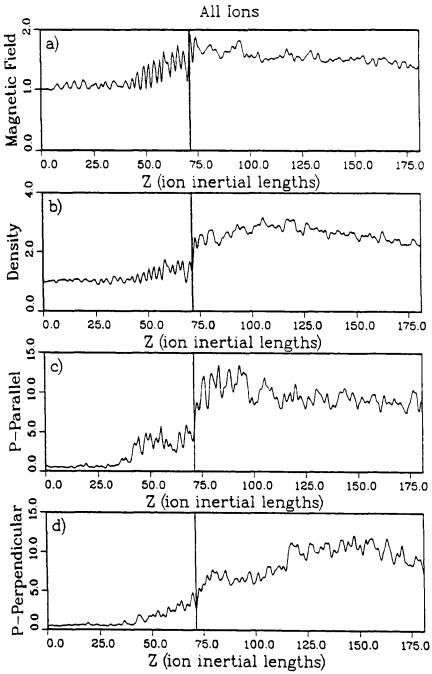

Figure 6.1 Profiles of a) magnetic field magnitude, b) plasma density, c) parallel ion pressure, and d) perpendicular ion pressure for the $M_A = 2.0$ case at time $T = 60\Omega_{in}^{-1}$. (Ω_{in}^{-1} is the inverse of the gyro-frequency based on the normal magnetic field component). The parallel and perpendicular directions are relative to the local magnetic field direction. All quantities are normalized to their asymptotic upstream values.

The heating here is anisotropic with $P_{\parallel} > P_{\perp}$ and much greater than the isentropic-adiabatic rate of $\gamma = 5/3$. The fluctuations in the magnetic field and density in the upstream region are characteristic of the whistler mode wave where the density and $|\vec{B}|$ are in phase.

In Figure 6.2 are plotted the parallel and perpendicular temperatures for the $M_A = 2$ case. From this figure it appears that the principal temperature increase occurs in the upstream region and little if any occurs at the main density ramp. The large temperatures in the upstream region are due in part to backstreaming particles which make large contributions to the calculation of the second moment of the distribution function. Figure 6.5 shows that with these particles removed the principal temperature increase for the bulk of the incoming plasma actually occurs at the main density jump. Also included in Figure 6.2c is a scatter plot of the normal component of the ion velocities. This shows the backstreaming particles as well as the thermalization (spreading) of the main part of the distribution in the upstream region.

Figure 6.3 shows plots of the logarithm of the pressures versus the logarithm of the density for the parallel and perpendicular pressures respectively. All of the information in Figures 6.1b and c is contained in Figure 6.3a and similarly for Figure 6.1d with Figure 6.3b. From these figures one can see the two stages of heating, the upstream (left side of plots) and downstream (right side of plots) sides of the transition region. Two lines are drawn on each figure for reference purposes representing $\gamma_{1\parallel} = 14$, $\gamma_{2\parallel} = 1.2$, $\gamma_{1\perp} = 6.5$, and $\gamma_{2\perp} = 1.4$ for the upstream parallel, downstream parallel, upstream perpendicular, and downstream perpendicular exponents respectively. These lines are an eyeball fit to the data in each region. These plots indicate that in the first stage the heating is predominantly parallel. For reference, curves with slopes of $\gamma = 5/3$ and $\gamma = 1$ are drawn in the lower right corner of each figure.

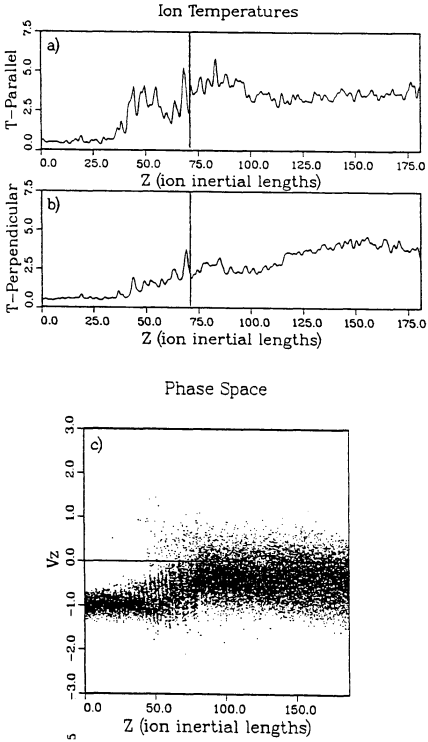

Figure 6.2 Plot of the a) parallel and b) perpendicular temperatures and c) a scatter plot of the normal velocity component for the $M_A = 2$ case.

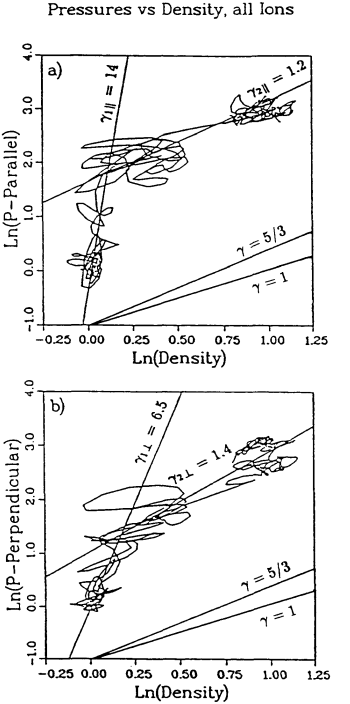

Figure 6.3 Plot of the logarithm of a) the parallel pressure, and b) the perpendicular pressure versus the logarithm of the ion density in hodogram style format for the $M_A = 2.0$ case. Reference curves for power law exponents with $\gamma = 5/3$ and 1 are drawn in the lower right-hand corner.

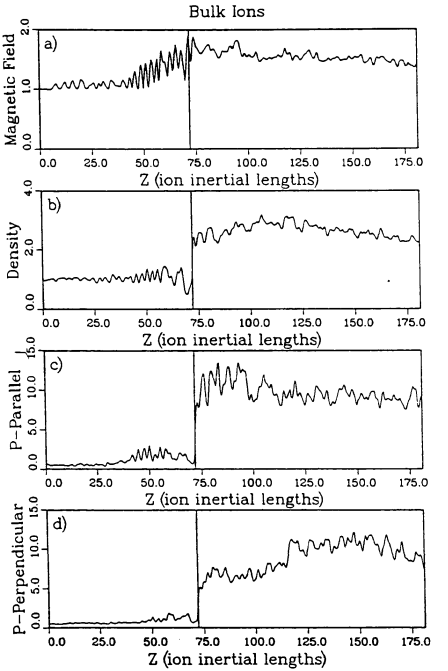

Figure 6.4 Same as Figure 6.1, but with backstreaming and energetic particles removed from the calculations in the upstream region.

In Figure 6.4 the results shown in Figure 6.1 are reproduced with the backstreaming and energetic ions removed from the calculations in the upstream region. One can see by comparing Figure 6.4 to Figure 6.1 that while the magnitude of the increase is substantially less than that in Figure 6.1, the pressures still experience a large increase well upstream of the main shock jump. This demonstrates that the bulk of the plasma is heated to some degree in the upstream region. The large pressures there are not due solely to high energy or counterstreaming particles. Figure 6.5 shows the temperatures calculation from the bulk of the distribution. Here the principal temperature change is at the main ramp. Figure 6.6 shows hodograms of the pressures and densities for this calculation. Comparison with Figure 6.3 shows that the result of using a reduced distribution function is to slightly reduce the value of the exponent in the upstream region. The value characterizing the downstream region has increased and the heating at both stages appears to be more isotropic. However, the distinction of the upstream region having the larger exponent remains.

Figure 6.7 shows profiles of the magnetic field, density, and pressure components for the higher Mach number case ($M_A = 4$). The pressure profiles show large upstream pressures in the upstream region and the sudden heating where the density begins to increase. The heating in this case has $P_{||} > P_{\perp}$ in the upstream region but results in a fairly isotropic downstream distribution. Figure 6.8 shows the parallel and perpendicular temperatures. Again the large temperatures upstream are primarily due to backstreaming particles and the largest temperature jump occurs at the main ramp as can clearly be seen in Figure 6.11 where the temperatures for the bulk of the distribution are plotted. The phase space scatter plot in Figure 6.8c also shows a very definite spreading in the bulk of the distribution in the upstream region. Figure 6.9 shows the hodograms of the pressures and density for this case. One can see that the pressures increase an order of magnitude before the density experiences a significant change. At the principal density jump the compression is between adiabatic and isothermal.

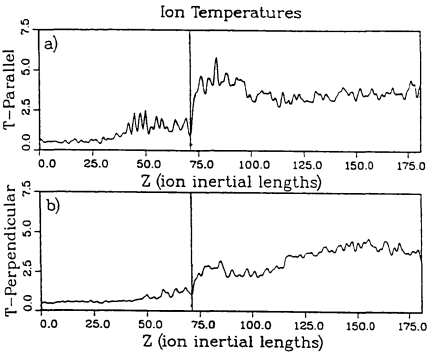

Figure 6.5 Plot of the a) parallel and b) perpendicular temperatures of the bulk of the ion distribution function.

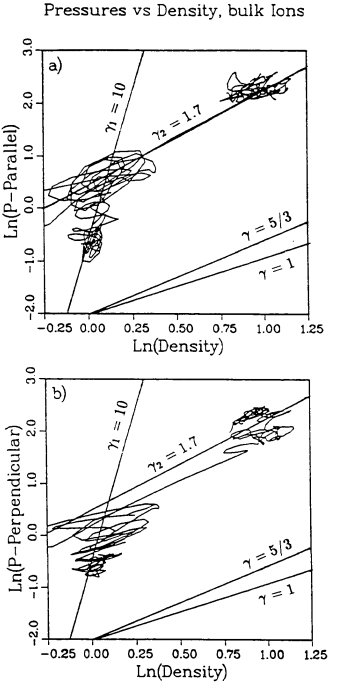

Figure 6.6 Same as Figure 6.3, but with backstreaming and energetic particles removed from the moment calculations in the upstream region.

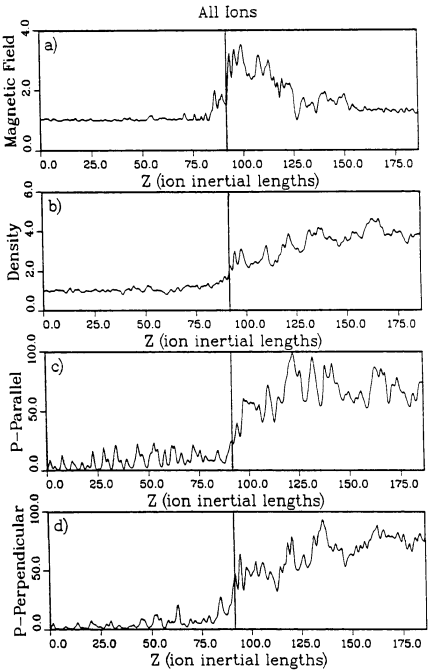

Figure 6.7 Same as Figure 6.1, but for the $M_A = 4$ case at $T = 50\Omega_{in}^{-1}$.

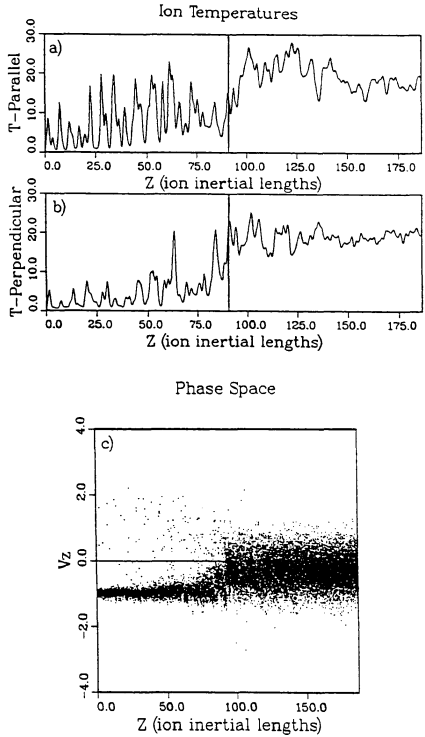

Figure 6.8 Same as Figure 6.2, but for the $M_A = 4$ case.

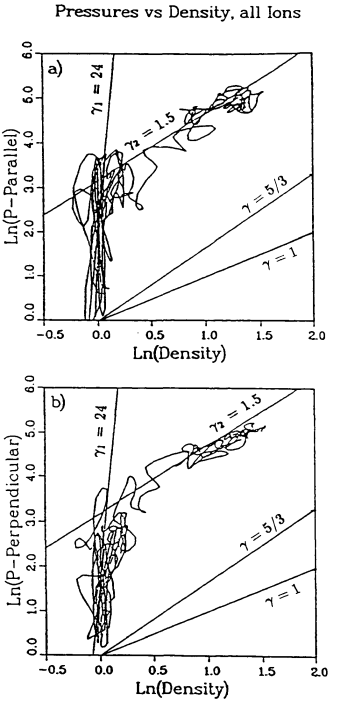

Figure 6.9 Same as Figure 6.3, but for the $M_A = 4$ case.

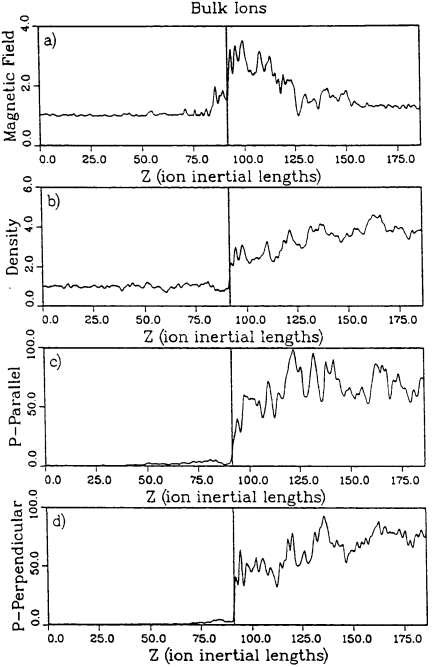

Figure 6.10 Same as Figure 6.4, but for the $M_A = 4$ case.

Figure 6.10, 6.11, and 6.12 show the same profiles for the bulk of the upstream particles. The pressures in the upstream region here are clearly much less than for the full distribution and are more isotropic. The exponents one obtains from Figure 6.12 are somewhat reduced in the upstream but the same for the downstream region as compared to Figure 6.9. The signature of the two stages of heating with that in the upstream being much greater than the adiabatic rate and that in the downstream being near the adiabatic rate remains.

Figure 6.13 shows the results of determinations of the power law coefficients for a number of simulation runs. The results of using the full and reduced distribution functions are indicated by the circles and triangles respectively. The values of the power law coefficient were determined from plots such as those in Figures 6.3, 6.6, 6.9, and 6.12. For those cases where the exponent for the parallel and perpendicular pressures differed that average is plotted. The lines plotted are least squares fits to each of the sets of points. The slopes for the lines representing the upstream exponents are 5.7 and 1.5 and the correlations were 0.96 and 0.82. In the downstream the slopes were both -1.1 and the correlations -0.73 and -0.41. The complete ion set showed the higher correlation. This shows that the exponent characterizing the heating in the downstream part of the transition seems to be somewhere between adiabatic and isothermal and appears to be independent of the Mach number for all but very low Mach numbers.

How the exponent of a power law equation of state relates to entropy and heat production is demonstrated in Appendix B. It is seen that for a compression, if $\gamma > 5/3$ then entropy is increasing while if $\gamma < 5/3$ it is decreasing. A measure of the change in entropy between two states is the ratio of temperatures. However, this does not provide much information on how much heating is occurring. A measure of how much heating is occurring in a change of state is the difference in temperature between them. So the results obtained from Figures 6.3, 6.6, 6.9, 6.12, and 6.13 indicate that most of the entropy production

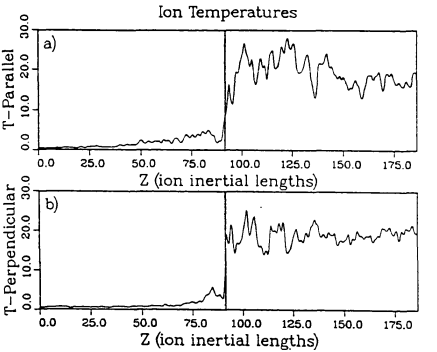

Figure 6.11 Same as Figure 6.5, but for the $M_A = 4$ case.

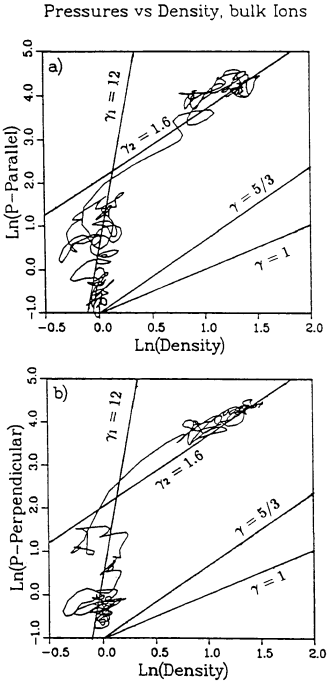

Figure 6.12 Same as Figure 6.6, but for the $M_A = 4$ case.

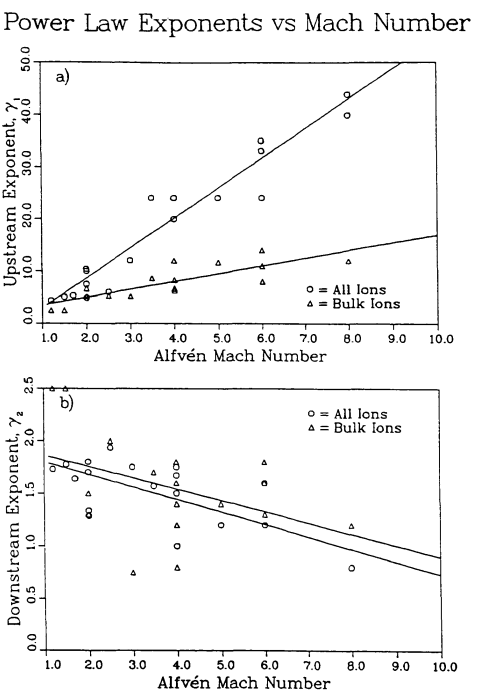

Figure 6.13 Power law exponents as a function of M_A for a) the upstream, and b) the downstream portions of the shock transition region. The solid lines represent the least squares estimates to the points plotted.

occurs in the upstream part of the shock transition region. In the downstream part the entropy often decreases, but the net change in entropy for the entire transition is always positive. Since it is the difference in temperatures that determines the amount of heating, Figures 6.5 and 6.11 show that most of the heating occurs at the principal ramp which we have considered to be in the downstream part of the shock transition region.

6.3 Ion Heating Mechanism

Most theories put forth to explain the ion heating in the quasi-parallel collisionless shocks rely on instabilities and wave particle interactions to provide the dissipation required by the Rankine-Hugoniot equations. The quasi-parallel shock abounds with different wave structures (Russell and Hoppe, 1983), many of which may relate directly to the physical processes in the shock. It is suggested here that the heating can be accounted for by the dispersive character of the whistler wave and finite larmor radius effects. The dispersive nature of the whistler wave controls the scale length of the magnetic field structures at the shock. The finite larmor radius effects result in non-adiabatic motion and heating of the ions as they traverse the magnetic field structure of the shock.

The interaction of individual particles with various static magnetic field structures is examined in Appendix C using test particle calculations. It is found that the interaction of a particle with a jump in the magnetic field magnitude over a scale length $L_B \lesssim \rho_s$ can result in a significant amount of heating and could even reflect the particle. The Rankine-Hugoniot equations predict the maximum ratio of the downstream thermal velocity to the upstream flow velocity to be 0.612. For the simple, idealized model with a perfect discontinuity this can be accomplished by a change in the magnetic field angle of 33° as can be seen in Figure C1.2 in Appendix C. Examination of the simulation results show that the change in magnetic field angle across the shock is approximately 30° at low Mach

numbers and can be up to 70° at higher Mach numbers. If the magnetic field jump at the shock is narrow enough, finite larmor radius effects can thus easily account for the required heating. The results of Chapter 5 show that at higher Mach numbers $L_B \lesssim \rho_s$ so the particle behavior is similar to that for a perfect discontinuity. At low Mach numbers $5\rho_s \lesssim L_B \lesssim 10\rho_s$, but much less heating is required so that the non-adiabatic ion motion can still account for it.

The presence of the upstream wave train in the shock increases the amount of heating that can be produced as is demonstrated in Appendix C. However, the time independent magnetic field structure left the transmitted particles gyro-phase bunched if the wavelength and magnetic ramp scale length were less than 1-2ρ_s. It is entirely possible that the temporal fluctuations and spatial non-uniformities that occur in space plasmas and the simulation model could account for the additional phase angle scattering needed to produce a truly thermal distribution. It is also possible that a gyro-phase bunched distribution will lead to instabilities which randomize the phases. The simulation results need to be re-examined for evidence of gyro-phase bunched particles. If they are absent then it is reasonable to conclude that it is due to the temporal and spatial inhomogeneities.

6.4 Summary and Conclusions

A balance between nonlinear steepening and dispersion controls the scale length of the magnetic field transition at the shock which in turn determines the nature of the ion heating. At very low Mach numbers the dispersive scale length is very long and determines the thickness of the magnetic field and plasma jumps at the shock. As the Mach number increases the dispersive scale length becomes shorter and the upstream waves begin to interact more strongly with the plasma as their wavelength approaches the streaming gyro-radius on the upstream side. The interaction of the incoming ions with these waves results

in a large entropy increase and some amount of heating in the upstream region. From Heos 1 and Ogo 5 observations of a quasi-parallel bow shock Greenstadt *et al.* (1977) pointed out that the ions experienced some thermalization in the region upstream of the shock transition. Thomsen *et al.* (1985) also reported a similar phenomenon in more oblique shocks.

These results are not entirely inconsistent with the existing theories. The waves that are considered by Quest (1988) have very long wavelengths and are not expected to interact very strongly with the plasma. It is noted, however, that the conditions at the shock favor generation of these waves through streaming instabilities so it is reasonable to expect that they are still an integral part of the shock structure if not an important part of the dissipation mechanism. The upstream waves discussed by Quest are occasionally (but not consistently) seen in the simulations performed here but are always of very small amplitude. The shorter wavelength waves that are considered here are not mentioned by Quest.

It is seen that while the principal temperature increase (determined by $T_2 - T_1$ rather than T_2/T_1) occurs at the main shock ramp, a considerable amount of heating occurs in the region upstream of the shock ramp. Relating this to the discussion on entropy and the equations of state presented in Appendix B, this shows that the entropy production for the shock occurs mainly in the upstream region. At the principal shock ramp the compression is seen to be much closer to the isentropic-adiabatic rate. This is consistent with the scenario that the particles are scattered and heated by the upstream wavetrain and are then compressed where the magnetic field experiences a permanent increase in magnitude.

In conclusion, we have examined the characteristics of the ion heating based on simulation results of moderate beta ($\beta = 0.5$), quasi-parallel ($\theta_{Bn} = 10°$), collisionless shocks for Mach numbers ranging from $M_A = 1.2$ to 8.0. The heating is seen to occur in two distinct stages with most of the entropy production for the shock being accomplished in

the first stage which can be characterized by a polytropic equation of state whose exponent is much greater than the isentropic-adiabatic value. The compression at the main shock jump is generally seen to be between adiabatic and isothermal. The nature of the heating is consistent with the hypothesis that the heating is due to finite larmor radius effects and the dispersive character of the fast mode shock as the particles encounter the upstream wavetrain and magnetic ramp.

Chapter 7. Discussion and Conclusions

The objective of this thesis is to resolve some of the unanswered questions concerning the quasi-parallel collisionless shock wave. In conducting this study a simulation model is used and it should be kept in mind that the results from the simulation model are limited by the constraints imposed upon it. In brief, the simulation assumes a one-dimensional geometry, the electrons are inertialess, and high frequency ($\omega \gtrsim \omega_{pe}, \Omega_e$) radiation is neglected.

It has been demonstrated that the simulation model can reproduce reasonably well the same structures that are observed by satellites in the interplanetary medium. This is done explicitly for the magnetic field profiles of three specific cases in Chapter 3. It is also seen from the results of Chapters 5 and 6 that the qualitative character as obtained from the observations is also seen in the simulation model. The discrepancies between the observed and simulated results may be explained by the assumptions made concerning the geometry of the shock and the simulation model. It appears that the wave normal for the precursor waves may by aligned with the upstream magnetic field rather than with the shock normal as is usually assumed.

The effects of using three different electron equations of state and their relationship to the electrostatic potential jump are considered in Chapter 4. It is found that the expected potential jump due to the CGL equation is unphysical in that it has negative values which would accelerate ions through the shock. From the simulation results the effects of the three equations are very similar for low Mach number. At higher Mach numbers ($M_A \gtrsim 3$) only the isotropic power law equation of state behaves reasonable in the simulation. Due to their implicit anisotropies the CGL and CCGL equations generate large electric fields which

destroy the shock structure. The values of potential jump obtained from the simulations follow the expected values quite well.

The wavelengths of the upstream and downstream waves as well as the scale lengths of the jumps in the magnetic field magnitude, the density, and the normal flow velocity were examined as a function of the Alfvén Mach number for shocks with $\theta_{Bn} = 10°$ and $\beta = 0.5$. The wavelength of the upstream waves follows that predicted for a phase standing whistler very well but are around a factor of 2 to large. This may be explained by the reduction in the flow near the shock and/or nonlinear effects. The wavelength of the downstream waves which appear for $M_A \gtrsim 2.5$ are 2-3 times the streaming gyro-radius and appear to be otherwise independent of the Mach number. The scale length of the magnetic field jump is on the order of the upstream wavelength. The scale length of the plasma jump is about $10\rho_s$ at low Mach numbers and around $1 - 2\rho_s$ at higher Mach numbers. Particularly near the transition Mach number ($M_A \approx 2.5$) where its width can be the largest, the plasma jump length tends to vary with time. This temporal behavior is an oscillation in the shock thickness as it steepens to near the dispersive scale length and then relaxes to scales many times larger before steepening again.

The characteristics of the ion heating were studied in Chapter 6. It was found that the ion heating occurs in two distinct stages, each of which can be described by a power law coefficient. The heating that occurs in the upstream part of the transition region is associated with the upstream whistler wave train. The heating here is much greater than the isentropic-adiabatic rate of $\gamma = 5/3$. The second stage of heating is associated with the principal density jump and is characterized by an exponent that lies within the range $1 \lesssim \gamma_2 \lesssim 2$. It is seen that while the largest temperature increase may be at the main shock ramp, most of the entropy production for the shock occurs in the upstream region. It is suggested that the temperature increase may be accounted for by the magnetic field structures and finite larmor radius effects and one need not invoke wave instabilities

to provide the dissipation. However, it appears that waves associated with instabilities play some role in the shock structure since this seems to be the most likely generation mechanism for the downstream waves.

The quasi-parallel collisionless shock wave exhibits a large variety of complex structures. This has led to their neglect in the study of collisionless shock waves from observations because of the difficulty in identifying the shock transition. From a simulationists point of view, the large spatial scales and long time scales that appear to be an integral part of the shock have also made their study difficult. Theoreticians tend to confine their studies to extreme cases (such as very low or very high Mach numbers, $\beta >> 1$ or $\beta << 1$) that are usually not observed in the solar wind. It is hoped that this study has added to the knowledge of the quasi-parallel collisionless shock wave.

References

Abe, H., N. Sakairi, R. Itatani, and H. Ocuda, High-order spline interpolations in the particle simulation, *J. of Comp. Phys.*, **63**, 247, 1986.

Anderson, J. E., *Magnetohydrodynamic Shock Waves*, M. I. T., Cambridge, Mass., 1963.

Anderson, K. A., R. P. Lin, D. W. Potter, and H. D. Heetderks, An experiment to measure interplanetary and solar electrons, *IEEE Trans. Geoscience Electronics*, GE-16, 153, 1978.

Auer, R. D., and H. J. Volk, Parallel high beta shocks and relaxation phenomena, *Astrophys. Space Sci.*, **72**, 243, 1973.

Axford, W. I., The interaction between the solar wind and the earth's magnetosphere, *J. Geophys. Res.*, **67**, 3791, 1962.

Bame, S. J., J. R. Asbridge, H. E. Felthauser, J. P. Gore, H. L. Hawk, and J. Chavez, ISEE-C solar wind plasma experiment, *IEEE Trans. Geoscience Electronics*, GE-16, 160, 1978a.

Bame, S. J., J. R. Asbridge, H. E. Felthauser, J. P. Gore, G. Paschmann, P. Hemmerich, K. Lehmann, and H. Rosenbauer, ISEE-1 and ISEE-2 fast plasma experiment and the ISEE-1 solar wind experiment, *IEEE Trans. Geoscience Electronics*, GE-16, 216, 1978b.

Bavassano-Cattaneo, M. B., B. T. Tsurutani, and E. J. Smith, Subcritical and supercritical interplanetary shocks: Magnetic field and energetic particle observations, *J. Geophys. Res.*, **91**, 11,929, 1986.

Berezin, Y. A., and R. Z. Sagdeev, One-dimensional nonlinear instability model for an anisotropic plasma, *Soviet Phys. Doklady*, **14**, 62,1969.

Biskamp, D., and H. Welter, Ion heating in high-Mach number oblique, collisionless shock waves, *Phys. Rev. Lett.*, **28**, 410, 1972.

Boyd, T. J. M., and J. J. Sanderson, *Plasma Dynamics*, Nelson pub., London, 1969.

Brillouin, L., Wave Propagation and Group Velocity, *Pure and Applied Physics* monographs, vol. 8, p. 122, Academic Press, New York, 1960.

Chew, G. F., M. L. Goldberger, and F. E. Low, The Boltzmann equation and the one-fluid hydromagnetic equations in the absence of particle collisions, *Proc. Royal Soc.* (London), **236**, 112, 1956.

Coroniti, F. V., Dissipation discontinuities in hydrodynamic shock waves, *J. Plasma Phys.*, **4**, 265, 1970.

de Hoffman, F., and E. Teller, Magneto-hydrodynamic shocks, *Phys. Rev.*, **80**, 692, 1950.

Edmiston, J. P., and C. F. Kennel, A parametric study of slow shock Rankine-Hugoniot solutions and critical Mach numbers, *J. Geophys. Res.*, **91**, 1361, 1986.

Feldman, W. C., S. J. Swartz, S. J. Bame, D. N. Baker, J. Birn, J. T. Gosling, E. W. Hones, D. J. McComas, J. A. Slavin, E. J. Smith, and R. D. Zwickl, Evidence for slow mode shocks in the deep magnetic tail, *Geophys. Res. Lett.*, **11**, 599, 1984a.

Feldman, W. C., D. N. Baker, S. J. Bame, J. Birn, E. W. Hones, Jr., S. J. Schwartz, and R. L. Tokar, Power dissipation at slow-mode shocks in the distant geomagnetic tail, *Geophys. Res. Lett.*, **11**, 1058, 1984b.

Frank, L. A., D. M. Yeager, H. D. Owens, K. L. Ackerson, and M. R. English, Quadrispherical LEPEDEAS for ISEE's-1 and -2 plasma measurements, *IEEE Trans. Geosci. Electronics*, GE-16, 221, 1978.

Formisano, V., The physics of the Earth's collisionless shock wave, *J. de Physique*, **38**, C6, 1977.

Forslund, D. W., and J. P. Freidberg, Theory of laminar collisionless shocks, *Phys. Rev. Lett.*, **27**, 1189, 1971.

Forslund, D. W., J. M. Kindel, and E. L. Lindman, Parametric excitation of electromagnetic waves, *Phys. Rev. Lett.*, **29**, 249, 1972.

Forslund, D. W., J. M. Kindel, and E. L. Lindman, Simulation of quasi-parallel bow shock structures, paper presented at the 1980 Spring Meeting, AGU, Toronto, Canada, 1980.

Freeman, J. W., The morphology of the electron distribution in the outer radiation zone near the magnetospheric boundary as observed by Explorer 12, *J. Geophys. Res.*, **69**, 1691, 1964.

Galeev, A. A., and R. Z. Sagdeev, Model of a shock wave in solar wind plasma, *Soviet Phys. JETP*, Engl. Transl., **30**, 571, 1970.

Greenstadt, E. W., C. T. Russell, V. Formisano, P. C. Hedgecock, F. L. Scarf, M. Neugebauer, and R. E. Holzer, Structure of a quasi-parallel, quasi-laminar bow shock, *J. Geophys. Res.*, **82**, 651, 1977.

Greenstadt, E. W., and R. W. Fredricks, Shock systems in collisionless plasmas, in *Solar System Plasma Physics*, Vol. III edited by L. J. Lanzerotti, C. F. Kennel, and E. N. Parker, North-Holland pub., Amsterdam, 1979.

Greenstadt, E. W., V. Formisano, C. Goodrich, J. T. Gosling, M. Lee, M. Leroy, M. Mellott, K. Quest, A. E. Robson, P. Rodriguez, J. Scudder, J. Slavin, M. Thomsen, D. Winske, and C. S. Wu, Collisionless shock waves in the solar terrestrial environment, in *Solar Terrestrial Physics; Present and Future*, NASA reference pub. 1120, 1984.

Greenstadt, E. W., Oblique, parallel, and quasi-parallel morphology of collisionless shocks, in *Collisionless Shocks in the Heliosphere: Reviews of Current Research, Geophys. Monogr. Ser.*, vol. **35**, edited by B. T. Tsurutani and R. B. Stone, pp. 169–184, AGU, Washington, D.C., 1985.

Hada, T., and C. F. Kennel, Nonlinear evolution of slow waves in the solar wind, *J. Geophys. Res.*, **90**, 531, 1985.

Hada, T., C. F. Kennel, and T. Terasawa, The effect of pressure anisotropy on the slow mode shocks, paper presented at the *Chapman Conference on Magnetotail Physics*, 1986.

Jackson, R. W., Second order effects related to a model for a parallel shock, *J. Geophys. Res.*, **88**, 9981, 1983.

Kan, J. R., and D. W. Swift, Structure of the quasi-parallel bow shock: Results of numerical simulations, *J. Geophys. Res.*, **88**, 6919, 1983.

Kantrowitz, A., and H. E. Petschek, MHD characteristics and shock waves, in *Plasma Physics in Theory and Application*, edited by W.B. Kunkel, McGraw-Hill, New York, 1966.

Kellog, P. J., Flow of plasma around the earth, *J. Geophys. Res.*, **67**, 3805, 1962.

Kennel, C. F., and R. Z. Sagdeev, Collisionless shock waves in high beta plasmas, *J. Geophys. Res.*, **72**, 3303, 1967.

Kennel, C. F., and H. E. Petschek, Magnetic turbulence in shocks, in *Physics of the Magnetosphere*, edited by R. Carovillano, J. F. McClay, and H. R. Radoski, p. 485. D. Reidel, Hingham, Mass., 1968.

Kennel, C. F., F. L. Scarf, F. V. Coroniti, E. J. Smith, and D. A. Gurnett, Nonlocal plasma turbulence associated with interplanetary shocks, *J. Geophys. Res.*, **87**, 17, 1982.

Kennel, C. F., F. L. Scarf, F. V. Coroniti, C. T. Russell, K. P. Wenzel, T. R. Sanderson, P. Van Nes, W. C. Feldman, G. K. Parks, E. J. Smith, B. T. Tsurutani, F. S. Mozer, M. Temerin, R. R. Anderson, J. D. Scudder, and M. Scholer, Plasma and energetic particle structure upstream of a quasi-parallel interplanetary shock, *J. Geophys. Res.*, **89**, 5419, 1984a.

Kennel, C. F., J. P. Edmiston, F. L. Scarf, F. V. Coroniti, C. T. Russell, E. J. Smith, B. T. Tsurutani, J. D. Scudder, W. C. Feldman, R. R. Anderson, F. S. Mozer, and M. Temerin, Structure of the November 12, 1978, quasi-parallel interplanetary shock, *J. Geophys. Res.*, **89**, 5436, 1984b.

Kennel, C. F., J. P. Edmiston, and T. Hada, A quarter century of collisionless shock research, in *Collisionless Shocks in the Heliosphere: A tutorial Review*, R. G. Stone and B. T. Tsurutani eds., American Geophysical Union, Washington, D.C., 1985.

Landau, L. D., and E. M. Lifshitz, *Course on Theoretical Physics Vol. 5, Statistical Physics*, Pergamon Press Ltd., London, 1958.

Landau, L. D., and E. M. Lifshitz, *Course of Theoretical Physics Vol. 8, Electrodynamics of Continuous Media*, Pergamon Press Ltd., London, 1960.

Lee, L. C., C. S. Wu, and X. W. Hu, Increase of ion kinetic temperature across a collisionless shock: I. A new mechanism, *Geophys. Res. Lett.*, **13**, 209, 1986.

Lee, M. A., Coupled hydromagnetic wave excitation and ion acceleration at interplanetary travelling shocks, *J. Geophys. Res.*, **88**, 6109, 1983.

Mandt, M. E., J. R. Kan, and C. T. Russell, Comparison of magnetic field structures in quasi-parallel interplanetary shocks: observations versus simulations, *J. Geophys. Res.*, **91**, 8981, 1986.

Moiseev, S. S., and R. Z. Sagdeev, Collisionless shock waves in a plasma in a weak magnetic field, in *Plasma Physics J. of Nucl. Energy*, Part C, **5**, 43, 1963.

Ness N. F., C. S. Scearce, and J. B. Seek, Initial results of the IMP 1 magnetic field experiment, *J. Geophys. Res.*, **69**, 3531, 1964.

Nicholson, D. R., *Introduction to Plasma Theory*, John Wiley and Sons pub., New York, 1983.

Olson, J. V., Electromagnetic Radiation in the Earth's Bow Shock, Ph.D. Thesis dissertation, University of California, Los Angeles, 1970.

Parker, E. N., A quasi-linear model of plasma shock structure in a longitudinal magnetic field, *J. Nucl. Energy*, **C2**, 146, 1961.

Petschek, H. E., Magnetic field annihilation, in *AAS-NASA Symposium on the Physics of Solar Flares*, p. 425, edited by W. N. Hess, NASA, Washington, D.C. 1964.

Priest, E. R., *Solar Magnetohydrodynamics*, D. Reidel Pub. Co., Dordrecht Holland, 1982.

Quest, K. B., D. W. Forslund, J. U. Brackbill, and K. Lee, Collisionless dissipation processes in quasi-parallel shocks, *Geophys. Res. Lett.*, **10**, 471, 1983.

Quest, K. B., Simulation of quasi-parallel collisionless shocks, in *Collisionless Shocks in the Heliosphere: Reviews of Current Research, Geophys. Monogr. Ser.*, vol. **35**, edited by B. T. Tsurutani and R. G. Stone, pp. 185–194, American Geophysical Union, Washington, D.C., 1985.

Quest, K. B., Theory and simulation of collisionless parallel shocks, accepted *J. Geophys. Res.*, June 1988.

Roache, P. J., *Computational Fluid Dynamics*, p. 42, Hermosa Publishers, Albuquerque, New Mexico, 1972.

Russell, C. T. The ISEE-1 and -2 fluxgate magnetometers, *IEEE Trans. Geosci. Electronics*, GE-16, 239, 1978.

Russell, C. T., M. M. Mellott, E. J. Smith, and J. H. King, Multiple spacecraft observations of interplanetary shocks: Four spacecraft determination of shock normals, *J. Geophys. Res.*, **88**, 4739, 1983a.

Russell, C. T., E. J. Smith, B. T. Tsurutani, J. T. Gosling, and S. J. Bame, Multiple spacecraft observations of interplanetary shocks: Characteristics of the upstream ULF turbulence, in *Solar Wind Five*, NASA Conference Publication 2280, 385, NASA Washington, D.C., 1983b.

Russell, C. T., J. T. Gosling, R. D. Zwickl, and E. J. Smith, Multiple spacecraft observations of interplanetary shocks: ISEE three-dimensional plasma measurements, *J. Geophys. Res.*, **88**, 9941, 1983c.

Russell, C. T., and M. M. Hoppe, Upstream waves and particles, *Space Sci. Rev.*, **34**, 155, 1983.

Russell, C. T., and C. J. Alexander, Multiple spacecraft observations of interplanetary shocks: Shock-normal oscillations and their effects, *Adv. Space Res.*, **4(2-3)**, 277, 1984.

Sagdeev, R. Z., The 1976 Oppenheimer lectures: Critical problems in plasma astrophysics, II, Singular layers and reconnection, *Rev. Mod. Phys.*, **51**, 11, 1979.

Scholer, M., F. M. Ipavich, G. Gloeckler, and D. Hovestadt, Acceleration of low-energy protons and alpha particles at interplanetary shock waves, *J. Geophys. Res.*, **88**, 1977, 1983.

Scudder, J. D., L. F. Burlaga, and E. W. Greenstadt, Scale lengths in quasi-parallel shocks, *J. Geophys. Res.*, **89**, 7545, 1984.

Scudder, J. D., A. Mangeney, C. Lacombe, C. C. Harvey, T. L. Aggson, R. R. Anderson, J. T. Gosling, G. Paschmann, and C. T. Russell, The resolved layer of a collisionless, high beta, supercritical, quasi-perpendicular shock wave 1. Rankine-Hugoniot geometry, currents, and stationarity, *J. Geophys. Res.*, **91**, 11,019, 1986a.

Scudder, J. D., A. Mangeney, C. Lacombe, C. C. Harvey, and T. L. Aggson, The resolved layer of a collisionless, high beta, supercritical, quasi-perpendicular shock wave 2. Dissipative fluid electrodynamics, *J. Geophys. Res.*, **91**, 11,053, 1986b.

Scudder, J. D., A. Mangeney, C. Lacombe, C. C. Harvey, C. S. Wu, and R. R. Anderson, The resolved layer of a collisionless, high beta, supercritical, quasi-perpendicular shock wave 3. Vlasov electrodynamics, *J. Geophys. Res.*, **91**, 11,075, 1986c.

Sonnet, C. P., and I. J. Abrams, The distant geomagnetic field, 3. Disorder and shocks in the magnetopause, *J. Geophys. Res.*, **68**, 1,233, 1963.

Swift, D. W., and L. C. Lee, Rotational discontinuities and the structure of the magnetopause, *J. Geophys. Res.*, **88**, 111, 1983a.

Swift, D. W., On the structure of the magnetic slow switch-off shock, *J. Geophys. Res.*, **88**, 5685, 1983b.

Tidman, D.A., and N. A. Krall, *Shock Waves in Collisionless Plasmas*, Wiley-Interscience pub., New York, 1971.

Thomsen, M. F., J. T. Gosling, S. J. Bame, and M. M. Mellott, Ion and electron heating at collisionless shocks near the critical Mach number, *J. Geophys. Res.*, **90**, 137, 1985.

Tsurutani, B. T., E. J. Smith, and D. E. Jones, Waves observed upstream of interplanetary shocks, *J. Geophys. Res.*, **88**, 5645, 1983.

Winske, D., Elmer K. Stover, and S. Peter Gary, The structure and evolution of slow mode shocks, *Geophys. Res. Lett.*, **12**, 295, 1985.

Wolfson, R., The configuration of slow-mode shocks, *J. Geophys. Res.*, **92**, 9875, 1987.

Zhigulev, V. N., On the phenomena of magnetic detachment of the flow of a conduction medium, *Soviet Phys. Doklady*, 4, 514, 1959.

Appendix A The Simulation Code

This appendix contains a description of the simulation code that was used in this study. It is adapted from the code originally developed by D. W. Swift. First the basic equations that are used in the simulation are formulated in a system of dimensionless units. This provides the normalization for the simulation. Then this dimensionless set of equations is used to derive the equations that are to be implemented in the simulation. The finite differencing schemes utilized and the implementation of the equations are presented next. Finally, a number of aspects and considerations for actually running the simulation are discussed.

A.1 Normalization of Equations

When performing a simulation it is desirable to formulate the set of equations in a system of dimensionless units. With such a system, any given simulation run actually represents an entire class of events rather than any one particular event. Presented here are the ion equations of motion, the canonical momentum equation, Ampere's law (in differential form), Faraday's law, and the electron equation of motion. All quantities are normalized to the basic units of time, mass, length, and magnetic field strength.

We will begin with the ion equations of motion. The equations of motion for a charged particle in arbitrary electric and magnetic fields are

$$\frac{d\vec{x}}{dt} = \vec{v} \tag{A1.1}$$

$$\frac{d\vec{v}}{dt} = \frac{e}{M}\vec{E} + \frac{e}{Mc}\vec{v} \times \vec{B} \tag{A1.2}$$

where $\vec{x}$ is the position vector, $\vec{v}$ is the velocity vector, e is the electron charge, M is the ion mass, c is the speed of light, and $\vec{E}$ and $\vec{B}$ are the electric and magnetic fields. (A1.1) and (A2.1) are used to integrate the particle position and the z-component of the velocity.

We define the following quantities as our dimensionless variables: $\vec{x}' = \vec{x}/\lambda$, $t = t'/\tau$, $\vec{v}' = \vec{v}/\nu$, $\vec{\varepsilon}' = \vec{E}/\xi$, and $\vec{\Omega} = \vec{B}/B_0$. Substituting in our dimensionless variables, we get for (A1.1)

$$\frac{\lambda}{\tau}\frac{d\vec{x}'}{dt'} = \nu\vec{v}' \qquad \text{(A1.1')}.$$

We desire an equation of the form

$$\frac{d\vec{x}'}{dt'} = \vec{v}' \qquad \text{(A1.3)}$$

so we must have $\nu = \lambda/\tau$. For (A1.2) we get

$$\frac{d\vec{v}'}{dt'} = \frac{e\tau^2\xi}{M\lambda}\vec{\varepsilon}' + \frac{e\tau B_0}{Mc}\vec{v}' \times \vec{\Omega} \qquad \text{(A1.2')}.$$

Again we seek an equation of the form

$$\frac{d\vec{v}'}{dt'} = \vec{\varepsilon}' + \vec{v}' \times \vec{\Omega} \qquad \text{(A1.4)}$$

so we must set $\tau = Mc/eB_0$ and $\xi = M\lambda/e\tau^2$. Thus we see that the time scale will be in units of the inverse ion gyro-frequency based on the normalization field B_0.

The canonical momentum $\vec{p}_i$ is used to integrate the transverse velocities in time. This is done to eliminate the dependence of the force on $\frac{\partial \vec{A}}{\partial t}$ (through the electric field, see (A2.13)) which leads to numerical instabilities. The equations are

$$\vec{p}_{it} = M\vec{v}_t + \frac{e}{c}\vec{A}_t \qquad \text{(A1.5)}$$

and

$$\frac{d\vec{p}_{it}}{dt} = \frac{e}{c}\vec{v}_t \times \hat{z}B_z \qquad \text{(A1.6)}.$$

For these equations we require the vector potential $\vec{A}_t$. We define a vector potential by $\vec{\Omega}_t = \vec{\nabla}' \times \vec{a}_t$ and upon comparing this to the usual definition $\vec{B} = \vec{\nabla} \times \vec{A}$, we see that $\vec{A}_t = \lambda B_0 \vec{a}_t$. Now letting $\vec{p}_{it} = \eta \vec{p}'_{it}$ and recalling the definition of τ, (A1.5) becomes

$$\frac{\eta c}{\lambda e B_0} \vec{p}'_{it} = \vec{v}'_t + \vec{a}_t \qquad \text{(A1.5')}.$$

So we set $\eta = \lambda e B_0 / c$ and (A1.5) and (A1.6), respectively, become

$$\vec{p}'_{it} = \vec{v}'_t + \vec{a}_t \qquad \text{(A1.7)}$$

and

$$\frac{d\vec{p}'_{it}}{dt'} = \vec{v}'_t \times \hat{z}\Omega_z \qquad \text{(A1.8)}.$$

Let us now consider Ampere's law (neglecting the displacement current)

$$\vec{\nabla} \times \vec{B} = \frac{4\pi}{c} \vec{J} = \frac{4\pi e}{c} (n_i \vec{u}_i - n_e \vec{u}_e) \qquad \text{(A1.9)}$$

where n_j and $\vec{u}_j$ are the density and flow velocity of the j-th species. The displacement current is omitted since we are interested in low frequency ($\omega \approx \Omega_i \ll \Omega_e, \omega_{pe}$) waves in our simulation. If we define a dimensionless density by $N = n\lambda A$, where A is an area to be determined, then (A1.9) becomes

$$\vec{\nabla}' \times \vec{\Omega} = \alpha (N_i \vec{u}'_i - N_e \vec{u}'_e) \qquad \text{(A1.10)}$$

where $\alpha = \sigma\lambda/A$ and $\sigma = 4\pi e^2/Mc^2$. The value of α is adjusted to minimize computational time while retaining phenomena of interest.

By eliminating the magnetic field in favor of the vector potential, Faraday's law is

$$\vec{\nabla} \times \vec{E} = -\frac{1}{c} \frac{\partial}{\partial t} \left(\vec{\nabla} \times \vec{A} \right) \qquad \text{(A1.11)}.$$

From this we see that the inductive electric field may be expressed as

$$\vec{E} = -\frac{1}{c} \frac{\partial \vec{A}}{\partial t} \qquad \text{(A1.12)}.$$

In simulation units, the transverse field becomes

$$\vec{\varepsilon}_t = -\frac{\partial \vec{a}_t}{\partial t'} \qquad \text{(A1.13).}$$

Note that in a one dimensional simulation the transverse electric field can have no electrostatic component unless it is externally imposed (all quantities are functions of the simulation coordinate, z, only) and the z component of the electric field must be electrostatic.

The equation of motion for the electrons as a fluid is

$$-m\frac{d\vec{u}_e}{dt} = e\vec{E} + \frac{e}{c}\vec{u}_e \times \vec{B} + \frac{1}{n_e}\vec{\nabla}\cdot\mathbf{P}_e \qquad \text{(A1.14)}$$

where $\mathbf{P}_e$ is the electron pressure tensor and m is the electron mass. Defining the dimensionless pressure tensor by $\mathbf{P}_e = \Theta\mathbf{P}'_e$ and dividing by the ion mass M, (A1.14) becomes

$$\frac{-m}{M}\frac{d\vec{u}'_e}{dt'} = \vec{\varepsilon}' + \vec{u}'_e \times \vec{\Omega} + \frac{\Theta A\tau^2}{M\lambda N_e}\vec{\nabla}'\cdot\mathbf{P}'_e \qquad \text{(A1.14')}$$

so if we let $r = m/M$ and $\Theta = \lambda M/A\tau^2 = \alpha M/\sigma\tau^2$ we get

$$-r\frac{d\vec{u}'_e}{dt'} = \vec{\varepsilon}' + \vec{u}'_e \times \vec{\Omega} + \frac{1}{N_e}\vec{\nabla}'\cdot\mathbf{P}'_e \qquad \text{(A1.15).}$$

In this simulation the electrons are treated as inertialess so we will set $r = 0$. Note that the ion mass M is taken to be the normalized mass unit in (A1.15).

It has been shown that, in the simulation, the basic mass unit is the ion mass. We choose the component of the magnetic field parallel to the shock normal, B_n to normalize the field. With this the time scale, $\tau = \Omega_{ni}^{-1} = \frac{eB_n}{Mc}$, is the inverse ion gyro-frequency based on the normal field component. To determine the scaling length, λ, note that

$$N\alpha = (n\lambda A)\left(\frac{\sigma\lambda}{A}\right) = n\sigma\lambda^2 \qquad \text{(A1.16)}$$

thus we get

$$\lambda = \sqrt{N\alpha/n\sigma} \qquad \text{(A1.17)}.$$

The quantity $1/\sqrt{n\sigma}$ is the ion inertial length c/ω_{pi} where ω_{pi} is the ion plasma frequency.

As an example of how the simulation is scaled, consider the first of the interplanetary shock cases discussed in Chapter 3. For this case $N = 25$, $\alpha = 5.272(10^{-3})$, $n = 4\text{cm}^{-3}$, and $B_1 = 7.8\gamma$. With these values for the simulation parameters and the observed upstream density and average magnetic field strength the grid spacing is

$$\Delta x = \sqrt{N\alpha}(c/\omega_{pi}) = 2.28(10^7)\sqrt{N\alpha/n}\text{ cm} = 41.3\text{km} \qquad \text{(A1.18)}$$

and the total system length is 24,400km. If B is in units of γ then the time scale is

$$\tau = T_i/2\pi = 10.5/B\text{ sec} = 1.34\text{sec} \qquad \text{(A1.19)}$$

and the total duration is 188 seconds for this case.

A.2 Derivation of Equations

A derivation of the equations used in the simulation is presented following that of Swift and Lee (1983) but including the anisotropic electron pressure. To be derived are the z component of the electric field, the field equation for the vector potential, and the ion equation of motion. The equations presented in this section are in the dimensionless simulation units.

The electrons are treated as a massless fluid of finite pressure, therefore their equation of motion is

$$\vec{\varepsilon} + \vec{u}_e \times \vec{\Omega} + \frac{1}{n}\vec{\nabla}\cdot\mathbf{P}_e = 0 \qquad \text{(A2.1)}.$$

In the presence of a magnetic field in an arbitrary coordinate system, the electron pressure tensor may be written as

$$\mathbf{P}_e = P_{e\perp}\mathbf{I} + \left(P_{e\|} - P_{e\perp}\right)\frac{\vec{\Omega}\vec{\Omega}}{\Omega^2} \tag{A2.2}$$

where $P_{e\perp}$ and $P_{e\|}$ are the scalar electron pressures perpendicular and parallel to the magnetic field and $\mathbf{I}$ is the unit diadic.

The simulation is one-dimensional along the z-axis. This means that all derivatives with respect to the x and y coordinates are zero. So the electrostatic part of the field $\vec{\varepsilon}_{es} = -\vec{\nabla}\phi$ has only a z component and from Faraday's law the transverse fields may be expressed as (A1.13)

$$\vec{\varepsilon}_t = -\frac{\partial \vec{a}_t}{\partial t} \tag{A2.3}.$$

(A1.1) can thus be written in component form as

$$\varepsilon_x + u_{ey}\Omega_z - u_{ez}\Omega_y + \frac{1}{n}\frac{\partial}{\partial z}\left[\left(P_{e\|} - P_{e\perp}\right)b_x b_z\right] = 0 \tag{A2.4}$$

$$\varepsilon_y + u_{ez}\Omega_x - u_{ex}\Omega_z + \frac{1}{n}\frac{\partial}{\partial z}\left[\left(P_{e\|} - P_{e\perp}\right)b_y b_z\right] = 0 \tag{A2.5}$$

$$\varepsilon_z + u_{ex}\Omega_y - u_{ey}\Omega_x + \frac{1}{n}\frac{\partial}{\partial z}\left[\left(P_{e\|} - P_{e\perp}\right)b_z b_z\right] = 0 \tag{A2.6}$$

where $\vec{b} = (b_x, b_y, b_z) = \vec{B}/B$ is the magnetic field unit vector. By solving (A2.4) and (A2.5) for u_{ex} and u_{ey} respectively, and using (A2.3) to eliminate $\vec{\varepsilon}_t = (\varepsilon_x, \varepsilon_y, 0)$ in (A2.6) one obtains for the z component of the electric field

$$\varepsilon_z = \frac{\vec{\Omega}_t}{\Omega_z}\cdot\frac{\partial \vec{a}_t}{\partial t} - \frac{1}{n}\frac{\partial P_{e\|}}{\partial z} + \frac{\left(P_{e\|} - P_{e\perp}\right)}{n\Omega^2}\left(\vec{\Omega}_t \cdot \frac{\partial \vec{\Omega}_t}{\partial z}\right) \tag{A2.7}.$$

With the definition of the vector potential, $\vec{\Omega}_t = \vec{\nabla} \times \vec{a}_t$, the field equation (A1.10) becomes

$$\frac{\partial^2 \vec{a}_t}{\partial z^2} = -\alpha\left(n\vec{u}_{it} - n\vec{u}_{et}\right) \tag{A2.8}$$

where we have assumed quasi-neutrality, i.e. $n_i = n_e = n$. From the ion canonical momentum we calculate the canonical momentum density as

$$\vec{\pi}_t = \sum_k S(z - z_k)\vec{p}_{kt} = n\left(\vec{u}_{it} + \vec{a}_t\right) \tag{A2.9}$$

where $S(z - z_k)$ is the particle position to grid-point weighting function (see section A.3). Using (A2.9) to eliminate $\vec{u}_{it}$ (A2.8) becomes

$$\frac{\partial^2 \vec{a}_t}{\partial z^2} = -\alpha\left(\vec{\pi}_t - n\vec{a}_{it} - n\vec{u}_{et}\right) \tag{A2.10}.$$

Now we make use of (A2.4) and (A2.5) to eliminate u_{ex} and u_{ey}. The result, in component form, is

$$\frac{\partial^2 a_x}{\partial z^2} = -\alpha\pi_x + \alpha n a_x - \frac{\alpha n}{\Omega_z}\left(\frac{\partial a_x}{\partial t} + u_z\frac{\partial a_y}{\partial z} - \frac{1}{n}\frac{\partial P_{yz}}{\partial z}\right) \tag{A2.11a}$$

$$\frac{\partial^2 a_y}{\partial z^2} = -\alpha\pi_y + \alpha n a_y - \frac{\alpha n}{\Omega_z}\left(\frac{\partial a_y}{\partial t} + u_z\frac{\partial a_x}{\partial z} - \frac{1}{n}\frac{\partial P_{xz}}{\partial z}\right) \tag{A2.11b}$$

or

$$\frac{\partial^2 \vec{a}_t}{\partial z^2} = \alpha\left(n\vec{a}_t - \vec{\pi}_t\right) - \frac{\alpha n}{\Omega_z}\hat{z}\times\left(\frac{\partial \vec{a}_t}{\partial t} + u_z\frac{\partial \vec{a}_t}{\partial z} - \frac{1}{n}\frac{\partial \vec{P}_{tz}}{\partial z}\right) \tag{A2.12}$$

where $\vec{P}_{tz} = (P_{xz}, P_{yz}, 0)$ are the x-z and y-z components of the electron pressure tensor.

The ion equation of motion is

$$\frac{dv_z}{dt} = \hat{z}\cdot\left(\vec{v}_t\times\vec{\Omega}_t\right) + \varepsilon_z \tag{A2.13}.$$

In order to use (A2.7) in (A2.13) we need to eliminate the term involving the time derivative of $\vec{a}_t$. To do this we take $\vec{\Omega}_t\cdot[\hat{z}\times$ (A2.12)], which after numerous manipulations yields

$$\frac{1}{\Omega_z}\vec{\Omega}_t\cdot\frac{\partial \vec{a}_t}{\partial t} = \hat{z}\cdot\left[\left(\vec{a}_t - \frac{\vec{\pi}}{n}\right)\times\vec{\Omega}_t\right] - \frac{1}{2\alpha n}\frac{\partial\Omega_t^2}{\partial z} + \frac{1}{n\Omega_z}\vec{\Omega}_t\cdot\frac{\partial \vec{P}_{tz}}{\partial z} \tag{A2.14}.$$

Now we use (A2.7) and (A2.14) in (A2.13) and eliminate $\vec{v}_t$ with equation (A1.7) to get

$$\frac{dv_z}{dt} = \hat{z}\cdot\left[\left(\vec{p}_{it} - \frac{\vec{\pi}}{n}\right)\times\vec{\Omega}_t\right] + \frac{1}{2n}\left(\frac{P_{e\|} - P_{e\perp}}{\Omega^2} - \frac{1}{\alpha}\right)\frac{\partial\Omega_t^2}{\partial z} - \frac{1}{n}\frac{\partial P_{e\|}}{\partial z} + \frac{\vec{\Omega}_t}{n\Omega_z}\cdot\frac{\partial\vec{P}_{tz}}{\partial z} \qquad \text{(A2.15)}.$$

A.3 Implementation of Equations

Performing the simulation consists primarily of integrating equations (A2.12), (A2.15), and (A1.8) in time. The computations can be formally simplified by writing the two transverse components as the real and imaginary part of a complex number. We introduce the following definitions:

$$\vec{a}_t \quad \Rightarrow \quad a_t = a_x + ia_y \qquad \text{(A3.1a)}$$

$$\vec{\Omega}_t \quad \Rightarrow \quad \Omega_t = \Omega_y - i\Omega_x \qquad \text{(A3.1b)}$$

$$\vec{\pi}_t \quad \Rightarrow \quad \pi_t = \pi_x + i\pi_y \qquad \text{(A3.1c)}$$

$$\vec{p}_{it} \quad \Rightarrow \quad p_{it} = p_{xi} + ip_{yi} \qquad \text{(A3.1d)}$$

$$\vec{P}_{tz} \quad \Rightarrow \quad P_{tz} = P_{zx} + iP_{yz} \qquad \text{(A3.1e)}.$$

With these definitions we see that $\hat{z}\times\vec{a}_t \Rightarrow ia_t$ and $\Omega_t = \frac{\partial a_t}{\partial z}$. So the field equation (A2.9) becomes

$$\frac{\partial^2 a_t}{\partial z^2} = \alpha\left(na_t - \pi_t\right) + \frac{i\alpha n}{\Omega_z}\left(\frac{\partial a_t}{\partial t} + u_z\frac{\partial a_t}{\partial z} - \frac{1}{n}\frac{\partial P_{tz}}{\partial z}\right) \qquad \text{(A3.2)}.$$

The equation for the z component of the ion velocity, (A2.15), can be written as

$$\frac{dv_z}{dt} = \left(p_x - \frac{\pi_x}{n}\right)\Omega_y - \left(p_y - \frac{\pi_y}{n}\right)\Omega_x - \frac{1}{n}\frac{\partial P_{e\|}}{\partial z} - \frac{1}{2\alpha n}\frac{\partial\Omega_t^2}{\partial z} + \frac{1}{n}\frac{\partial}{\partial z}\left(\frac{P_{e\|} - P_{e\perp}}{\Omega^2}\Omega_t^2\right) \qquad \text{(A3.3)}.$$

The ions are moved by integrating (A1.3).

Upon using the definition of the canonical momentum to eliminate $\vec{v}_i$ in (A1.8), we get

$$\frac{dp_{it}}{dt} = i\,(a_t - p_{it})\,\Omega_z \qquad \text{(A3.4)}.$$

It we multiply (A3.4) by $e^{i\Omega_z t}$, upon rearranging terms we get

$$\frac{d}{dt}\left(p_{it}e^{i\Omega_z t}\right) = i\Omega_z a_t e^{i\Omega_z t} \qquad \text{(A3.5)}.$$

A leap frog time stepping scheme is used to integrate the above equations in the simulation. This allows one to maintain second order accuracy without increasing the computation time over that of a first order scheme very much. The quantities p_{it}, v_z, u_z, and π_t are calculated at the even time step. The quantities a_t, P_e, and n are calculated at the half time step. The position, z, is advanced every half time step because particle positions are needed at both the full and half time steps to compute the source terms and coefficients for the equations to be integrated.

The time stepping scheme is as follows: Say we begin at the m^{th} time step. First the canonical momentum is advanced. We use p_{it}^m and $a_t^{m+1/2}$ to calculate p_{it}^{m+1} and $p_{it}^{m+1/2}$ which is the average of the old and new values. Now we advance the velocity using v_z^m, $p_{it}^{m+1/2}$, $a_t^{m+1/2}$, $P_e^{m+1/2}$, and $n^{m+1/2}$ to calculate v_z^{m+1}. The particles are moved a half time step at a time. We use $z^{m+1/2}$ and v_z^{m+1} to get z^{m+1} and from this we also calculate n^{m+1}, u_z^{m+1}, and π_t^{m+1}. Now the particles are advanced another half time step to get $z^{m+3/2}$. Finally the fields are advanced by using $a_t^{m+1/2}$, P_e^{m+1}, n^{m+1}, u_z^{m+1}, and π_t^{m+1} to get $a_t^{m+3/2}$. Then the process repeats itself. The electron pressure is calculated at the even time step by calculating a provisional vector potential from the old electron pressure (at the half time step) since it is found from the density and fields via the equations of state (if P_e is anisotropic).

The field equation (A3.2) is implemented using a fully implicit, second order accurate (in time), finite differencing scheme. Using an implicit scheme makes the computation unconditionally stable for any time step or grid size (assuming constant coefficients and source terms in the equation). (A3.2) may be written as follows

$$\frac{i\alpha n}{\Omega_z}\frac{\partial a_t}{\partial t} = L\left[a_t\right] + \alpha\pi_t + \frac{i\alpha}{\Omega_z}\frac{\partial P_{tz}}{\partial z} \tag{A3.6}$$

where the operator L is

$$L = \frac{\partial^2}{\partial z^2} - \alpha n\left(1 + \frac{iu_z}{\Omega_z}\frac{\partial}{\partial z}\right) \tag{A3.7}.$$

The finite difference implementation of (A3.7) is

$$\frac{i\alpha n}{\Omega_z \Delta t}\left(a_t^{m+3/2} - a_t^{m+1/2}\right) = \frac{1}{2}L\left[a_t^{m+3/2} + a_t^{m+1/2}\right] + \alpha\pi_t^{m+1} + \frac{i\alpha}{\Omega_z}\frac{\partial P_{tz}^{m+1}}{\partial z} \tag{A3.8}$$

where Δt is the time step. On a finite grid the derivatives with respect to z become

$$\frac{\partial f}{\partial z} \quad \Rightarrow \quad \frac{1}{2}(f_{j+1} - f_{j-1}) \tag{A3.9a}$$

and

$$\frac{\partial^2 f}{\partial z^2} \quad \Rightarrow \quad f_{j+1} - 2f_j + f_{j-1} \tag{A3.9b}$$

where j is the grid point and we have set the grid spacing, Δz, equal to unity. So the field equation becomes

$$-A_j a_{j+1}^{m+3/2} + B_j^{+} a_j^{m+3/2} - C_j a_{j-1}^{m+3/2} = A_j a_{j+1}^{m+1/2} - B_j^{+} a_j^{m+1/2} + C_j a_{j-1}^{m+1/2}$$
$$+2\alpha\pi_t^{m+1} + \frac{2i\alpha}{\Omega_z}\frac{\partial P_{tz}^{m+1}}{\partial z} \tag{A3.10}$$

where

$$A_j = 1 - \frac{i\alpha n u_z}{2\Omega_z} \tag{A3.11a}$$

$$B_j^{\pm} = 2 + \alpha n\left(1 \pm \frac{2i}{\Omega_z \Delta t}\right) \tag{A3.11b}$$

$$C_j = 1 + \frac{ian u_z}{2\Omega_z} \tag{A3.11c}.$$

This is solved using the Tri-diagonal algorithm. Note that since we specify the value of Ω_t at the boundaries, this fixes $\frac{\partial a_t}{\partial t}$, so we have Neumann boundary conditions.

An explicit scheme is used to advance v_z. So, (A3.3) in finite difference form is

$$v_z^{m+1} = v_z^m + \Delta t \left\{ \left(p_x - \frac{\pi_x}{n} \right) \Omega_y - \left(p_y - \frac{\pi_y}{n} \right) \Omega_x \right.$$

$$\left. - \frac{1}{n} \frac{\partial P_{e\|}}{\partial z} - \frac{1}{2an} \frac{\partial \Omega^2}{\partial z} + \frac{1}{n} \frac{\partial}{\partial z} \left(\frac{P_{e\|} - P_{e\perp}}{\Omega^2} \Omega_t^2 \right) \right\}^{m+1/2} \tag{A3.12}.$$

The canonical momentum equation (A3.5) becomes

$$p_{it}^{m+1} = p_{it}^m e^{-i\Omega_z \Delta t} + i\Delta t a^{m+1/2} \Omega_z e^{i\Omega_z \Delta t/2} \tag{A3.13}.$$

The particle position, z, is advanced a half time step by

$$z^{m+1} = z^{m+1/2} + \frac{\Delta t}{2} v_z^{m+1} \tag{A3.14a}$$

and

$$z^{m+3/2} = z^{m+1} + \frac{\Delta t}{2} v_z^{m+1} \tag{A3.14b}.$$

This is because the density is needed at the half time step to solve equation A3.8 and at the even time step to solve equation A3.12.

The particle in cell scheme is the weighting function used to compute moments for the simulation grid and is given by

$$S(z - z_k) = \delta(z - j_k)(1 - z_k + j_k) + \delta(z - j_k - 1)(z_k - j_k) \tag{A3.15}$$

where z_k is the position of the k^{th} particle, z is the position coordinate, j_k is z_k truncated to an integer and $\delta(\,)$ is the usual Dirac delta function. This is a simple linear interpolation. That is, the particle quantities are weighted to the two nearest grid points according to

how close to them they are. Grid point quantities are weighted to the particle positions in the same manner.

A.4 The Simulation Domain

The system of equations described in the previous sections covers the mathematics and finite differencing scheme that goes into the simulation model. However, there is more to do in order to use these equations in a working model. This section discusses how the boundaries are handled, how the simulation is initialized, and a couple of other tricks used to keep the simulation under control.

Since the shock normal angle is relatively small for all of the simulations run in this thesis the simulations are performed in the de Hoffman-Teller frame (de Hoffman and Teller 1950) where $(\vec{v} \| \vec{B})$. Usually the normal incidence frame is used for quasi-perpendicular shock runs. Since the system of equations is normalized by the normal magnetic field component exactly perpendicular shocks cannot be run. The simulation is also done in the frame such that, according to the Rankine-Hugoniot equations, the shock should be stationary. This allows the simulation to evolve for the longest period of time without interference from the boundaries.

Since the model used for this simulation is non-periodic there are two boundaries at which particles may enter and exit the simulation domain. Buffer zones in which all quantities are assumed to be constant are maintained at each end of the active simulation domain. This prevents the disruption of particle orbits to near the boundaries which would cause spurious currents and perturbations in the magnetic fields. Particle arrays must be large enough so that there are plenty of particles available to inject into the system. Inactive particles are placed in a reservoir and are not moved until they are required to supply particles to be injected at the boundaries. At each timestep particles are placed at

the outer boundaries (away from the active region) of the buffer zone all active particles are moved. Then, each particle is examined to determine whether it is in the active domain, the buffer zone, or inactive in which case it becomes available for re-injection into the system. The buffer zone is at least one grid space wide so that the particles therein can be used in computing moments for the last active grid point. The buffer zone must also be at least a gyro-diameter wide to prevent disruption of the orbits of particles that may be passing in and out of the active domain.

The particular simulation case is defined by the parameters M_A, θ_{Bn}, β, and P_e/P_i. In addition, the time step Δt and the scaling parameter α determine how well resolved the system will be in time and space. With the upstream state specified the Rankine-Hugoniot equations are solved numerically to determine the particle moments and the magnetic field in the downstream side. Initially, the upstream and downstream states are matched with a hyperbolic tangent producing a monotonic ramp of arbitrary width. The particles are initialized using a random number generator to obtain a maxwellian distribution. The simulation is carried out in an inertial frame in which the shock is at rest and the asymptotic flow is parallel to the magnetic field. So, in general, particles will enter at the upstream boundary and exit at the downstream boundary.

At high Mach numbers the magnetic fields in the far upstream region begin to exhibit very short wavelength ($\lambda \approx 2\Delta x$) waves of significant amplitude (but still less than the usual shock associated wave amplitudes). Also perturbations in the form of density depletions form in this region and are then convected downstream with the flow. Runs were made in which a third order weighting scheme (*e. g.* Abe *et al.*, 1986) was used to compute particle moments. This in effect constitutes a smoothing of the source terms for the field equation and should diminish the problem if it was due to a feedback instability between the particles and fields. However, using a higher order weighting scheme did not

cure the problem. The problem was alleviated by doing a very light filtering on the vector potential at each integration. The filter used is

$$a'_j = W a_{j-1} + (1 - 2W) a_j + W a_{j+1} \tag{A4.1}$$

where the weighting factor W is less than, but on the order of the time step Δt, a is the complex vector potential, and the index j designates the grid point. Application of the Von Neumann stability analysis (*e. g.* Roache, 1972) to the field equation (assuming no sources and constant coefficients) shows that the phase errors can be arbitrary at the shortest wavelengths. This and the fact that filtering out the shortest wavelengths in the simulation indicates that the problem is due to dispersive errors in the finite differencing scheme used to integrate the field equation. It should also be noted that too much filtering results in a loss of short wavelength features that are an essential part of the shock structure. Filtering of the vector potential is also employed over a number of grid points near the boundaries. This is done to make the boundaries absorbing so that waves and disturbances reaching the boundaries are not reflected back into the system.

The simulation is suspended at regular intervals to produce diagnostic plots. Typical diagnostics include the magnetic field profiles, moments of the ion distribution function, ion phase space plots, the electrostatic potential, currents, and any quantities which may be derivable from these. The simulation may also be used to save space-time histories of any quantity. However, this tends to require a lot of storage space and should be done judiciously. One major advantage of the simulation is that it is reproducible. A simulation run can be reproduced exactly by providing input identical to a previous run. Other versions of the same case may be produced by either changing the scaling parameters or the seed integer for the random number generator that initializes the particle velocities. So, any diagnostics that are not generated in a given run can be produced by another, but at the cost of additional computer time.

Appendix B Entropy and the Equations of State

This appendix discusses how equations of state describing changes of state of a gas relate to the change in entropy of the gas. An equation for the change in entropy for a general power law equation of state ($P/n^{\alpha} = constant$) will be derived. The four possible cases for the change of state and corresponding change in entropy are described and an example of each is given. Finally we consider how this relates to the electron equations of state discussed in Chapter 4 and the ion heating in Chapter 6. It should be pointed out that in this section α is used for the power law exponent to distinguish it from γ, the ratio of specific heats. In Chapters 4 and 6 γ was used to represent the exponent.

For a perfect gas with constant specific heats the entropy may be defined as (Landau and Lifshitz, 1958)

$$S = (Nk)\log P + (Nc_p)\log kT + S_0 \tag{B1}$$

where N is the total number of molecules, k is the Boltzmann constant, c_p is the specific heat per molecule at constant pressure, and S_0 is a constant. If we make use of the definitions $k = c_p - c_v$ where c_v is the specific heat at constant volume, $\gamma = c_p/c_v$, and $P = nkT$, then the above expressions can be reduced to the following form

$$S = \frac{N}{c_v}\log\left(\frac{P}{n^{\gamma}}\right) + S_0 \tag{B2}.$$

For an ideal gas $\gamma = 5/3$. In general, for a real 3-dimensional gas the value lies in the range $1 \leq \gamma \leq 5/3$ (Priest, 1982, p. 84). The limiting value of $\gamma = 1$ would only be reached for molecules with an infinite number of degrees of freedom. We shall limit ourselves to the special case of an ideal gas and let $\gamma = 5/3$ for the definition of the entropy. This is applicable to the solar wind since a fully ionized hydrogen plasma has only the three translational degrees of freedom per particle.

We can use the above equation to obtain information about a gas undergoing a change of state. If the change of state can be characterized by a generalized power law, $P = C_0 n^\alpha$, then we may write an expression for the change in entropy as

$$\Delta S = S_2 - S_1 = \frac{N}{c_v}(\alpha - 5/3)\log\left(\frac{n_2}{n_1}\right) \qquad \text{(B3)}.$$

This leads to four possible cases for changes in the entropy depending on whether the density has increased or decreased and whether the exponent is greater or less than 5/3. The entropy change for the for cases are listed in Table B.

Table B Entropy Changes for Power Law Equation of State

	$n_2/n_1 > 0$	$n_2/n_1 < 0$
$\alpha > 5/3$	$\Delta S > 0$	$\Delta S < 0$
$\alpha < 5/3$	$\Delta S < 0$	$\Delta S > 0$

For the special case of $\alpha = 5/3$, then there is no change in the entropy and we have the usual isentropic-adiabatic equation of state.

It should be noted here that it is not being suggested that the total entropy of a system may be decreased. We only examine the changes of state of a gas in a defined region of space. It is not specified how the changes are to take place, only that they do. The change of state could be accomplished by work being done to or by the gas, as well as by heat flow in and out of the volume. As always, the second law of thermodynamics cannot be violated.

To help illustrate the entropy changes described above, an example demonstrating each of the above four cases is given. Since the thermodynamic quantities defining the final state of the gas are independent of the process by which that state is achieved, we need only to find a process that satisfies the desired change of state.

A) For a compression with $\alpha > 5/3$, let us consider how a transition producing $P_2 = C_0 n_2^\alpha$ might be brought about. First, we compress the gas adiabatically

so that $P_2 = C_0 n_2^{5/3} < C_0 n_2^{\alpha}$. Now to further increase P_2 so that $P_2 = C_0 n_2^{\alpha}$ (at constant volume) we must add heat (Q) to the gas and the entropy will increase by $\Delta S = \int \frac{dQ}{T}$.

B) An example of this case is the isothermal ($\alpha = 1$) compression of the gas. To accomplish an isothermal compression we compress the gas adiabatically so that $P_2 = C_0 n_2^{5/3} > C_0 n_2^{\alpha}$. To reach the desired final state heat must be removed from the gas so the entropy of the gas decreases.

C) To obtain an expansion with $\alpha > 5/3$ we first expand the gas adiabatically to obtain $P_2 = C_0 n_2^{5/3} < C_0 n_2^{\alpha}$. Now with the volume constant we must add heat to get $P_2 = C_0 n_2^{\alpha}$.

D) A classical example of this case is the free expansion of a gas into a vacuum. This is an adiabatic-isothermal expansion in which the entropy increases.

We shall now consider how this relates to the electron equation of state. The isotropic-adiabatic equation of state is given by

$$P/n^{5/3} = constant \tag{B4}$$

which expresses conservation of entropy. If we take the cube of this equation and let $P^3 = P_{\perp}^2 P_{\parallel}$ (to reflect two degrees of freedom for the perpendicular direction and one for the parallel) it may written as

$$\frac{P_{\perp}^2 P_{\parallel}}{n^5} = constant \tag{B5}.$$

Now if we require that the magnetic moment be conserved we arrive at the CGL equation of state (presented in Chapter 4). Thus the CGL equation of state preserves both the magnetic moment and entropy of the electrons. The modification to get the CCGL equation is to allow the electrons to be isothermal along the magnetic field direction. Thus the CCGL equation represents a loss of entropy for the electrons.

In the case of the ions, the analysis of Chapter 6 and the results above show us where the entropy production (and hence the energy dissipation) occurs. Of the two stages of heating described, the greatest entropy production occurs during the first stage in the upstream region (except for very low Mach number, $M_A \lesssim 1.5$). In general the entropy production precedes the compression in the shock. It should be pointed out here that since the entropy may be defined in terms of the logarithm of the temperature, it is the temperature ratio that determines the degree of entropy change. In terms of heating, since $dQ = C dT$ (where C is usually the specific heat and may be process dependant) it is the temperature difference between two states that determines the degree of heating that has occurred.

Appendix C Test Particle Calculations

In this appendix we shall consider the results of the interaction of charged particles incident upon various magnetic field structures. The intent of this section is to demonstrate how a substantial amount of 'heating' can be accomplished in a collisionless plasma by simple discrete particle effects within the finite larmor radius limit. The motive for examining this problem is that shock waves in magnetized plasmas are generally accompanied by wavetrains as well as a sudden increase in the magnetic field magnitude. A set of equations will be derived which predict the resultant velocities of a particle after encountering a discontinuity in the magnetic field. The velocities are displayed as functions of θ_B, the angle between the magnetic field vectors on the up and downstream sides of the discontinuity. It will be shown that a critical angle ($\theta_B = \theta_r$) exists above which particles are reflected at the discontinuity. Test particle calculations will be used to confirm the results of the model and then examine the effects of having a 'discontinuity' of finite thickness. Then the test particle calculations will be extended to examine the results of having a distribution of thermal particles and including a precursor wave in the magnetic fields.

This work is similar to that done by Lee *et al.* (1986). They consider the temperature rise across a discontinuity under conditions appropriate to oblique shocks where the angle between the shock normal and the magnetic field is large ($\theta_{Bn} \geq 50°$). What is considered here is appropriate to the geometry of quasi-parallel shocks where $\theta_{Bn} \approx 0$). This difference is important for the accessibility of the upstream region to particles that have encountered the discontinuity. If the reader wishes to compare the results, note that Lee *et al.* (1986) plot the ratio of the downstream thermal energy to the upstream kinetic energy ($T_2/E_1 \equiv V_{\perp 2}^2/V_1^2$), whereas here $V_{\parallel,\perp 2}/V_1$ is plotted.

The problem to be considered here is the motion of a charged particle incident upon a discontinuity in the magnetic field. The particle is initially traveling parallel to the magnetic field which at some point experiences a discontinuous change in direction and magnitude. Initially, $\vec{B} = B_1(0,0,1)$, $\vec{V} = V_1(0,0,1)$, for $z < 0$. The discontinuity lies in the x-y plane at $z = 0$. At and beyond the discontinuity ($z \geq 0$) $\vec{B} = (B_x, 0, B_z) = B_1(\tan(\theta_B), 0, 1)$. The z-component of the magnetic field is held constant. The geometry is shown in Figure C1.1. Figure C1.1a shows the direction and density of magnetic field lines on either side of the discontinuity. Figure C1.1b shows the components of the velocity perpendicular and parallel to the magnetic field at the discontinuity and the components of the gyro-radius in the downstream region (in the x-z plane). Figure C1.1c shows typical trajectories of a transmitted and reflected particle.

At the instant the discontinuity is traversed, the velocities parallel and perpendicular to the downstream magnetic field are given by

$$V_{2\parallel} = V_1 \cos\theta_B \tag{C1a}$$

$$V_{2\perp} = V_1 \sin\theta_B \tag{C1b}$$

At this point in time, the perpendicular velocity has components in the $-\hat{x}$ and $\hat{z}$ directions so the initial gyrational motion along $\hat{z}$ is in the positive direction. Assuming the particle remains in the downstream region, it will gyrate back a maximum distance in the $-\hat{z}$ direction after 3/4 of the gyro-period, $\Delta t = (3/4)(2\pi/\Omega_2)$ where $\Omega_2 = eB/mc$ is the gyro-frequency. This is because initially the z component of the gyrational motion is positive and the z-component of the guiding center motion is always positive as long as $z > 0$. During the first cycle, when the z-component of the gyro-motion is negative, if the particle re-encounters the discontinuity it will pass through and continue on into the upstream region. The maximum value of the z-component of the gyro-radius is (see Figure 1.1b)

$$r_z = \frac{V_{2\perp}}{\Omega_2}\sin\theta_B = \frac{V_1}{\Omega_2}\sin^2\theta_B \tag{C2}.$$

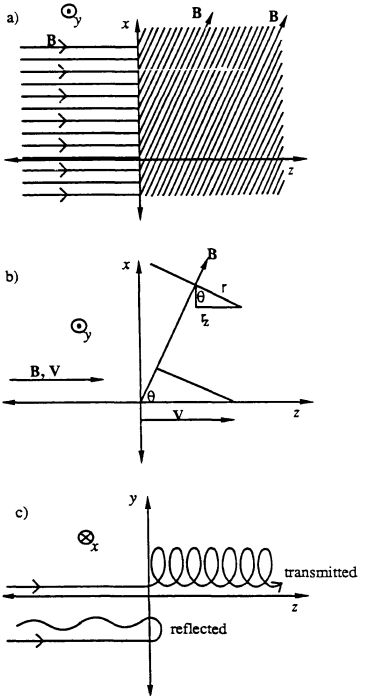

Figure C1.1 a) Representation of the magnetic field lines with a discontinuity in the x-y plane at $z = 0$. b) Geometry of the discontinuity in the magnetic field. c) Typical trajectories of a transmitted and reflected particle projected upon the y-z plane.

The z-component of the guiding center displacement is

$$\Delta z = (\Delta t) V_{1\parallel} \cos\theta_B = (\Delta t) V_1 \cos^2\theta_B \qquad \text{(C3)}.$$

Equating the maximum of the z-component of the gyro-radius, r_z, to the displacement, Δz, due to the guiding center motion along the $\hat{z}$ axis during this time interval ($\Delta t = 3\pi/\Omega_2$, then we get a relation defining a critical angle θ_R above which particles will be reflected.

$$\tan^2\theta_R = \frac{3\pi}{2} \quad \text{or} \quad \theta_R = 65.27^\circ \qquad \text{(C4)}.$$

Particles are transmitted if $\theta_B < \theta_R$ and reflected if $\theta_B > \theta_R$. Particles get reflected because they re-encounter the discontinuity with $V_z < 0$ within the first orbit. If the particle does not re-encounter the discontinuity it will continue to move along the downstream magnetic field. Figure C1.1b shows typical trajectories of a transmitted and reflected particle in the y-z plane.

The magnitude of the parallel and perpendicular velocities of transmitted particles are given by equations C1a and b. To determine the velocities of the reflected particles we must find the time at which the discontinuity is re-encountered and the particles' velocities at that time. To define the time we equate the displacement due to the z-component of the guiding center motion to the z-component of the gyro-radius and note that the encounter will occur between $\pi/\Omega_2 \leq \Delta t \leq 3\pi/2\Omega_2$ yielding

$$\cot^2\theta_B = -\frac{\sin(\Omega_2 \Delta t)}{\Omega_2 \Delta t} \qquad \text{(C5)}.$$

For a fixed value of θ_B, this expression can be solved numerically to find $\Omega_2 \Delta t$. Now we need to find the particle velocity components at this time. They are obtained from

$$\vec{V}_\perp = V_1 \sin\theta_B \{(-\hat{x}\cos\theta_B + \hat{z}\sin\theta_B)\cos(\Omega_2 \Delta t) + \hat{y}\sin(\Omega_2 \Delta t)\} \qquad \text{(C6a)}$$

$$\vec{V}_\parallel = V_1 \cos\theta_B (\hat{x}\sin\theta_B + \hat{z}\cos\theta_B) \qquad \text{(C6b)}.$$

The resulting perpendicular and parallel velocities in the upstream region will then be

$$V_\perp = V_1 \sin\theta_B \left\{\cos^2\theta_B \left(1 - \cos(\Omega_2 \Delta t)\right) + \sin^2(\Omega_2 \Delta t)\right\}^{1/2} \qquad \text{(C7a)}$$

$$V_{||} = V_1 \left(\cos^2\theta_B + \sin^2\theta_B \cos(\Omega_2 \Delta t)\right) \qquad \text{(C7b)}.$$

In Figure C1.2a and b the magnitude of the parallel and perpendicular velocities are plotted as a function of the angle θ_B. The lines represent the analytic results given above and the symbols are the results of test particle calculations. The discontinuity in the velocities is the point at which particles get reflected and the parallel velocity becomes negative for $\theta_B > \theta_r$. One can see from the figure that the two results match very well. It should be noted however that the test particle calculations indicated a reflection angle of $\theta_r = 65.8°$ whereas the analytic result yielded 65.3°. This small discrepancy is most likely due to the finite size of the time step for the particle calculations.

Next we consider the effect of the finite width (L_d) of the 'discontinuity'. Figure C1.3 shows the same results as plotted in Figure C1.2 but for different widths of the discontinuity. Both parallel (denoted by solid lines and circles) and perpendicular (denoted by dashed lines and triangles) velocities are placed on the same plot. The discontinuity is formed by fitting the values on both sides with a hyperbolic tangent whose argument is normalized to the desired width. The lengths are in units of the upstream streaming gyro-radius ($r_s = V_1/\Omega_1$). The figure shows the expected result. As the discontinuity widens the particle flow becomes more field aligned and the reflection angle moves towards 90°.

Figure C1.3a shows the form for all cases where $L_d \ll r_s$ as long as the timestep satisfies $V_1 \Delta t \ll L$ so the particle samples many points along the discontinuity. If the condition $V_1 \Delta t \gg L_d$ then the particles do not sample along the discontinuity and the figure would look similar to a true discontinuity as in Figure C1.2. Figure C1.3d shows

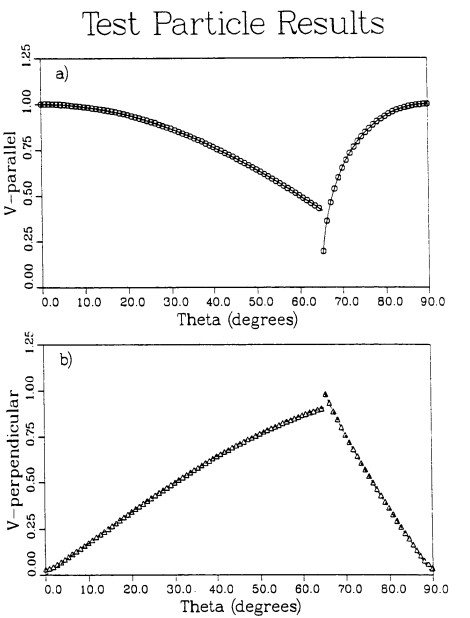

Figure C1.2 Magnitude of the a) parallel and b) perpendicular velocities relative to the local magnetic field. The lines are from the analytic solutions (eqns. C6a and b) and the symbols are the results of test particle calculations.

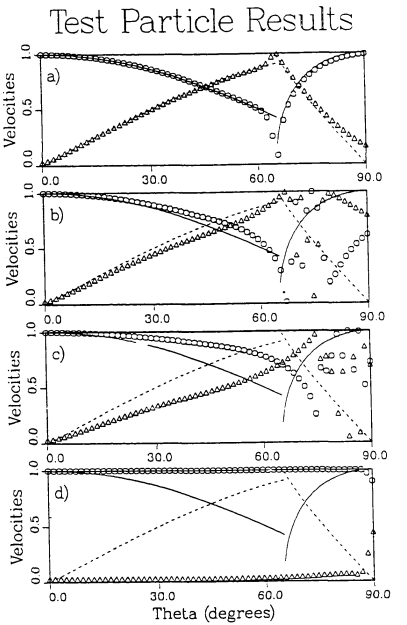

Figure C1.3 Plots of the results of test particle calculations of the interaction with a 'discontinuity' of finite width. Plotted are the magnitude of the parallel and perpendicular velocities as functions of the change in the magnetic field angle. The widths considered, in units of the streaming gyro-radius $r_s = V_1/\Omega_1$, are a) 0.1, b) 0.5, c) 1.0, and d) 5.0. Circles and the solid lines represent the parallel velocity while triangles and dashed lines are used for the perpendicular velocity.

the form for all cases where $L_d \gg r_s$. In this case the field line curvature is gradual so particles can follow the magnetic field.

These results show that considerable heating of a plasma may be accomplished by the interaction with a discontinuity in the magnetic field. In the ideal case of a perfect discontinuity, $V_{2\perp} > V_{2\parallel}$ for $\theta_B > 45°$ and particles get reflected for $\theta_B > \theta_r \approx 65°$. For a 'discontinuity' whose thickness is $L_d \lesssim r_s$ considerable heating is still achieved but less than for the ideal case. For $L > r_s$ the particles behave adiabatically and virtually no heating occurs. The particles are able to flow parallel to the magnetic and no particles get reflected. These test particle results do exclude small range of angles $\theta_B \approx 90°$ since roundoff errors become large for the model used. The last point plotted in the figures is $\theta_B = 89.9$.

Now the test particle calculations are extended to examine a distribution of thermal particles. For these calculations we fix $\theta_B = 50°$ and vary the width from $L_d = 0.1\rho_s$ to $L_d = 10.0\rho_s$. Ten phase angles are used and the calculations are done with initial thermal velocities of $V_{th} = 0.1V_1$ in Figures C1.4a and b and $V_{th} = 0.5V_1$ in Figures C1.4c and d. Plotted in Figure C1.4 are the final parallel and perpendicular velocities as a function of the width of the discontinuity (L_d). The symbols are the average over all phase angles and the error bars represent the range of values obtained. This shows that the particles have an increase in perpendicular velocities only when the width of the discontinuity is small. The parallel and perpendicular velocities are spread over a broad range only for a hotter distribution of particles.

The model is now again extended by adding a right-hand polarized precursor wave field to the discontinuity to more accurately represent the observed structure of the quasi-parallel collisionless shock. The waves increase in amplitude linearly as the discontinuity is approached from the upstream side and then the amplitude is attenuated exponentially beyond the discontinuity. The wavelength is set to be equal to the width of the discontinuity

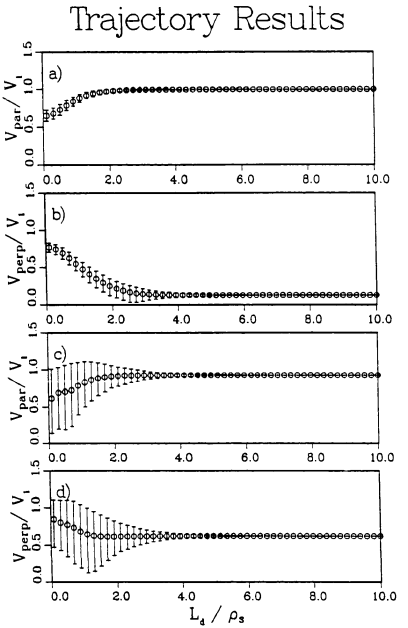

Figure C1.4 Results of test particle calculations for a distribution of thermal particles on a discontinuity. The final parallel and perpendicular velocities are plotted as a function of the width of the discontinuity. The initial thermal velocities are $0.1V_i$ in a) and b) and $0.5V_i$ in c) and d). The the symbol is the average over all phase angles and the error bars represent the range of values.

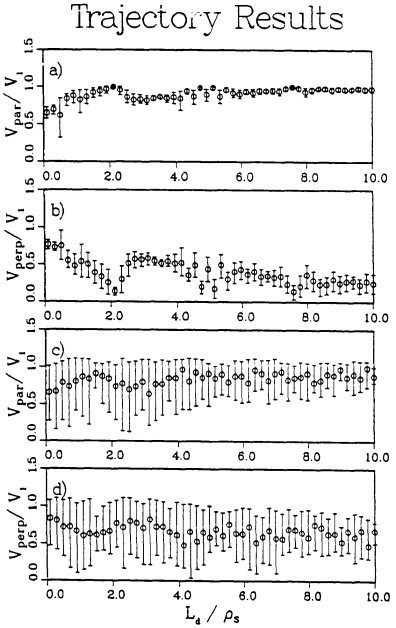

Figure C1.5 Same as Figure C1.4 but in this case a right hand circularly polarized wave train has been added to the magnetic field upstream of the ramp. The initial thermal velocities are $0.1V_1$ in a) and b) and $0.5V_1$ in c) and d).

(L_d) and the amplitude at the ramp is equal to the downstream B_z. The magnetic field structure is very similar to that seen in Figure 3.2 but the waves are purely sinusoidal and noise free. Figure C1.5 shows the resultant velocities from using this magnetic field structure. One can see that considerably more scattering of the particles occurs for all widths. The calculation was also performed with the wave fields without the discontinuity present. Then the velocity scatter was less than for the discontinuity without the wave fields.

There are some important points to consider in relating this model to the ion heating that can be accomplished at a shock due to the magnetic field structures. From the standpoint of cold non-interacting test particles traveling in a fixed magnetic field, the resulting upstream or downstream distributions would be gyro-phase bunched and would not necessarily exhibit a significant increase in temperature. The phase angle for the perpendicular velocity component should also be fairly random for the downstream distribution. In Figure C1.6 the phase angles for the trajectory results shown in Figures C1.4 and C1.5 are plotted. Figure C1.6a shows that the cooler particles incident on a ramp are highly gyro-phase bunched for $L_d < 2$ and are transmitted mostly undisturbed for L_d greater than that. Figure C1.6b shows similar results for the hotter particles but here the spread in phase is greater and the breakpoint is near $L_d = 1$. Figures C1.6c and d show that when the wave fields are added that the phase angle bunching is is pushed to smaller L_d but has not otherwise altered much. It should be pointed out that in the calculation no thermal component was added to the parallel velocity. Doing so would be equivalent to averaging over a range of L_d so a number of the gyro-phase bunched clumps seen in Figure C1.6c would be averaged together resulting in a more uniform distribution over all.

It from these results it appears that the time independent magnetic field model combining the discontinuity with the upstream wave field can lead to a substantial amount of heating if the width is greater than the streaming gyro-radius. For L_d less than this the

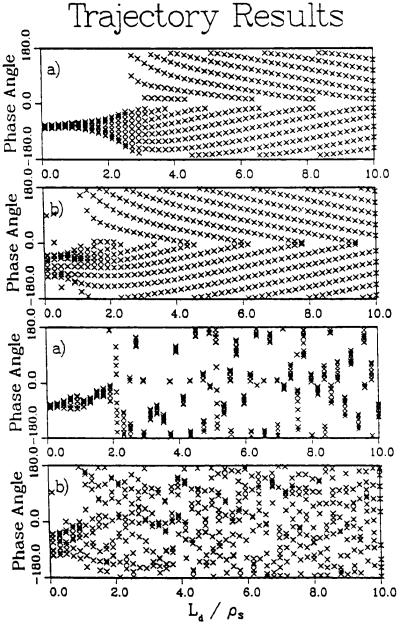

Figure C1.6 Phase angles for the trajectory results displayed in Figures C1.4 and C1.5. a) corresponds to C1.4a and b, b) to C1.4c and d, c) to C1.5a and b, and d) to C1.5c and d. The phase angles are plotted for ten particles at each value of L_d.

perpendicular velocity increases considerably if initially small or the velocities are spread if they are initially hot. However, they tend to be gyro-phase bunched which is not true heating for the case of cold particles. If the particles themselves were allowed to interact through the electromagnetic fields then a gyro-phase bunched distribution would likely be unstable. Unstable wave growth would result in phase mixing and further thermalization of the distribution. Another likely contributor to gyro-phase mixing is time dependant effects and turbulent type inhomogeneities that will be present in the simulation and in true shocks. That these irregularities are more evident at higher Mach numbers where they seem to be required (since L_d is smaller) is reasonable.

In summary, it has been demonstrated that the time independent macroscopic structure of the magnetic fields of the quasi-parallel collisionless shock wave is such that the interaction of particles with it results in a significant amount of heating. Any additional time dependant behavior in the magnetic fields should only add to the scattering that the particles experience. Thus one does not need to invoke micro-instabilities to account for the dissipation in the shock even though they may play a role in determining the complete structure.